The Volume Distribution of Artificial Aurora Induced by HF Radio Waves in the Ionosphere

—

Andreas Kvammen
FYS-3900 Master's thesis in physics August 2016

Abstract

This thesis presents three-dimensional modelling of artificial aurora in the ionospheric F layer, induced by high frequency (HF) O-mode radio waves from the EISCAT heating facility. Understanding how HF radio waves produces enhanced emission in the ionosphere has been one of the one of the major motivations for conducting heating experiments during the last decades. A key element for understanding the heating process is to accurately determine the RIOE (Radio Induced Optical Emission) volume distribution. There are two main theories explaining the RIOE, the accelerated electron excitation theory and the thermal electron excitation theory.

Three different auroral construction techniques were considered, theoretical, semi-theoretical and free parameter search. The theoretical modelling is based on accelerated electron excitation theory predictions. Projections of the three dimensional models were compared to observational images of the artificial aurora, taken at the Auroral Large Imaging System (ALIS) in northern Sweden. ALIS takes simultaneous images of the RIOE at four separate ground based imaging stations. This allows tomographic-like reconstruction of the artificial aurora. The ALIS images were taken with different filters, providing auroral modelling of the 5577 Å, 6300 Å and 8446 Å emission lines.

It was clear, by comparisons between the observational images and the projections of the modelled aurora, that the semi-theoretical and free parameter search modelling provided physically sound and statistically feasible constructions of the artificial aural. Whereas the theoretically modelled aurora projections did not agree with the observational images.

Acknowledgement

First and foremost, I would like to thank Björn Gustavsson for all the support and help throughout the year. It would not have been possible to write this thesis without your guidance. I have learned a lot during this year and I would like to thank Björn for making the work enjoyable.

I would also like to thank the staff at Nordic Optical Telescope and UIT for giving me the opportunity to write this thesis while working as a student support astronomer at the Nordic Optical Telescope in La Palma, Spain. It has been a very rewarding experience.

Last but not least, I would like to thank Christine Nilsen, Björn Gustavsson and Gregor Decristoforo for much appreciated visits and my co-students at Nordic Optical Telescope. You have all made the year in La Palma great.

Contents

CHAPTER 1

Introduction

The first successful multi-station imaging of the northern lights was led by the Norwegian geophysicist and mathematician Carl Størmer (1874-1957). At the begining of the 20th century, Størmer and his collegues took more than 20 000 auroral photographs. The photographs were taken simultaniously from two stations, one at Upper Alta School and the other at Bossekop church , near the city of Alta in Northern Norway. [Brekke and Egeland, 1994]
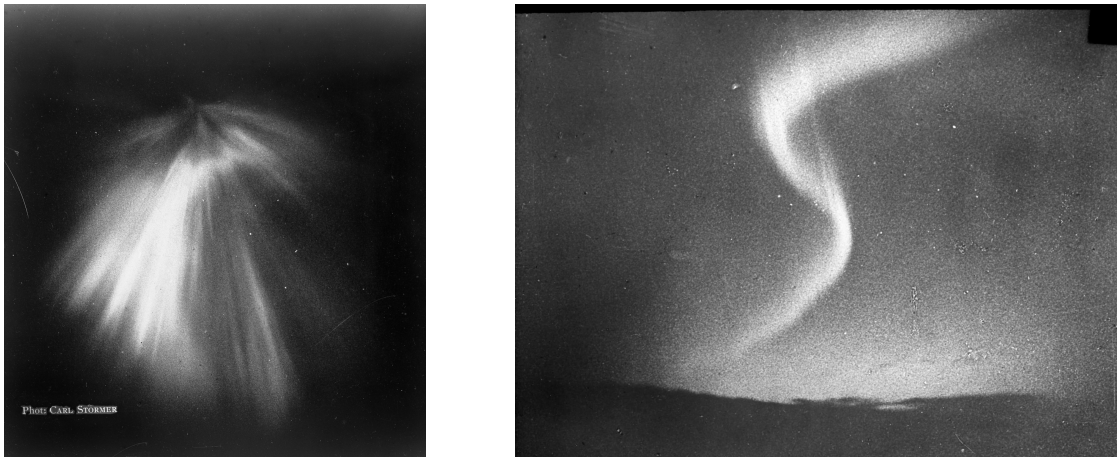
Figure 1.1: Photographs of the northern lights by Carl Størmer. The photographs are owned by Norsk Teknisk Museum.

Størmer realised that he would get more information about the auroral height and distribution by photographing the northern lights simultaneously from more than one direction. Størmer and his colleagues were able to estimate the first reliable height distribution of the northern light using the auroral photographs and triangulation. The heights of the peak auroral brightness from 10 000 auroral photographs are presented in figure 1.2 below:

Figure 1.2: To the left, a photograph from 1910 of Carl Størmer with one of the auroral cameras and his assistent Bernt Johannes Birkeland at Talvik in Finmark, Norway. The photograph is taken by Anders Beer Wilse and owned by Norsk Folkemuseum. To the right, the estimated height distribution of the northern lights presented by Størmer. The number of auroras observed is given along the x-axis and the height of the aurora is in km along the y-axis. Northern lights are usually observed in the ionospheric E layer, between 90 km and 150 km, with a peak observational frequency at about 100 km in altitude. [Brekke, 2012]

Multi-station imaging of the aurora remains a scientific field of interest, almost 100 years after the auroral campaign near Alta. The auroral appearance, intensity and frequency continues to carry new information about the solar wind, the Earth's magnetic field and the chemistry and composition of the ionosphere. The method of simultaneous multi station imaging is the same, but the technology has improved a great deal since the beginning of the 20th century. The Aurora Large Imaging System (ALIS), consists of four separate ground based imaging stations. Each station is equipped with a high resolution monochromatic CCD-camera. By employing ALIS and tomographic inversion methods, it possible to estimate the three dimensional shape of the auroras.

Experiments to simulate the aurora were first done by the great Norwegian scientist Kristian Birkeland (1867-1917) in his "Terrella"[1] experiment. In his famous experiment, Birkeland used a magnetized ball, the Terrella, which represented the earth and an electron gun to represent the solar wind. The ball was painted with fluorescent paint, so that the electrons hitting the ball would cause emission, like electrons entering the atmosphere causes emission by exciting ionospheric constituents. The Terrella was put inside a vacuum chamber to ensure that the electrons could move without collisions, and only be

---

[1]Terrella is from latin, meaning "little Earth"

affected by the magnetic field. The beam of electron fired towards the Terrella would then act similar to the electrons from the solar wind when approaching the Earth. Birkeland discovered that when the electron gun was powered on, the electrons were led towards the poles of the magnetized ball. The energetic electrons hit the florescent paint around the poles producing the characteristic emission rings of the Terrella, much like the northern and southern lights around the poles of the Terra, the Earth. [Brekke and Egeland, 1994]
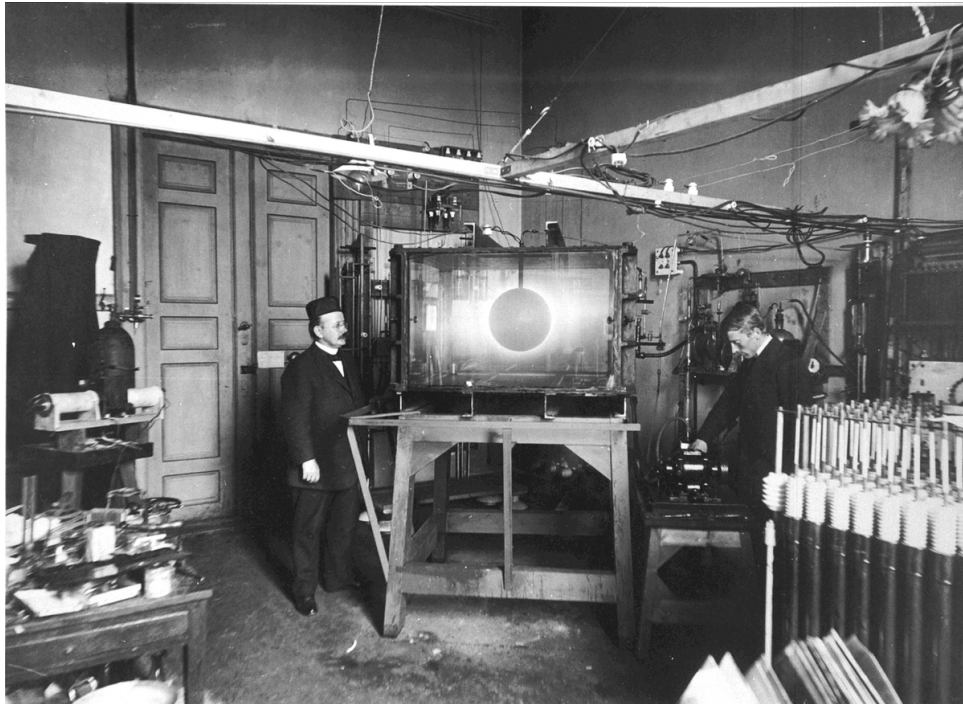

Figure 1.3: The photograph shows Kristian Birkeland to the left and his assistent Karl Devik to the right in the laboratory in the university of Kristiania. Between them is the vacuum chamber containing the Terrella. The image is taken from [Brekke and Egeland, 1994]

Today, artificial auroras are made in the ionosphere by heating experiments. The European Incoherent Scatter Scientific Association (EISCAT) has one of the worlds most powerful heating facilities preforming such experiments, located in Ramfjorden, Norway. At the EISCAT heating facility, high frequency radio waves are transmitted anit-parallell to the magnetic field. When the radio-waves reaches the ionospheric F layer, between 150 km and 800 km, several wave-plasma interactions occurs which will accelerate electrons. The accelerated electrons excites constituents in the ionosphere, leading to emissions with emission lines similar to the ones of the northern lights, hence the name artificial auroras. The radius of the RIOE (Radio Induced Optical Emission) blobs are typically 10 km, giving emission volumes of the order 10^{12} m^3. For comparison, the Terrella experiments produced emission rings with volumes of the order 10^{-4} m^3. This gives a scale difference of 10^{16} m^3.

Several attempts have been made the last decades to explain how the energy of the high frequency radio waves causes artificial auroras. There are two main theories attempting

to explain the RIOE, the thermal electron theory, as presented in [Mantas, 1994] and the acclerated electron theory [Bernhardt et al., 1989]. In order to understand the cause of the RIOE, it is important to find good methods for estimating the three dimensional emission rate distribution. The motivation for this thesis is therefore to use simultaneous multi-station images to estimate the volume emission rate of the artificial aurora, induced by EISCAT heating. This will be done in three emission lines, 5577 Å, 6300 Å and 8446 Å. The estimated volume emission rate distributions will be compared to theoretical predictions. An additional goal of this thesis has been to develop better background subtraction and flat-field correction methods.

The Heating Experiment And Observations

In this chapter the experimental set-up and the instruments used at EISCAT and ALIS will be described. The EISCAT observations will be presented and the motivation behind the filter cycle used at ALIS will be explained. The experimental constrains will be discussed at the end of this chapter.

2.1   The EISCAT Heating Facility

The European Incoherent Scatter Scientific Association (EISCAT) is located in Ramjorden 69.6° north and 19.2° east [Gustavsson et al., 2005], near Tromsø in northern Norway. This thesis will focus on the heating experimen conducted at EISCAT the 16th of February 2015. On this date, the ionospheric heating was powered by 12 transmitters, each with a power of 80 kW, making the total heating power 960 kW. This power is feed to dipole antennas which transmit the frequency dependent effective radiated power (ERP) as high frequency radio waves. The ERP, using the EISCAT antenna array 3, is approximately 138,2 MW at 6.2000 MHz and 115.9 MW at 5.423 MHz frequency modulation. The transmitted HF radio waves were directed 12 degrees from zenith, so that the main beam was pointing anti-parallel to the magnetic field above EISCAT.
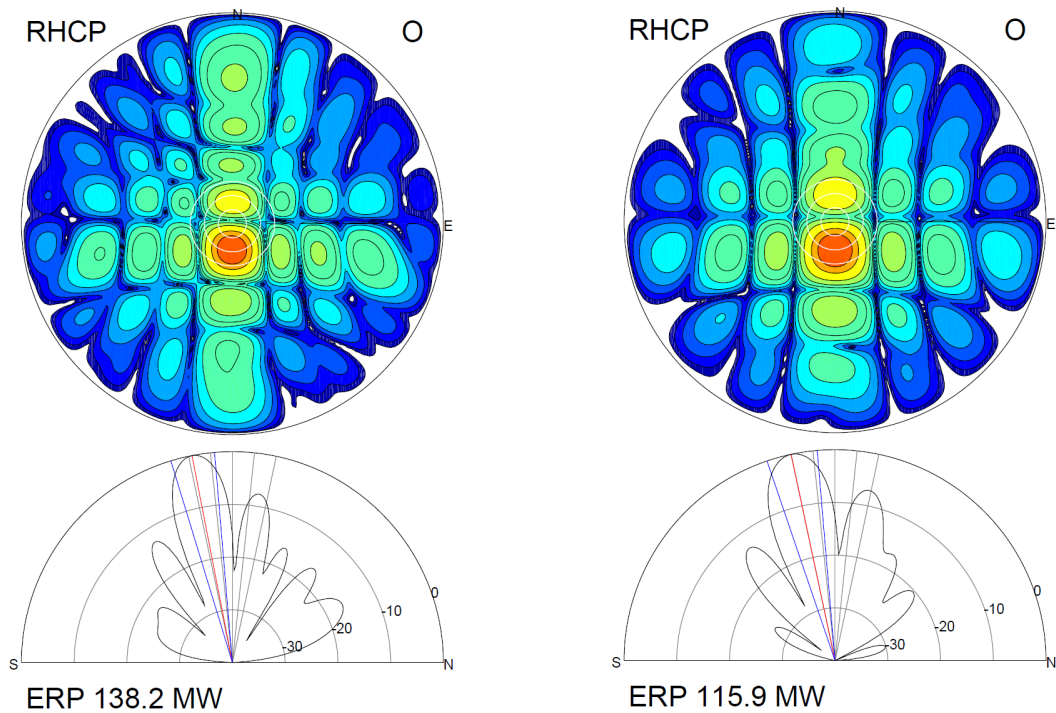
Figure 2.1: The figures show the 6.200 MHz beam pattern in the meridional plane to the bottom left and the 5.423 MHz beam pattern to the bottom right. Above the beam patterns are the 2D radiated interference patterns for the corresponding frequencies.

The heating experiment used a 150 second on and 85 second off cycle[1]. This modulation made it possible to measure the sky background in between pulses and to estimate the growth and decay time of the 6300 Å emission from the long lived $O(^1D)$ excited state.

The airglow was induced by ordinary mode (O-mode) HF radio waves. The radio waves had a frequency of 6.200 MHz from 16:00:00 UT to 16:49:30 UT and a frequency of 5.423 MHz from 16:50:55 UT and onwards.

---

[1]On is when the HF antennas are turned on and ionospheric heating is on going. Off is when the antennas are off and there is no artificial heating.
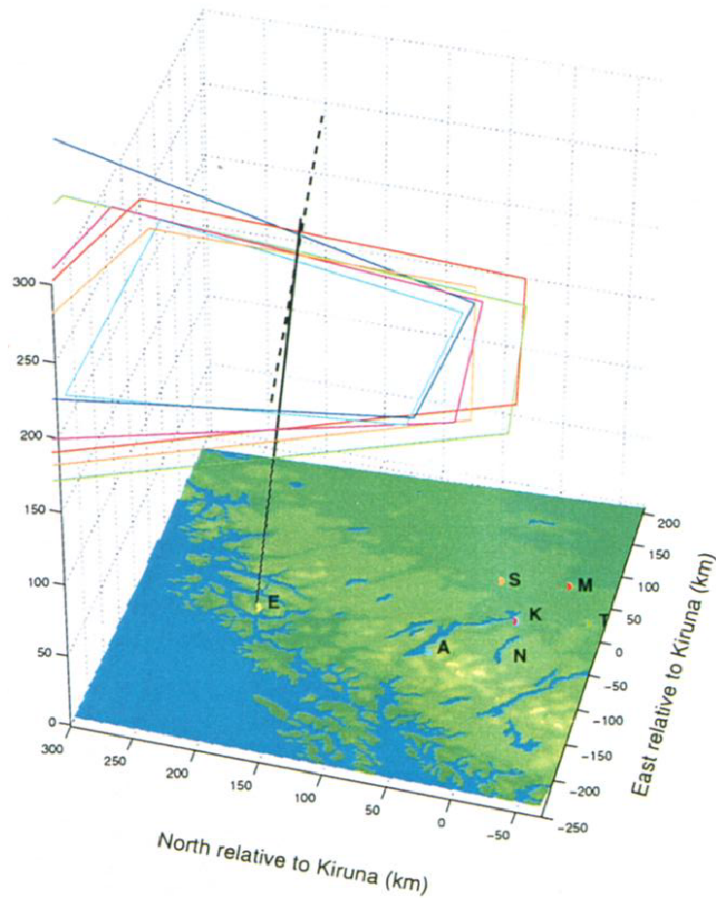
Figure 2.2: The figure show the geometry of the experiment. The point marked with E is the heating facility in Ramfjorden. Points A, K, M, N, S and T show the location of the ALIS imaging stations in Abisko, Kiruna, Merasjärvi, Nikkaluokta Silkimuotka and Tjautjas. The coloured quadrangles around the heating beam show the imaging stations field of view at the heating altitude, around 250 km above the ground. Figure from [Gustavsson, 2000]

However, the main purpose of EISCAT is not ionospheric heating, but to measure ionospheric plasma parameters using incoherent scatter (IS) radars. Simultaneous to the heating experiment, the EISCAT-UHF radar was operating in order to measure the plasma parameters. The EISCAT-UHF radar is a 32 m parabolic dish antenna with a peak transmitting power of more than 2.0 MW. It is transmitting in the 931 MHz band from Ramfjorden. Three receivers, located in Ramfjorden (Norway), Kiruna (Sweden) and Sodankylä (Finland), are making continuous tri-static measurements of the backscattered signal. The tri-static measurements are preferred to one station measurements since they give better measurements of the motion of the plasma. The receivers provide measurements with 3 km height resolution and 5 second time resolution. The theory and science of the EISCAT IS radars is not directly relevant for this thesis and will therefore not be covered extensively. Nevertheless, a short review is in order and will be given since

data from these radars are being used.

2.1.1 The EISCAT IS power Density Spectrum

The EISCAT-UHF radar transmit ultra high frequency (UHF) radio waves into the atmosphere. The transmitted UHF waves are scattered from fluctuations in the plasma density, caused by ion-accoustic and Langmuir waves. A small fraction of the scattered radiation will be directed back towards ground based receivers. The free electrons in the ionosphere are scaterrers. It is assumed that the scattering of each electron is independent of each other, they are incoherent, and the scattering can be considered to be a random process. From the auto correlation function of the received signal it is then possible to extract the characteristic power density spectrum. The plasma and ion lines in the power density spectrum carries information about the ionospheric plasma parameters. The plasma parameters of interest in this thesis is the electron density (n_e), the ion temperature (T_i) and the electron temperature (T_e). The power of the returned signal is proportional to the electron density. The electron density is therefore found by integrating the received power density spectrum over all frequencies. I.e. more scatterers (electrons) give more backscattered radiation and hence a larger power density spectrum area. The electron and ion temperatures are estimated from the ion-line shape in the power density spectrum.
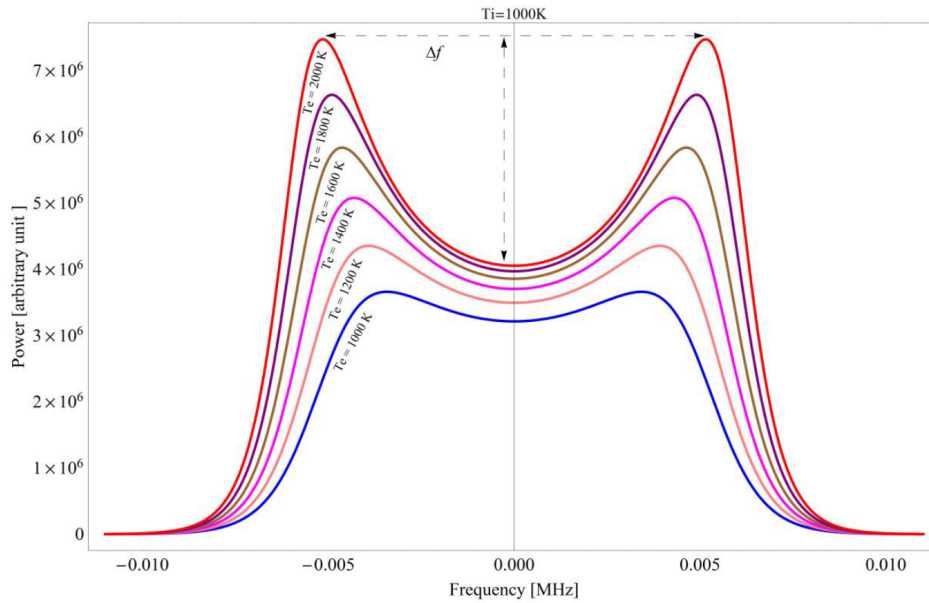

Figure 2.3: The figure show the theoretical shapes of the two ion lines at approximately ± 0.005 MHz with different electron to ion temperature ratios. The electron temperature can be estimated by the frequency width of the ion lines. I.e. higher electron temperatures will cause higher random motion which again will cause more Doppler broadening of the ion lines. Whereas lower temperatures (but still much higher than the ion temperatures) will cause narrowing of the ion lines, assuming low landau dampning. From the electron temperature it is possible to estimate the ion temperature by looking at the characteristic peak to valley ratio of the ion lines, as shown in the figure above. The figure is taken from [Dalipi and Syla, 2013].

2.1.2 EISCAT observations

From the IS power density spectra, the electron density and the electron and ion temperatures were estimated. This is already done at EISCAT. The received EISCAT data, the plasma parameters, can therefore be plotted directly, as shown in figure 2.4. The plasma parameters will be of interest when comparing the radio induced emission to theoretical predictions.
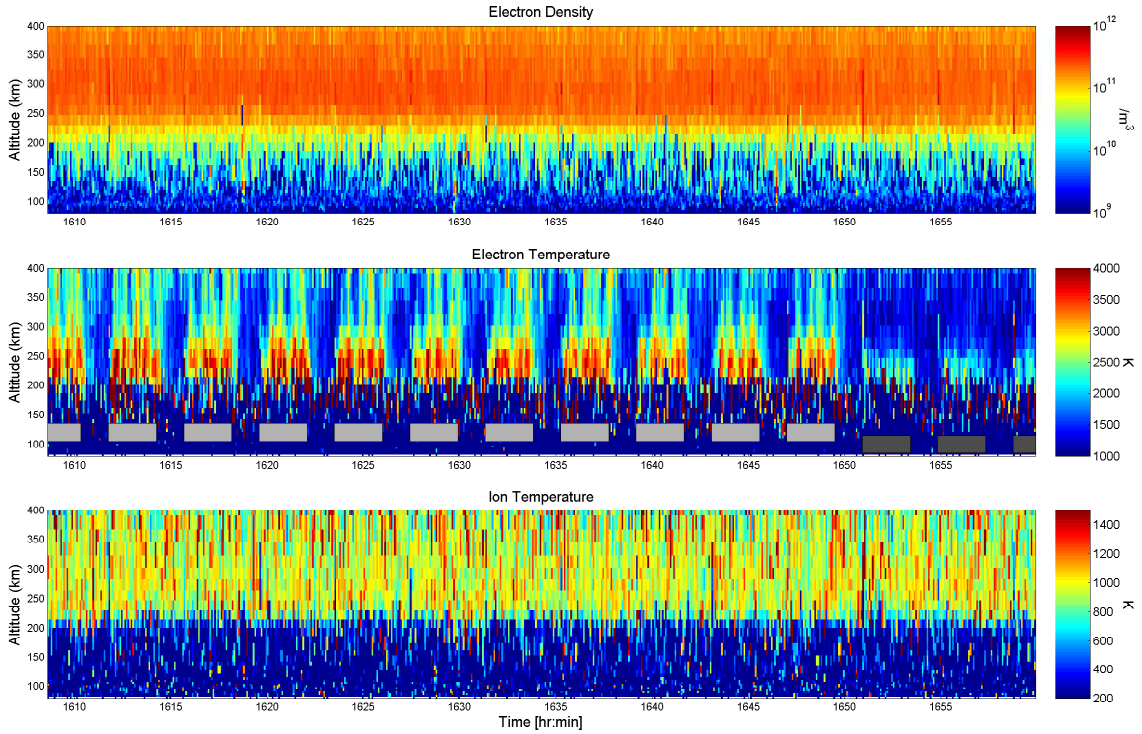

Figure 2.4: The EISCAT-UHF radar measurements of the electron density in the top panel, the electron temperature in the middle and the ion temperature in the bottom panel. The EISCAT-UHF data have been filtered along the time axis with a median filter of length 3 to reduce noise. The time step between each measurement is 5 seconds. The light grey boxes in the electron temperature panel show when transmitting heating at 6.200 MHz. The dark grey boxes shown the same, but with transmitting at 5.423 MHz.

The EISCAT measurements shows a near constant electron densities and ion temperatures. However, the electron temperature is strongly varying, synchronized with the turn on and turn off of the heating. It is also clear that transmitting at 6.200 MHz causes more efficient heating than the 5.423 MHz frequency heating.

2.2 ALIS

The Auroral Large Imaging System (ALIS) consists of six ground based imaging stations located around Kiruna, Sweeden. The main objective of ALIS is to make simultaneous multi station imaging of the aurora, allowing altitude and volume emission estimates of the aurora. Imaging was done at four stations on the 16th of February 2015, in Abisko, Kiruna, Silkimuotka and Tjautjas, respectively. The two remaining stations, Merasjärvi and Nikkaluokta, were not operating at the time of the experiment.
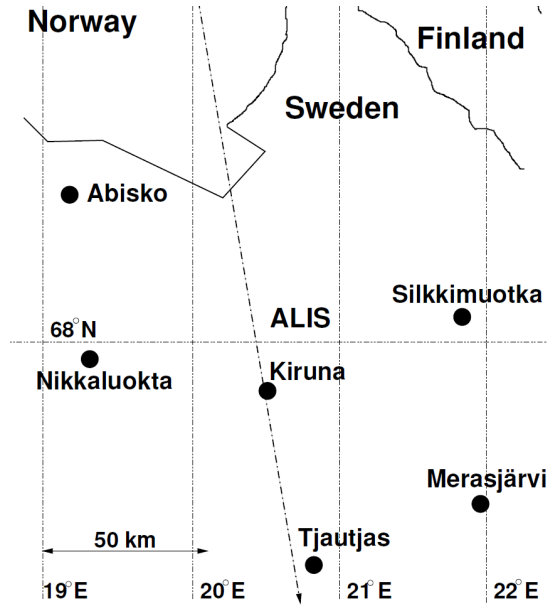

Figure 2.5: The figure show the location of the imaging stations. The stations are positioned around Kiruna with baselines around 50-90 km. The figure is taken from (B. U. E. Brändström et al, 1999). [Brändström et al., 1999]

Each station have a light sensitive high-resolution (1024 x 1024 pixels and 16 bits per pixel) unintensified monochromatic CCD-camera.[Brändström, 2003] The CCD consists of four CCD-chips, providing faster readout speeds. The gain in each pixel was enhanced 16 times by (4 x 4 pixels) binning, (2 x 2 pixels) on-chip binning and (2 x 2 pixels) while doing the data reduction. The binning reduces the image resolution to (256 x 256 pixels). The field-of-view is 90° x 90° for the camera in the Kiruna station, while the other stations have cameras with a 54° x 54° field-of-view.[Brändström et al., 1999] The stations field-of-view is overlapping around the region of heating, approximately 250 km above the ground. An exposure time of 6 seconds was chosen at all stations and for all filters, providing images approximately every 10 seconds.

The stations are equipped with a six-position filter-wheel containing narrow-band filters. [Brändström, 2003] The narrow band filters makes it possible to separate emission from different excitation levels and different excited constituents. This makes it possible to separate the analysis of the auroral emission lines, which will have different peak emission altitude, volume emission distribution and emission intensity. The filters will also reduce light pollution due to the isolation of the emission of interest.

Auroral imaging was done with four filters on the 16th of February 2015. The central wavelength of the filters were 4285 Å, 5590 Å, 6310 Å and 8455 Å and the corresponding filter bandwidths 50 Å, 40 Å, 40 Å and 40 Å. The filters were chosen to capture auroral emission lines with characteristic wavelengths 4278 Å, 5577 Å, 6300 Å and 8446 Å from relaxation of the excited N_2^+1NG, $O(^1S)$, $O(^1D)$ and $O(^3P)$ states.

The filter cycle was initially intended to be similar for all stations. However, this is not exactly the case, as can be seen in figure 2.6 below. First of all, the station in Kiruna did not have the 8455 Å filter for imaging of the 8446 Å emission. Images of the the 8446 Å emission could therefore only be taken by a maximum of three stations. In addition, the 6300 Å imaging at "turn off" were not taken simultaneously with the same filters, the reason for this is unknown. This is a pity since the out of sync images will affect the reliability of the tomographic inversion at "turn off" and the quality of the 6300 Å emission decay estimates.
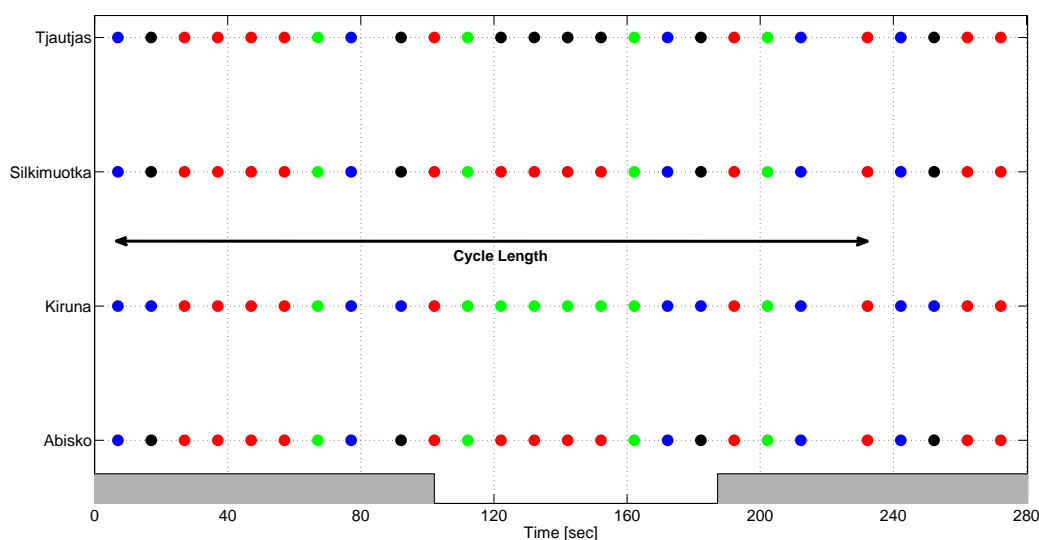
Figure 2.6: The figure show the filter cycle used by the four operational imaging stations. The cycle length is 22 or approximately 235 seconds, for all stations. The blue dots represents images of the 4278 Å emission, the green dots represents the 5577 Å emission, the red dots represents the 6300 Å emission and the black dots represents the 8446 Å emission. The grey areas at the bottom show when the heating was on going, the heating do not start at 0 in the figure, the "turn on" length is 150 seconds. Initially, the idea behind the 6300 Å imaging was to consecutively expose four images to capture the 6300 Å emission during growth and during decay, thus imaging in the middle of "turn on" and "turn off". This was done as intended for the emission growth but was not done successfully for the emission decay, as can be seen in the figure above.

2.3 Experimental Requirements

There are several requirements for a successful ionospheric heating experiment [Brändström et al., 1999]. Why and where in this thesis these requirements are needed is described below.

- **Electron Density** The ionospheric electron density must be high. This is important since the electron density is proportional to the electron acceleration height, more on this relation and the electron acceleration process in chapter 3. If the heating altitude becomes too low, it will cause inefficient heating. The reason being that the increased neutral density at lower altitudes will increase the electron cooling by the increased collision rate between the heated electrons and the cool neutral constituents in the ionosphere. The experiment should therefore be conducted at sunset or in twilight, when the electron density is kept high by the solar radiation flux. Note that the sun will illuminate the ionosphere although it is twilight at sea level. In addition, collisional de-excitation, quenching, will cause the 6300 Å line to faint away at lower altitudes. The radiative lifetime of the excited $O(^1D)$ state is long, 107 seconds, $O(^1D)$ will therefore never have a chance to relax to the ground state and transmit the characteristic 6300 Å emission if the collision frequency becomes too high. The process of quenching and the production of photo emission will be discussed in detail in chapter 4.

- **Sky constrains** In order to acquire good data, it is crucial that the sky is dark and clear. The high sensitivity cameras at ALIS will not be able to detect the heating if the sky background is too bright, the pixels will be saturated by background illumination. Imaging at sunset, in twilight and of course during the night is possible. In addition, clouds will reduce the data quality. Thick clouds will obscure the heating blob leading to useless data. Thin clouds will cause gradients and unwanted features in the projected images of the heating blob, this will lead to a faulty and unreliable tomographic inversion. Images taken under thick or thin clouds can therefore not be used for the purpose of accurately estimating the auroral height or the three dimensional emission distribution. The auroral altitude will be estimated in chapter 8 and a discussion of the tomographic inversion process will be given in chapter 5 and 6.

- **No natural aurora activity** Natural northern lights will have emission similar to the emission of the artificial aurora. Natural aurora will therefore very efficiently pollute the images with unwanted light. In particular, since the natural aurora is not static but constantly evolving with time, it will greatly distort the estimated time evolution of the artificial heating blob, even for faint natural auroras. Hence, there can be no natural aurora activity at the time of the experiment. The time evolution of the volume emission distribution will be reviewed in chapter 8.

- **Stable natural airglow background.** There will always be some background airglow, even if the sky is clear and there is no natural auroral activity. As long as the background airglow is stable it is possible to subtract the slowly varying background and flat-field correct the sky airglow. The background subtraction and flat-field correction procedures is described in the appendix C. A proper background reduction

will be impossible if there are large variations in the natural airglow. It is therefore required that the natural airglow background is stable.

All the requirements presented above were fulfilled on the 16th of February 2015 between 16.38 UT and 16.58 UT at EISCAT and at least three ALIS stations. This thesis will therefore focus on the data from this time regime.

Ionospheric Heating Theory

3.1 Ionospheric Absorption Of HF Radio Waves

Understanding how HF radio waves produces emission in the ionosphere has been one of the one of the major motivations for conducting heating experiments during the last decades. A key element for understanding the heating process is to accurately determine the RIOE (Radio Induced Optical Emission) volume distribution. EISCAT RIOE observations have shown that the maximum emission enhancement will occur approximately 10 km below the reflection height[1] for the 6300 Å emission and about 25 km below the relfelctrion height for the 4278 Å, 5577 Å and 8446 Å emissions [Gustavsson and Eliasson, 2008] and [Gustavsson et al., 2001]. The plasma oscillation frequency, which defines the reflection height, is given by:

$$f_p = \frac{1}{2\pi} \cdot \sqrt{\frac{n_e e^2}{\epsilon m_e}} \qquad (3.1)$$

Where m_e is the electron mass, e elementary electron charge and ϵ is the vacuum permittivity.

The height of the electron heating is therefore defined by the frequency of the transmitted radio waves, f_0, and the aquare root of the ionospheric electron density. In addition, it is known from [Kosch et al., 2002] and [Gustavsson et al., 2006] that the electron heating efficiency is dependent on the relationship between the transmitted heating frequency, the electron gyro-harmonic frequencies and the plasma frequency. This relationship is not fully understood yet. However, it has been observed that heating with frequencies close to a multiple of the electron gyro-frequency, f_e, at approximately the upper-hybrid

---

[1]The reflection height is the height where the transmitted frequency equals the plasma frequency. If a radio wave reaches the reflection height, it will be reflected or refracted back towards ground. Note that this is not due to plasma fluctation scattering, as for the EISCAT UHF backscattering, but due to interactions with electrons which are oscillating with the same frequency as the O-mode radio waves.

resonance height gives efficient heating response. Wheras heating at the hight where a multiple of the electron gyro frequency equals the upper hybrid frequency, f_h, suppresses the heating efficiency [Kosch et al., 2002] and [Gustavsson et al., 2006]. The Equations for the electron gyro-frequency and the upper hybrid frequency are given below:

$$f_e = \frac{|q|B}{m_e} \tag{3.2}$$

B is the magnetic field strength, the other parameters are defined as before.

$$f_h = \sqrt{f_p^2 + f_e^2} \tag{3.3}$$

The figure below shows the estimated frequencies gives from equations 3.1, 3.2 and 3.3. The electron density n_e is taken from the EISCAT electron density measurements, averaged over the entire heating period. Values of the altitude dependent magnetic field field strength are taken from the International Geomagnetic Reference Model [Finlay et al., 2010].
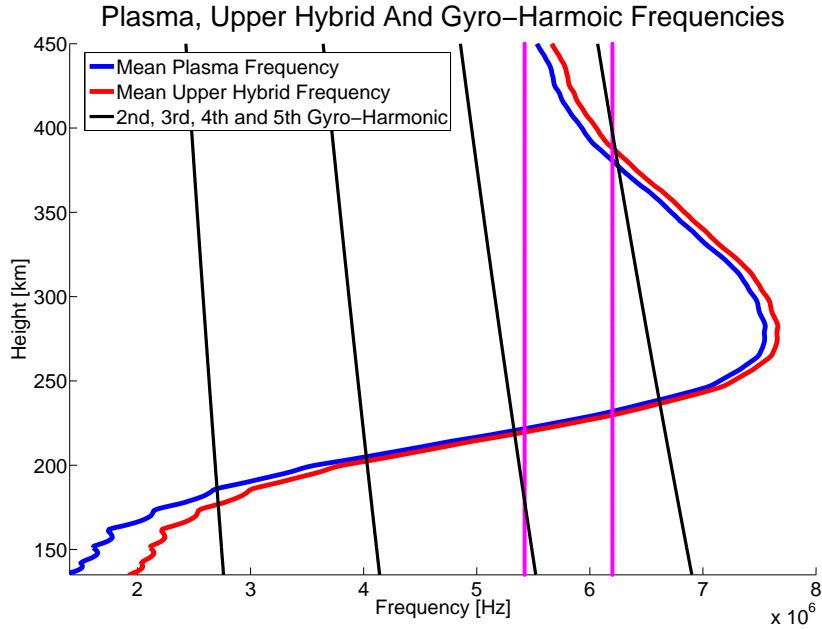
Figure 3.1: The figure above shows the plasma, the upper-hybrid and the electron gyro-harmonic frequencies. The magenta lines represents the transmitted heating frequencies. The point of maximum heating should be close to the intersection between the heating frequency and the upper-hybrid frequency. It is clear, by looking at the intersection points in the figure, that the fall in electron heating height seen in figure 3.2, is due to the transmitted frequency change from 6.200 MHz to 5.423 MHz.

HF heating experiments during the last decades have shown that the transmitted HF radio waves do energize ionospheric electrons which causes excitation of atoms and molecules. However, the underlying mechanism for energizing the electrons has been under debate. There are two main theories explaining the RIOE, the thermal electron excitation theory [Mantas, 1994] and the accelerated electron excitation theory

16

[Bernhardt et al., 1989]. The two theories will be described in the following sections. The results from the tomographic aurora reconstruction will later be compared to the theoretical predictions of the aurora.

3.2 The Thermal Electron Excitation Theory

The thermal electron excitation theory was first presented in the paper [Mantas, 1994]. The paper is based on electron density, electron temperature and 6300 Å emission data from ionospheric heating experiments at Arecibo, Puerto Rico. Mantas argues for that the observed RIOE is almost entirely produced by thermally heated electrons and that emission induced by electron acceleration is a rare phenomenon [Mantas, 1994]. The electrons are energized by anomalous and joule heating immidiatly below the reflection height [Mantas and Carlson, 1996]. Hence, the thermal heating theory predicts excitation of ionospheric neutrals exclusively from the high energy tail of a Maxwellian electron energy distribution. The Maxwellian electron energy distribution can be approximated from the measured EISCAT temperatures.
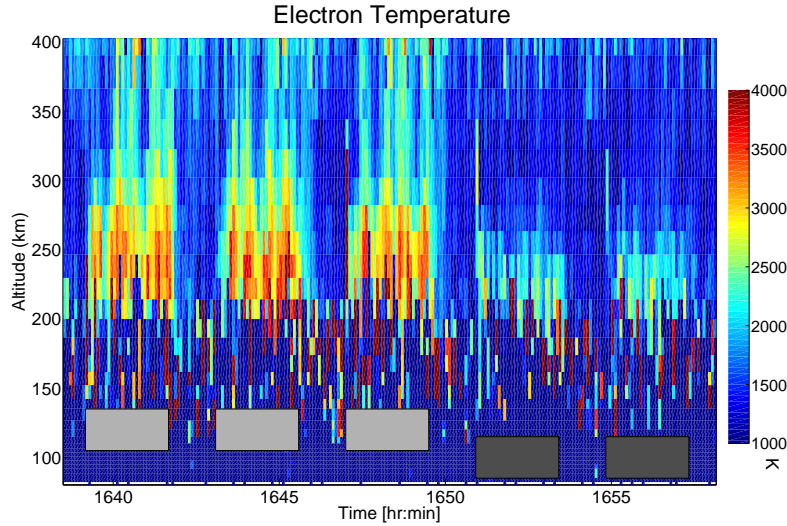
Figure 3.2: The figure shows the measured EISCAT temperatures, the figure is similar to 2.2, but zoomed in on the time region of interest.

The peak electron temperature can be approximated to 3300 K at 240 km for heating at 6.200 MHz and 2500 K at 220 km for 5.423 MHz heating. The Maxwellian energy distribution is given by:

$$f_E(E) = n_e \cdot 2\sqrt{\frac{E}{\pi}} \left(\frac{1}{kT}\right)^{3/2} \exp\left(\frac{-E}{kT}\right) \tag{3.4}$$

The energy distributions shown in figure 3.4 are calculated by using equation 3.4 and the approximated electron temperatures.

17
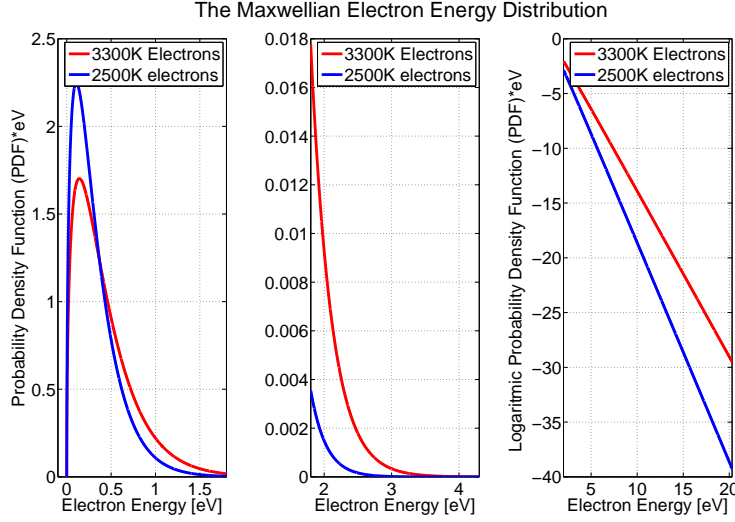
Figure 3.3: The figures shows the Maxwellian electron energy distributions for 3300 K and 2500 K electrons. To the left, the bulk electron energy distribution. The energy range of interest for exciting the $O(^1D)$ and $O(^1S)$ states are shown in the middle figure. The rightmost figure shows the high energy tail, from 2 eV to 20 eV, with a logarithmic probability density function.

The thermal electrons with enough energy to excite the $O(^1D)$, $O(^1S)$, $O(^3P)$ and N_2^+1NG states needs to come from the high energy tail of the Maxwellian electron energy distribution. The energy thresholds for excitation are (1.96 eV), (4.17 eV), (10.99 eV) and (18.75 eV) respectively. The proportion of electrons with energies above the threshold energy is given in the table below:

Excited State	Wavelength	Threshold Energy	Proportion 3300 K	Proportion 2500 K
$O(^1D)$	6300 Å	1.96 eV	0.0032	$4 \cdot 10^{-4}$
$O(^1S)$	5577 Å	4.17 eV	$1.90 \cdot 10^{-6}$	$1.98 \cdot 10^{-8}$
$O(^3P)$	8446 Å	10.99 eV	$1.15 \cdot 10^{-16}$	$5.60 \cdot 10^{-22}$
N_2^+1NG	4278 Å	18.75 eV	$2.09 \cdot 10^{-28}$	$1.63 \cdot 10^{-37}$

Table 3.1: The proportion of electrons with energies above the threshold energy of the excited states. In column four, the proportion from the 3300 K Maxwellian, and in the rightmost column the proportion from the 2500 K electron energy distribution.

From [Gustavsson et al., 2002], it was shown that by using thermal $O(^1D)$ and $O(^1S)$ excitation rate estimates, it is possible to find an analytical approximation of the steady state 5577 Å and 6300 Å emission intensity ratio:

$$q(T_e) = \frac{2(19960 + T_e)(51813 + T_e)^3 exp(-\frac{-25634}{T_e})}{5(9329 + T_e)A_{6300}\tau_{O(^1D)}(114080 + T_e)^3} \tag{3.5}$$

$A_{6300} = 0.00071s^{-1}$ is the transition probability from $O(^1D)$ to the ground state. $\tau_{O(^1D)}$ is the effective $O(^1D)$ lifetime at the altitude of the HF-excited emission lines.

18

The $O(^1D)$ lifetime accounts for the collisional de-excitation rate and the radiative de-excitation rate.

Equation 3.5 will be used later for comparing the observed 5577 Å and 6300 Å intensity ratios and the emission intensity ratio predictions from the thermal electron excitation theory. It is not expect that emission from de-excitation of $O(^3P)$ and the N_2^+1NG can be isolated from the background emission during the six second exposures. Their threshold energies of 10.99 eV and 18.75 eV are too high for the 3300 K and 2500 K Maxwell energy distributed electrons to produce an observable amount of emission in the 8446 Å and 4278 Å lines [Gustavsson and Eliasson, 2008].

3.3   The Accelerated Electron Excitation Theory

The accelerated electron theory has been the leading theory for explaining the radio induced emissions over the last decades. The theory do not assume an Maxwellian electron energy distribution. Instead, it argues that the transmitted HF radio wave will accelerate supra-thermal electrons. The electron energy distribution of the accelerated electrons will therefore deviate from the thermal model. Numerical studies has shown that the deviation is especially significant in the high energy tail [Stubbe, 1981]. At high latitudes and when transmitting O-mode HF radio waves antiparallell to the magnetic zenith, it is believed that the electron acceleration is caused by upper hybrid turbulence [Kosch et al., 2002].

3.3.1   Upper Hybrid Resonance And Plasma Cavities

The upper-hybrid resonance is excited by self focusing of the HF-radio waves within magnetic field-aligned plasma striations. This will happen just above the critical altitude of the upper-hybrid (UH) frequency [Eliasson and Papadopoulos, 2015]. The UH waves will increase the plasma pressure within the striations and therefore expand the small scale striations into bigger scale plasma cavities, with sizes from a few meters to a few kilo meters [Eliasson and Papadopoulos, 2015] and [Gondarenko et al., 2005]. The plasma cavities will then cause more efficient self-focusing of the HF waves and increase the strength of the upper hybrid turbulence.
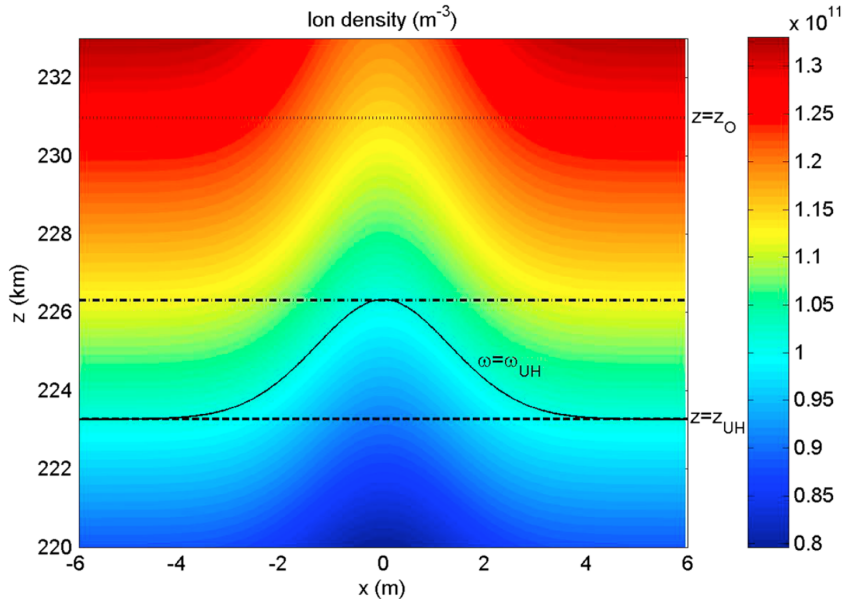
Figure 3.4: The figure displays the theoretical spatial profile of a plasma density striation. The dashed bottom line indicates the the UH altitude outside the striation, the solid line represents the effective UH altitude. The effective UH altitude will rise within the plasma striation. When the transmitted heating waves reaches the striation they will be focused by the density gradient and get trapped inside the striation. The trapped waves will then energize the upper-hybrid turbulence, increasing the plasma pressure and therefore the striation size. The figure is taken from [Eliasson and Papadopoulos, 2015].

Numerical simulations have shown that the upper hybrid plasma waves makes an efficient source of accelerating electrons [Gondarenko et al., 2005], explaining the observed enhanced emission. In [Bernhardt et al., 1989], Bernhardt et al. tried to relate observed 6300 Å and 5577 Å emissions at Arecibo, Puerto Rico, to an accelerated electron energy distribution profile. However, this relationship is not completely understood yet. It is important to find a good model for the electron energy distribution in order to understand more of the relationship between electron acceleration and the observed emission. This is an interesting objective which will be described in the next section.

3.3.2 The Accelerated Electron Energy Distribution

Finding a good estimate of the electron energy distribution during HF heating has been one of the main objectives within the field of ionospheric heating during the last years. In this thesis, the accelerated electron energy distribution from [Gustavsson and Eliasson, 2008] will be used. The electron energy distribution was determined by minimizing the weighted least square difference between observed and modelled emission enhancements. The 4278 Å, 5577 Å, 6300 Å and 8446 Å emissions were observed. The corresponding modelled enhancements were estimated by an electron transport model with a parametrized acceleration term and an electron acceleration midpoint at the upper hybrid resonance height. The transport of electrons with energies between 2-100 eV was simulated by a downward and an upward electron flux. Electrons with energies below 2 eV were not simulated,

since they are unable to produce emission through excitation of ionospheric constituents. The model takes self-focusing of the HF waves, the amplitude of the upper hybrid waves and the loss of energy due to collisional excitation of N_2 vibrational states into consideration. The figure below shows the energy-flux distribution, it is beyond the scope of this thesis to go further into how these distributions were acquired.
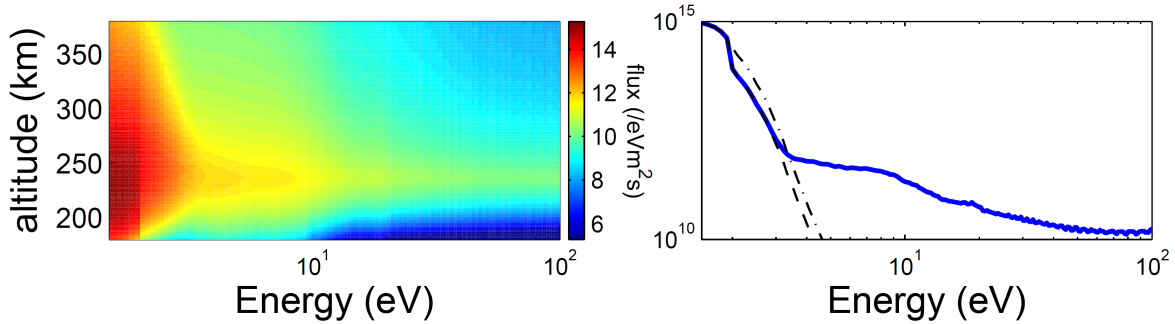
Figure 3.5: To the left, the figure shows the altitude energy variation of the electron flux from an electron acceleration altitude of 236 km. To the right, the electron flux as a function of energy at the acceleration altitude (236 km) and the corresponding thermally estimated electron flux in the black dash-dotted line. The black dashed line is the thermal electron energy distribution corrected for the energy loss to excitation of N_2 vibrational states. The figure is taken from [Gustavsson and Eliasson, 2008].

From the energy-flux distributions, Gustavsson estimated the excitation rate distributions for the $O(^1D)$, $O(^1S)$, $O(^3P)$ and N_2^+1NG states. This was achieved by using published cross sections, reaction rates and the MSIS neutral density model [Hedin, 1991]. Gustavsson estimated excitation rate altitude profiles for a range of electron acceleration heights. The modelling of the electron flux provided characteristic hight centrers and widths for the different emission lines at different acceleration altitudes. This is shown in the figures below:
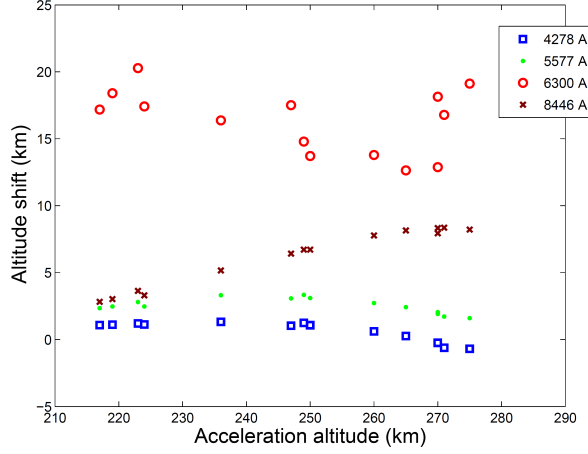
Figure 3.6: The figure show the altitude shift of the emission centre from the electron acceleration center. The significant upward shift in the 6300 Å emission is caused by the neutral density gradient. The long-lived $O(^1D)$ states will undergo collosional de-excitation in addition to radiative de-excitation. The colliosional de-excitation reate is proposional to the neutral density, causing more loss of radiative de-excitation at lower altitudes and therefore causing the upward shift of the radiated photons. The figure is taken from [Gustavsson and Eliasson, 2008].
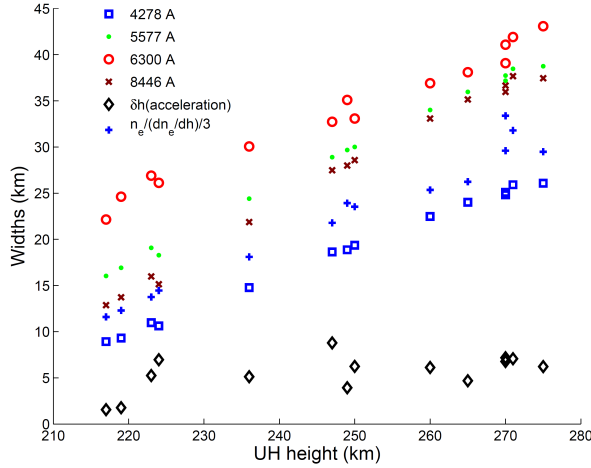
Figure 3.7: The width of the emission increases with altitude, as a consequence of the increasing mean free path of the electrons. In addition, the width of the emission gets smaller with higher excitation treshold energies. This is as expected, assuming that electrons further away from the acceleration center will have less energy, due to inelastic collisons, than electrons closer to the acceleration center. The blue crosses represents the electron scale height devided by three. The figure is taken from [Gustavsson and Eliasson, 2008].

The excitation rate profiles, provided by [Gustavsson and Eliasson, 2008], will be used later in this thesis to construct the modelled auroral emission distribution, via tomo-

graphic reconstruction of the observed RIOE. In addition, the height and width of the modelled emission volumes will be compared to the predictions in figures 3.6 and 3.7.

The Four Emission Lines

Before choosing how to construct the modelled aurora, it is beneficial to study the ionospheric excitation processes and the emission enhancements and appearances. The excitation processes, causing the 6300 Å, 5577 Å, 8446 Å and 4278 Å emissions, will be described briefly in this chapter. The discussion which is given here is based on more thorough descriptions given in [Gustavsson, 2000] and [Gustavsson and Eliasson, 2008]. An understanding of the auroral intensities, appearances and excitation processes will make it easier to determine the constrains and parameters which are need to construct a physically feasible model of the artificial aurora.

4.1 The Auroral Red Line - 6300 Å

The auroral red line can sometimes be seen in the upper border of natural auroras [Gustavsson, 2000]. For artificial auroras, induced by EISCAT heating, it is the strongest emission line. The 6300 Å emission is about 3 times stronger during heating at 6.200 MHz than during heating at 5.423 MHz. The emission enhancements are shown in the figures below:
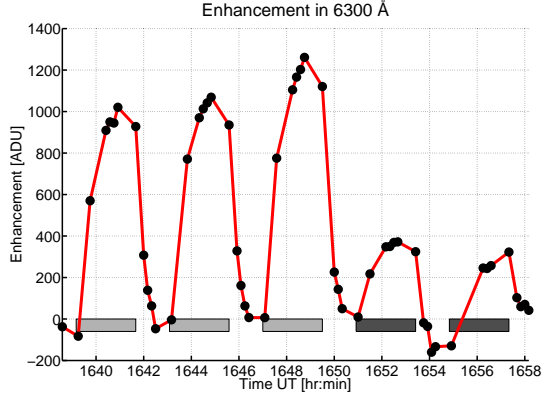
(a) Enhancement observed in Abisko
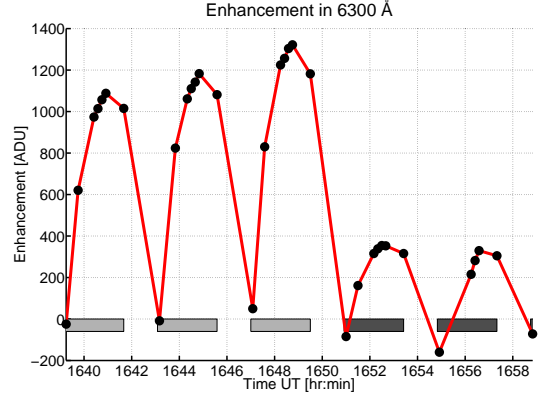
(b) Enhancement observed in Kiruna
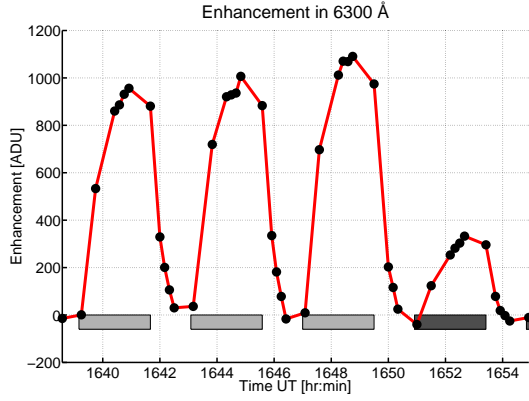
(c) Enhancement observed in Silkimoutka
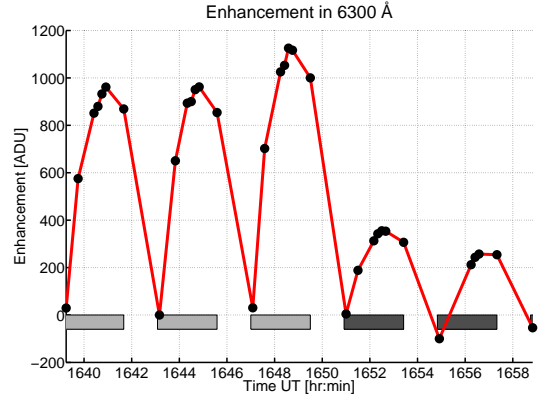
(d) Enhancement observed in Tjautjas

Figure 4.1: The enhancements are estimated by the averaged pixel value of a (10 x 10) pixel area over the point of maximum enhancement. The light-grey boxes represents the times when the 6.200 MHz heating was ongoing, the dark-grey boxes represents the times at 5.423 MHz heating. Images were only taken up to 16:55 in the Silkimoutka station. Note that this is the emission enhancements after background subtraction and flat-field correction, as described in appendix C.

The 6300 Å emission is caused by de-excitation of $O(^1D)$, the lowest excited electronic atomic oxygen state, to the ground state $O(^3P_2)$. The major sources of the $O(^1D)$ states are listed below:

- The main source in the quiet F region is excitation by dissociative recombination of O_2^+ [Gustavsson and Eliasson, 2008]:

$$O_2^+ + e \rightarrow O + O(^1D) \tag{4.1}$$

- Excitation by direct electron collisions with atomic oxygen:

$$O + e^- \rightarrow O(^1D) + e^- \tag{4.2}$$

- A small contribution also comes from de-excitation of $O(^1S)$:

$$O(^1S) \rightarrow O(^1D) + h\nu_{5577} \tag{4.3}$$

26

The treshold energy of the $O(^1D)$ state is 1.96 eV. The $O(^1D)$ state is meta-stable and has a radiative lifetime of 107 seconds. The long radiative lifetime causes collisional de-excitation, quenching, to become a significant effect. When the $O(^1D)$ excited states collides with molecular oxygen and nitrogen, the potential energy of the excited electron might get lost, without emitting photons. The energy is lost to an increase in the kinetic, vibrational or rotational energies of the colliding particles. The collisional de-excitation effect will increase with lower altitudes, due the neutral density gradient. In other words, a denser atmosphere will cause more collisions and hence less radiative $O(^1D)$ de-excitation. The neutral densities and the theoretical effective mean lifetime of the $O(^1D)$ state, before de-excitation, as a function of altitude is shown below in figure 4.2.
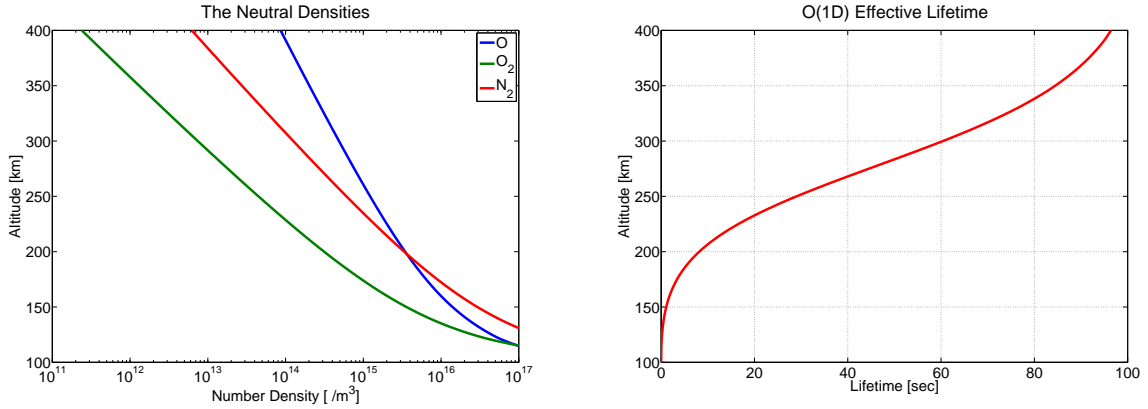
Figure 4.2: To the left, the logarithm of the neutral densities as a function of height, the density values are from the MSIS neutral density model [Hedin, 1991]. To the right, the theoretical effective mean lifetime of the $O(^1D)$. A typical emission altitude in evening twilight is 240 km for the 6300 Å emission. This corresponds to an effective lifetime of 24 seconds. The lifetimes are calculated using the MSIS neutral density model and reaction rates from personal contact with B. Gustavsson.

An effective lifetime of 24 seconds is still relatively long, compared to the imaging frequency, 10 seconds in between consecutive images. Hence, the effective lifetime, the drift and the diffusion of the $O(^1D)$ states needs to be taken into consideration when modelling the 6300 Å emission. How the modelling accounts for these factors will be thoroughly described in section sec:modelling.

4.2   The Auroral Green Line - 5577 Å

The auroral green line is generally the brightest emission line in the natural northern lights. It is the second strongest emission line for the artificial auroras studied in this thesis. The 5577 Å emission enhancements are shown in the figures below:
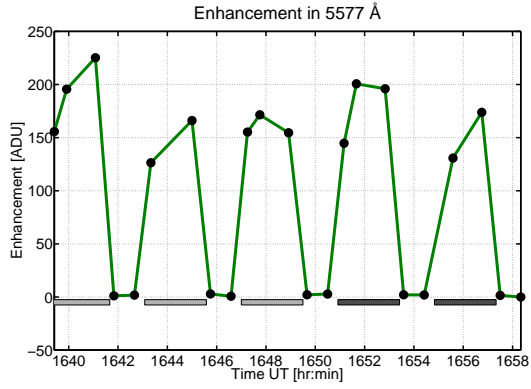
(a) Enhancement observed in Abisko
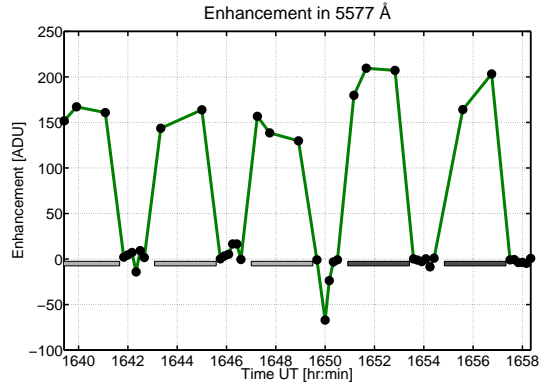
(b) Enhancement observed in Kiruna
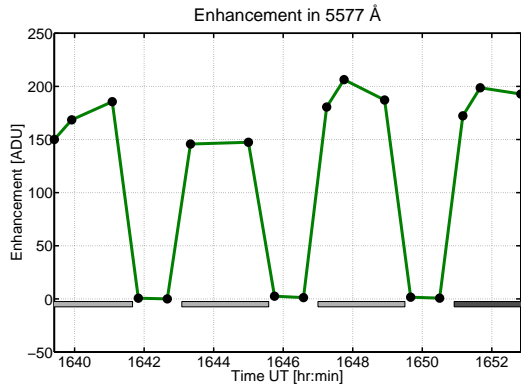
(c) Enhancement observed in Silkimoutka
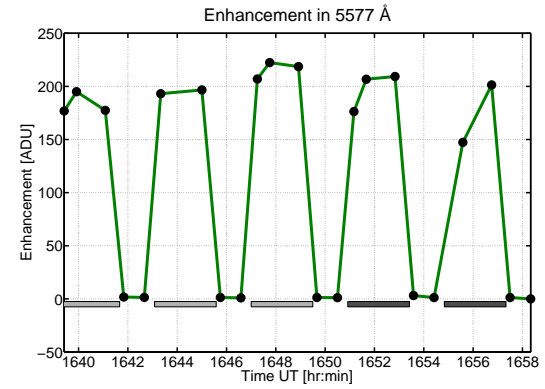
(d) Enhancement observed in Tjautjas

Figure 4.3: The 5577 Å enhancements are estimated similarly to the red line enhancements, see figure 4.1. The enhanced count values are estimated from the background reduced images.

The 5577 Å emission is, like the 6300 Å emission, caused by atomic oxygen. The 5577 Å emission is emitted when the second lowest electronic excitation state $O(^1S)$ relaxes to the lowest electronic excitation state $O(^1D)$. The two main sources of $O(^1S)$ are listed below [Gustavsson and Eliasson, 2008]:

- The main source in the F region is excitation by direct electron collisions with atomic oxygen:

$$O + e^- \rightarrow O(^1S) + e^- \tag{4.4}$$

- Excitation by energy transfer from the $N_2(A^3\Sigma_u^+)$ state:

$$N_2(A^3\Sigma_u^+) + O \rightarrow N_2 + O(^1S) \tag{4.5}$$
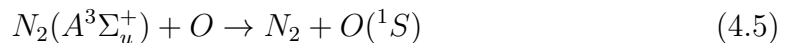
The $O(^1S)$ excitation state has a treshold enegy of 4.17 eV and is considered matastable. However, the radiative lifetime is only 0.7 seconds. Hence, the effect of quenching can be ignored in the F region modelling og the 5577 Å emission [Gustavsson et al., 2002].

4.3 The Auroral Near Infra-Red Line - 8446 Å

The near infra-red emission line is not visible by the naked eye. However, the ALIS CCD-cameras can detect the 8446 Å emission. It is the third strongest emission line, induced by EISCAT heating. It is stronger during the 5.423 MHz heating than during the 6.200 MHz heating, by a factor of 2 approximately.

(a) Enhancement observed in Abisko

(b) Enhancement observed in Silkimoutka

(c) Enhancement observed in Tjautjas
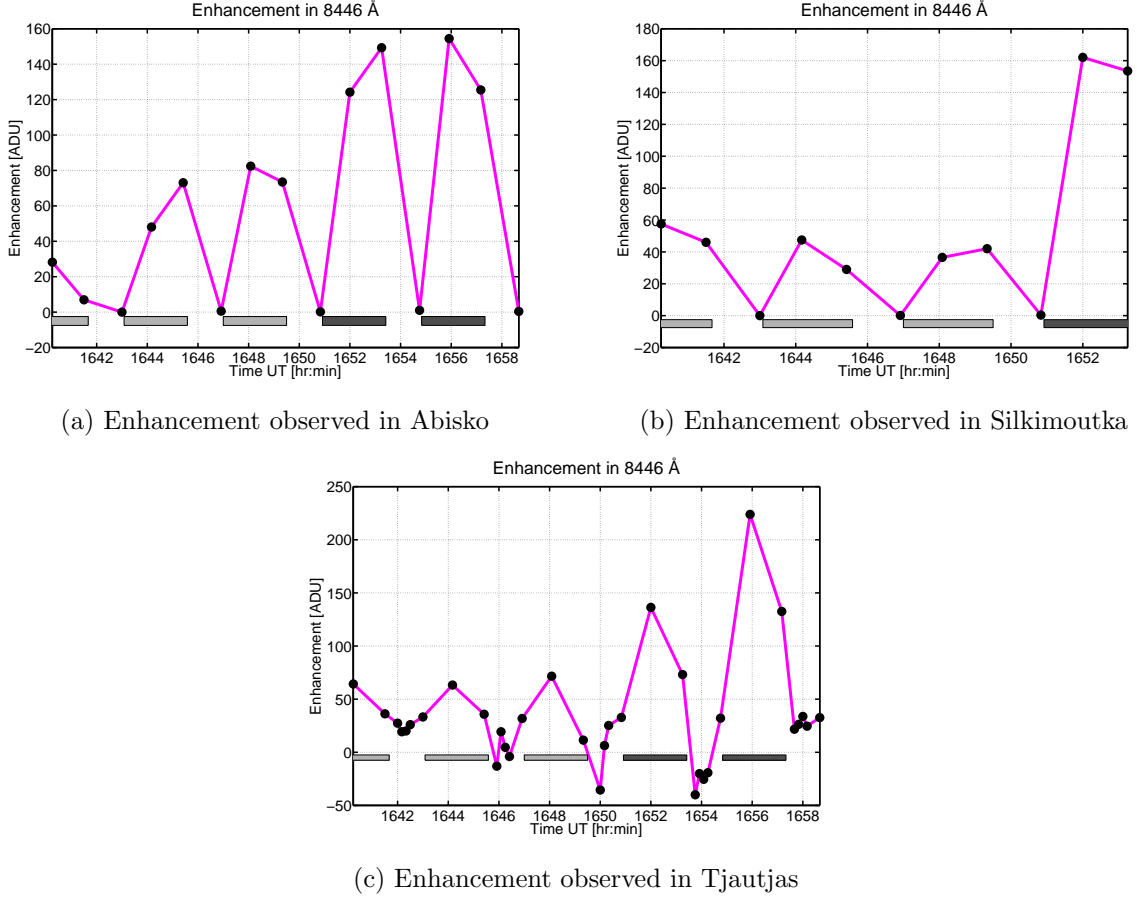
Figure 4.4: The 8446 Å enhancements are estimated similarly to the red line enhancements in figure 4.1. Note that no 8446 Å images were taken in the Kiruna station. The enhancements are calculated from the background reduced images.

The 8446 Å emission is caused by the transition $O(3p^3P) \rightarrow O(3s^3S)$. The main source of $O(3p^3P)$, which is shortened to $O(^3P)$ in this thesis, is from direct electron impact on atomic oxygen [Gustavsson, 2000]:

$$O + e^- \rightarrow O(^3P) + e^- \tag{4.6}$$

The threshold energy for excitation of the $O(^3P)$ state is 10.99 eV. The $O(^3P)$ state is not meta-stable and will emit a photon almost immediately after excitation. Collisional de-excitation, drift and diffusion will therefore be ignored in the modelling of the 8446 Å emission.

4.4 The Auroral Blue Line - 4278 Å

The auroral blue line can only bee seen at the bottom of strong auroral arcs. The 4278 Å line is the weakest emission line observed during the heating experiment. There are no enhancements during the 6.200 MHz heating and only small observable enhancements during 5.423 MHz heating. The enhancement plots are shown in the figures below:

(a) Enhancement observed in Abisko

(b) Enhancement observed in Kiruna

(c) Enhancement observed in Silkimoutka

(d) Enhancement observed in Tjautjas
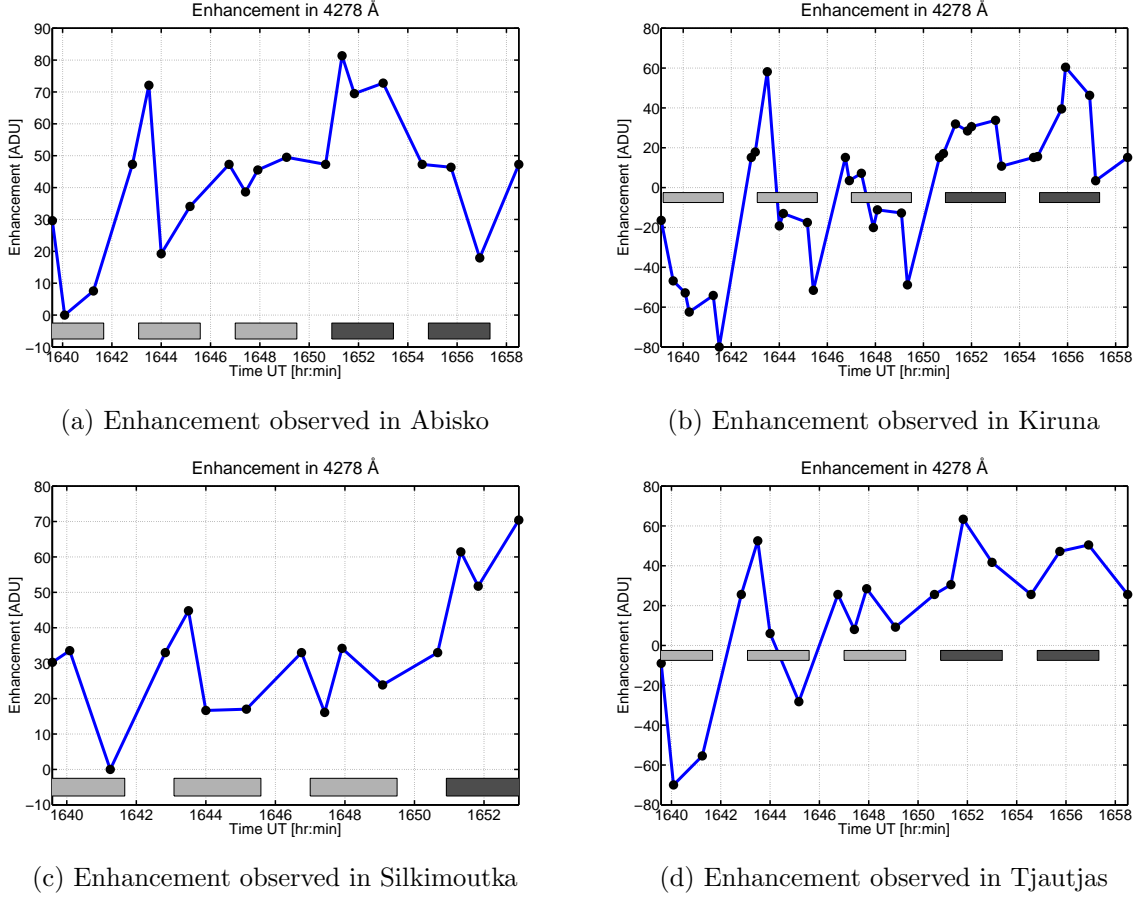
Figure 4.5: The only enhancement that can be isolated from the natural airglow variations, in at least 3 stations, is the enhancement during the 16:52 heating pulse. The 4278 Å enhancements are estimated similarly to the red line enhancements, see figure 4.1. The enhanced count values are estimated from the background reduced images.

The auroral blue line is caused by ionized molecular nitrogen. The 4278 Å photon is emitted by the transition of the $N_2^+ 1NG$ sate to the first vibrational level of the electronic ground state of the molecular nitrogen ion, $N_2^+(X^2\Sigma_u^+)$ [Gustavsson, 2000] . The main source of excitation of $N_2^+ 1NG$ is direct electron impact:

$$N_2 + e^- \rightarrow N_2^+ 1NG + 2e^- \tag{4.7}$$

The excited $N_2^+ 1NG$ sate has a threshold energy of 18.75 eV and is not meta-stable. Hence, it is assumed in the 4278 Å modelling that all the $N_2^+ 1NG$ states will transmits a photon directly after excitation. The lifetime, drift and diffusion of the $N_2^+ 1NG$ states can therefore be ignored in the auroral simulations. However, the emission enhancements

are too weak for tomographic reconstruction. The 4278 Å emission data will therefore not be used further in this thesis.

4.5 The Auroral Appearance

The auroral 6300 Å line is the strongest emission line, and will therefore be to make initial assumptions about the auroral appearance. In the parper [Gustavsson et al., 2001], two emission emission centres were observed in 6300 Å, causing a more complex model of the three dimensional volume emission rate. This demonstrates that it is important to have a first glance at the observed images before preforming the tomographic reconstruction. Below is a figure showing the growth and decay of the 6300 Å emission.

The Auroral Appearance
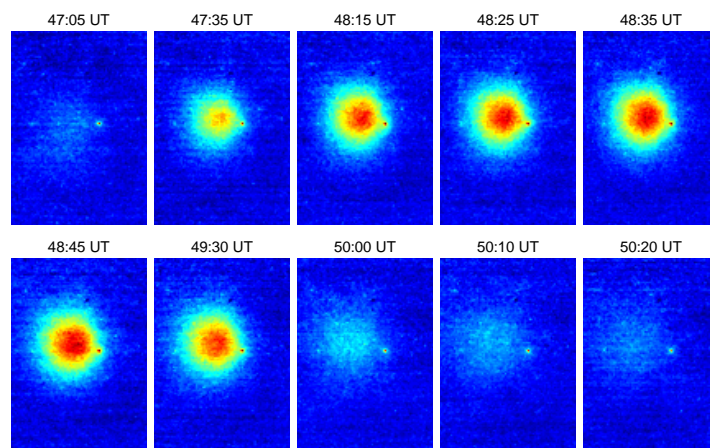
(a)
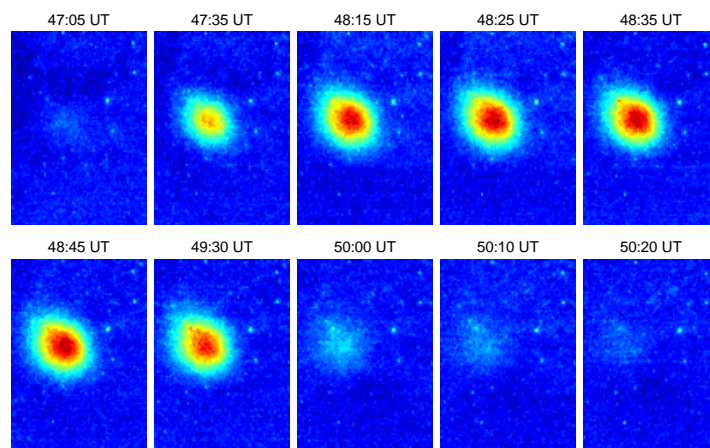
(b)

Figure 4.6: The figure shows the simultaneous images from one heating cycle, observed in Abisko,figure (a), and in Silkimoutka, figure (b). It is apparent from the images that there is only one emission center. The speckles in the images are stars. Note that these images are background reduced and flat field corrected, as described in appendix C.

The emission blob in figures (a) and (b) appears rather round in the projected images, this is not required since wind, diffusion and the neutral density gradient will distort the blob shape. The round shape is also seen at the other stations and for all pulses and filters, with a clearly defined enhanced emission. The 6300 Å emission blob, within the full frame image at all stations is shown in figure C.3, and the fitting between the emission count distribution and a Gaussian distribution is shown in figures C.13 and C.14. This indicates that the electrons moves isotropically from the heating/acceleration center in the near-horizontal plane. Hence, a Gaussian excitation distribution in the horizontal plane will be an adequate starting point in the auroral modelling construction. It is difficult to obtain information about the energized electron density distribution in the vertical plane, since all the imaging stations are underneath and south of the enhanced emission blob. It is expected that the mean free path of the electrons is longer above than below the heating center, due to the neutral density gradient. This is taken into consideration in the accelerated electron excitation profiles described in chapter 3. The vertically asymmetric electron distribution shape will also be taken into account when modelling the aurora without the use of the excitation profiles.

Auroral Construction and Modelling

5.1   Tomographic Inversion

The objective of tomographic inversion is to reconstruct the three dimensional distribution of an object from a set of projections, i.e. images.[Gustavsson, 1998] This is an inverse problem, since we start with the the images and desire to find the volume distribution causing them. However, the tomographic reconstruction of the aurora is different from the tomographic reconstruction of for example the brain or a tumour in the body. In most uses of tomography, there are numerous images taken around the object of interest, as for PET (Positron Emission Tomography) and X-ray CT (Computed Tomography) scanning. This is not the case for auroral imaging with ALIS. ALIS has only four operational imaging stations and they are all south and underneath the object of interest. This makes the imaged projections of the artificial aurora close to being linearly dependent [Gustavsson, 2000]. Conventional analytical methods can therefore not be used for describing the mathematical structure of our inverse problem. Hence, the Fredholm integral equation 5.1 can not be used. There will always be spatial structures in the three dimensional emission distribution that are "invisible" for ALIS.

$$\boldsymbol{I}(\bar{r}_s) = \int \boldsymbol{K}(\bar{r}_s, \bar{r}') f(\bar{r}') d\bar{r}' \tag{5.1}$$

$\boldsymbol{I}(\bar{r}_s)$ is the observed projections, $f(\bar{r}')$ is the unknown object's emission distribution and $\boldsymbol{K}$ is the Fredholm operator. The Fredholm operator defiens the transformation that projects emission from the object down to the images.[Gustavsson, 1998]

In this thesis, the volume distribution of the aurora will be determined by modelling, since the 3D distribution can not be found analytically. This is in practice done by constructing a modelled aurora, projecting the constructed aurora down to modelled images and then comparing the modelled and observed images. Comparisons of the "real" aurora projections (the observational images) and the "simulated" aurora projections (the modelled images), will determine the credibility of the model. This is done by minimizing a

modified version of the least square minimum. The techniques used for constructing and modelling the aurora will be described in this chapter. Chapter 6 will explain how the modelled aurora is projected down to the modelled images. The methods for comparing the modelled and observed images and determining the model reliability will be described in chapter 7.

5.2   Constructing The Excitation Distribution

Three different auroral construction techniques will be investigated in this thesis, theoretical curves, semi-theoretical curves and free parameter search. The theoretical curves are the excitation rate profiles described in subsection 3.3.2. The excitation rate profiles were generated by the accelerated two stream electron transport model, published in [Gustavsson and Eliasson, 2008]. The normalized excitation rate profiles from a range of excitation center heights were provided by personal contact with B. Gustavsson. The three construction techniques, theoretical curves, semi-theoretical curves and free parameter search are described below:

- **1. Theoretical Curves** The modelled aurora will be built up based on theoretical excitation predictions. The normalized theoretical excitation rate curve, I_{z0}, is the excitation rate profile with an electron excitation center at altitude z_o. The normalized excitation rate profile $I_{z0}(z)$ is a function of altitude, z. I_0 is the maximum excitation value, estimated over six second to match the exposure time of the observed images. The center of the excitation volume (x_0, y_0, z_0), is defined by the location of I_0. It is assumed that the excitation is Gaussian distributed in the horizontal plane $G(x, y, \sigma_r)$, where σ_r is the horizontal radius from the excitation center. The radius is defined by the $\pm\sigma$ $68th$ percentile, i.e. 68 per cent of the excitation lies within the radius σ_r in the horizontal plane. This gives the theoretical excitation volume function,$f^T(x, y, z)$, given by:

$$f^T(x, y, z) = I_0 \cdot I_{z0}(z) \cdot exp\left(- \left(\frac{(x - x_0)^2}{2\sigma_r^2} + \frac{(y - y_0 - (z - z_0)sin(\theta))^2}{2\sigma_r^2} \right) \right) \quad (5.2)$$

θ is the magnetic field angle from zenith, i.e. 12 degrees south at Ramfjorden.

- **2. Semi-Theoretical Curves** The theoretical curves and the Gaussian shaped distribution is used to construct the excitation volume, as in (1.). However, a shape parameter (γ) is applied on the normalized excitation rate curves, I_{z0}^{γ}. A low gamma value ($\gamma < 2$) will sharpen the excitation rate curves around the peak excitation, meaning that the emission will be produced within a thinner layer. A high gamma value ($\gamma > 2$) will make the curves more blunt. In addition, the excitation distribution is now allowed to be asymmetric in the horizontal plane, $G(x, y, \sigma_x, \sigma_y)$, where σ_x and σ_y are the independent widths of the excitation along the x and y-axis, as defined by the one $\pm\sigma$ $68th$ percentile. Hence, 68 percent of the excitation along the x and y-axis lies within $\pm dx$ and $\pm dy$. The rotation of the asymmetric excitation volume in the xy-plane is determined by an additional parameter ϕ. The semi-theoretical excitation function is given by:

$$f^S(x,y,z) = I_0 \cdot I_{z0}^\gamma \cdot exp\bigg(-\bigg(\frac{((x-x_0)cos(\phi)+(y-y_0)sin(\phi))^2}{2\sigma_x^2}$$
$$+ \frac{((y-y_0-(z-z_0)sin(\theta))cos(\phi)-(x-x_0)sin(\phi))^2}{2\sigma_y^2}\bigg)\bigg) \tag{5.3}$$

- **3. Free Parameter Search** There will be no theoretical curves defining the excitation rate as a function of height. The excitation blob will instead be constructed using Gaussian distributions along all axis, $G(x,y,z,\sigma_x,\sigma_y,\sigma_z^d,\sigma_z^u)$. σ_z^d and σ_z^u are the widths below and above the excitation center height z_0, defined by the one σ $34th$ percentile. This means that the constructed excitation blob can be asymmetric along the z-axis ($\sigma_z^d \neq \sigma_z^u$). The width ($[-\sigma_z^d, \sigma_z^u]$) will still contain 68 per cent of the excitation, 34 percent below and 34 per cent above the excitation center z_0. It is necessary to separate σ_z^d and σ_z^u since the excitation width might be dependent on the neutral density gradient. ϕ will determine the horizontal rotation of the excitation, as in equation 5.3. The equation for the Free Parameter Search excitation function is given by:

$$f^F(x,y,z) = I_0 \cdot exp\bigg(-\bigg(\frac{((x-x_0)cos(\phi)+(y-y_0)sin(\phi))^2}{2\sigma_x^2}$$
$$+ \frac{((y-y_0-(z-z_0)sin(\theta))cos(\phi)-(x-x_0)sin(\phi))^2}{2\sigma_y^2}$$
$$+ \frac{(z-z_0)^2}{2\sigma_z^2}\bigg)\bigg) \tag{5.4}$$

Where σ_z is defined by:

$$\sigma_z = \begin{cases} \sigma_z^d, & \text{if } z \leq z_0 \\ \sigma_z^u, & \text{otherwise} \end{cases} \tag{5.5}$$

The construction of the excitation volume is based on Gaussian functions, as suggested in section 4.5. The Gaussian functions are chosen since the electron acceleration is assumed to be induced within a small volume, the excitation midpoint (x_0, y_0, z_0). The chance of collision between accelerated electrons and neutral constituents is considered a random process and the scattering of the secondary[1] electrons is assumed to be isotropically distributed. The excitation of neutrals in the ionosphere is mainly produced by secondary electrons.[Gustavsson and Eliasson, 2008] Hence, the isotropically scattered electron flux will be the main source of emission. The secondary electron excitation distribution can therefore be assumed to have a Gaussian distribution along all lines crossing the excitation midpoint (x_0, y_0, z_0). The Gaussian distribution is therefore chosen to construct the excitation distribution along the x,y and z axis with origin in the excitation

---

[1]Secondary electrons represents all the scattered electrons produced by the HF electron acceleration. Secondary electrons can therefore also be the third, forth, fifth, ... order scattered electrons with enough energy to excite ionospheric constituents.

midpoint. The width of the excitation distribution will depend on the mean free path of the electrons. The width of the 6300 Å emission will also depend on the wind, diffusion and lifetime of the long-lived $O(^1D)$ excited state. Note that the distribution remains Gaussian although the mean free path of the electrons and the $O(^1D)$ states are different up and down in the ionosphere, due to the neutral density gradient. The neutral density gradient will however turn the symmetric Gaussian excitation distribution into a skewed Gaussian distribution.

5.3   Modelling The Aurora

The parameters needed to construct the modelled aurora, depending on the construction method, are summarized in the table below.

Parameter	Theoretical	Semi-Theoretical	Free Search
Maximum intensity	I	I	I
Exciation Midpoint	x_0, y_0, z_0	x_0, y_0, z_0	x_0, y_0, z_0
Exciation radius/size	σ_r	σ_x, σ_y	$\sigma_x, \sigma_y, \sigma_z^d, \sigma_z^u$
Rotation angle		ϕ	ϕ
Shape Parameter		γ	
(Neutral Wind)	(V_x, V_y, V_z)	(V_x, V_y, V_z)	(V_x, V_y, V_z)
(Diffusion)	(D)	(D)	(D)
Number of parameters	5 / (9)	8 / (12)	9 / (13)

Table 5.1: The table shows the free parameters used to construct the 4278 Å, 5577 Å, 6300 Å and 8446 Å emission volumes. For the 4278 Å, 5577 Å and 8446 Å emissions, caused by relaxation of the short-lived excited $N_2^+ 1NG$, $O(^1S)$ and $O(^3P)$ states, it is assumed that the emission rate is directly proportional to the excitation rate. This means that it is assumed that these molecules/atoms will emit photons immediately after excitation, and there is no loss of emission due to collisional de-excitation. In addition, the instant de-excitation allows ignoring the drift of the excited states due to neutral wind and diffusion, as explained in chapter 4. However, extra parameters are needed to construct the 6300 Å emission volume. The drift and diffusion of the long-lived $O(^1D)$ excited state can not be neglected, independent of the construction technique. The construction of the 6300 Å emission volumes therefore needs three additional drift parameters and one diffusion parameter. The three wind parameters (V_x, V_y, V_z), the diffusion parameter (D) and the total parameter numbers of the 6300 Å emission are shown in table above in parenthesis.

For the 4278 Å, 5577 Å and 8446 Å modelling, it is only necessary to construct emission volumes at times matching the times of the observed images. This is possible since the constructed emission volumes will be independent of previously made emission volumes. The emission volumes are independent since the 4278 Å, 5577 Å and 8446 Å emissions are assumed to come from instantly emitting excited states, i.e. the emission is directly proportional to the excitation. Thus, all the excited states at the time of the previously observed image are assumed to be de-excited at the time of the present image. Hence, all the excited states from the previously modelled emission volume will be de-excited when modelling the present emission volume. In other words, the background

volume, before the present emission modelling, is empty.

However, for the the slowly decaying 6300 Å emission it is not as easy. The 6300 Å emission can not entirely be built up from the emission caused by de-excitation of the current excitation volume. It can not be assumed that all the long-lived $O(^1D)$ excited states will be de-excited during the period of the image exposure. It is therefore necessary to give the 6300 Å emission volumes "memories". This means that a theoretically estimated number of left-over excited $O(^1D)$ states, from the previous emission volume, will remain in the present emission volume. In other words, the background volume is not empty, an emission "memory", or residual, remains in the volume.

The simulation of the volume emission with the added residual is in practice achieved by recursion. The recursion will happen every five seconds ($dt = 5$ seconds), regardless of whether or not the constructed emission volume matches observed images in time. A shorter time step, dt, will improve the residual emission estimation, but slow down the parameter search. The proportion of the 6300 Å emission which is directly related to the current excitation volume will be referred to as $dE_n(x, y, z)$. The previously made emission volume, $E_{n-1}(x, y, z)$, will be processed by a set of nested functions, represented by F. F is accounting for the $O(^1D)$ effective lifetime, the wind and the diffusion over a simulated period of dt. The total current emission volume is then given by:

$$E_n(x, y, z) = F\Big(E_{n-1}(x, y, z)\Big) + dE_n(x, y, z) \tag{5.6}$$

$F\Big(E_{n-1}(x, y, z)\Big)$ symbolizes the residual emission volume. Equation 5.6 defines the recursive process. The current emission volume, $E_n(x, y, z)$, will become $E_{n-1}(x, y, z)$ after projection and comparisons with possible observational images. Since the images are taken at fastest every 10 seconds, and $dt = 5$ seconds, it is ensured that it always will be a matching emission volume to an observed image. How F (the effects of lifetime, wind and diffusion) is accounted for is described below:

- The lifetime of $O(^1D)$ is accounted for by multiplying the emission volume $E_{n-1}(x, y, z)$ from time t_{n-1} with a height and time dependent lifetime factor, $C_z(z, dt)$:

$$E_{n-1}^L(x, y, z) = C_z(z, dt) \cdot E_{n-1}(x, y, z) \tag{5.7}$$

  Where

$$C_z(z, dt) = exp\Big(-\frac{(t_n - t_{n-1})}{\tau(z)}\Big) \tag{5.8}$$

  $\tau(z)$ is the height dependent effective lifetime of $O(^1D)$ in the ionosphere. Theoretical estimates of the effective lifetime are used, as presented in figure 4.2. $\tau(z)$ is therefore not a search parameter.

- The drift of $O(^1D)$ from wind will thereafter be accounted for by moving the $E_{n-1}^L(x, y, z)$ emission midpoint according to the time step (dt) and the wind parameters (V_x, V_y, V_z): $[dx, dy, dz] = dt \cdot [V_x, V_y, V_z]$. The Volume emission shift is then given by

$$E_{n-1}^{LV}(x, y, z) = E_{n-1}^{L}(x - dx, y - dy, z - dz) \tag{5.9}$$

It is assumed that the wind is constant during dt and equal everywhere within the simulated volume.

- The $O(^1D)$ diffusion is then accounted for by convolution of the emission volume and a diffusion volume, defined by the search parameter D and the time step dt:

$$E_{n-1}^{LVD}(x, y, z) = (E_{n-1}^{LV}(x, y, z) * D(x, y, z))dt \tag{5.10}$$

In equation 5.6 above, the nested function $F\Big(E_{n-1}(x, y, z)\Big)$ is therefore given by:

$$F\Big(E_{n-1}(x, y, z)\Big) = E_{n-1}^{LVD}(x, y, z) = E_{n-1}^{LVD}\left(E_{n-1}^{LV}\left(E_{n-1}^{V}\big(E_{n-1}(x, y, z)\big)\right)\right) \tag{5.11}$$

The figure below illustrates equation 5.6:
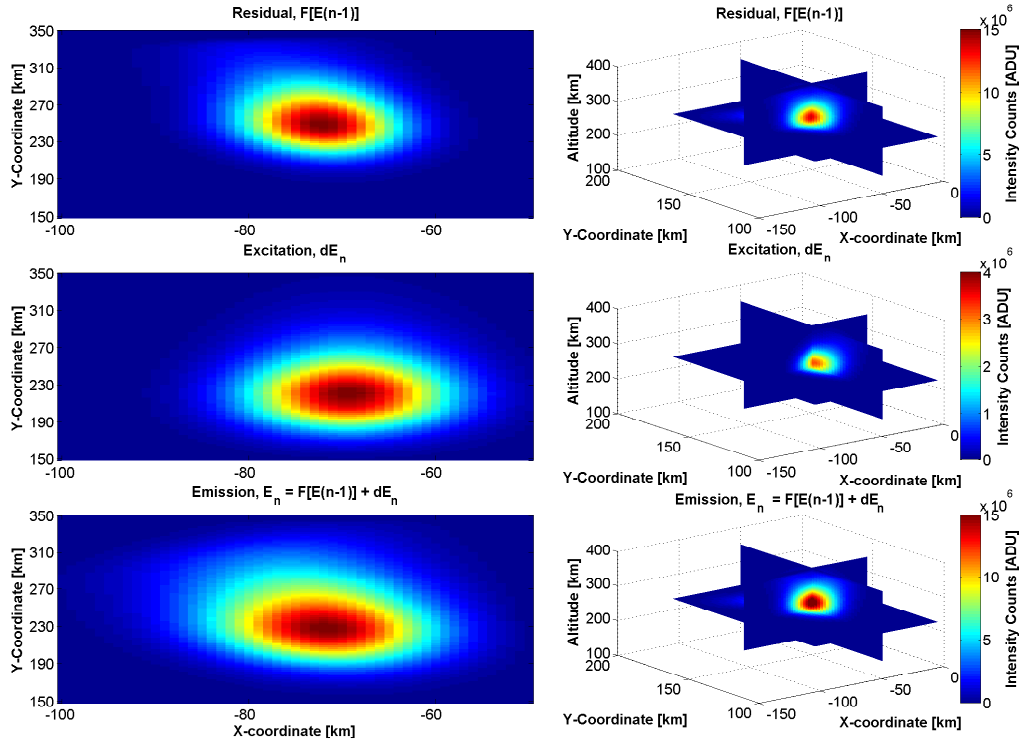
Figure 5.1: The residual emission $F\Big(E_{n-1}(x, y, z)\Big)$ is shown at the top. The emission from the current excitation during the time step $dE_n(x, y, z)$ is shown in the middle. At the bottom, the added emissions, the total current emission volume $E_n(x, y, z)$. The column to the left shows a cut through the emission volume. The figures in the right column shows slice plots of the emission volumes. Note that the count scales are different, as shown in the colour-bars. Most of the emission comes from the residual emission.

How the 3D emission volumes, seen in figure 7.1 are built up within the modelling volume will be described in the next chapter.

The Modelled Volume And The Projection Process

The techniques for modelling the aurora was described in the previous chapter. However, the properties of the modelling volume and the image projection of the modelled aurora have not been studied yet. Section 6.1 will describe how the modelled 3D emission distribution values will be assigned to emission volume elements, resulting in a volume emission distribution as shown below:
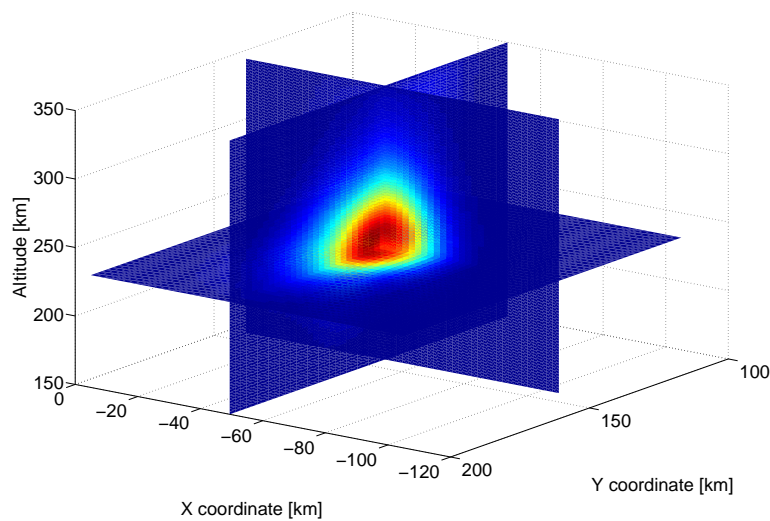
Figure 6.1: The figure shows a slice plot of a constructed emission volume. Section 6.1 will explain how the emission volume is built up within the modelling volume from a set of emission values.

In addition, the projection process will be explained in section 6.2.

6.1 Building The Emission Volume - Voxels And Blobs

An approximate solution to the tomographic inversion problem, with a limited amount of image projections, was proposed by [Gordon et al., 1970]. Gordon et al. suggested to use voxels [1] to build up the object's 3D emission distribution.

The method used in this thesis is based on the method proposed in [Rydesäter and Gustavsson, 2000]. The applied method uses the idea of voxels to construct the volume emission, but the voxels are exchanged in favour of overlapping three dimensional cos^2 blobs. The cos^2 function define the blob (b_i) in all directions $(b_i = cos^2(dx_i)cos^2(dy_i)cos^2(dz_i))$, making the blobs close to being spherical with a midpoint value of 1. The blobs are overlapping by joint domains, defined by $(dx, dy, dz \in [-\frac{\pi}{4}, \frac{\pi}{4}])$ within the host volume element b_i and $(dx, dy, dz \in [-\frac{\pi}{2}, -\frac{\pi}{4}) \cup (\frac{\pi}{4}, \frac{\pi}{2}])$ in the neighbouring volume elements. These blobs are equal in size, have a uniform emission value and are completely space filling, just like the voxels. A comparison between the voxels and the blobs is shown in the figure below:
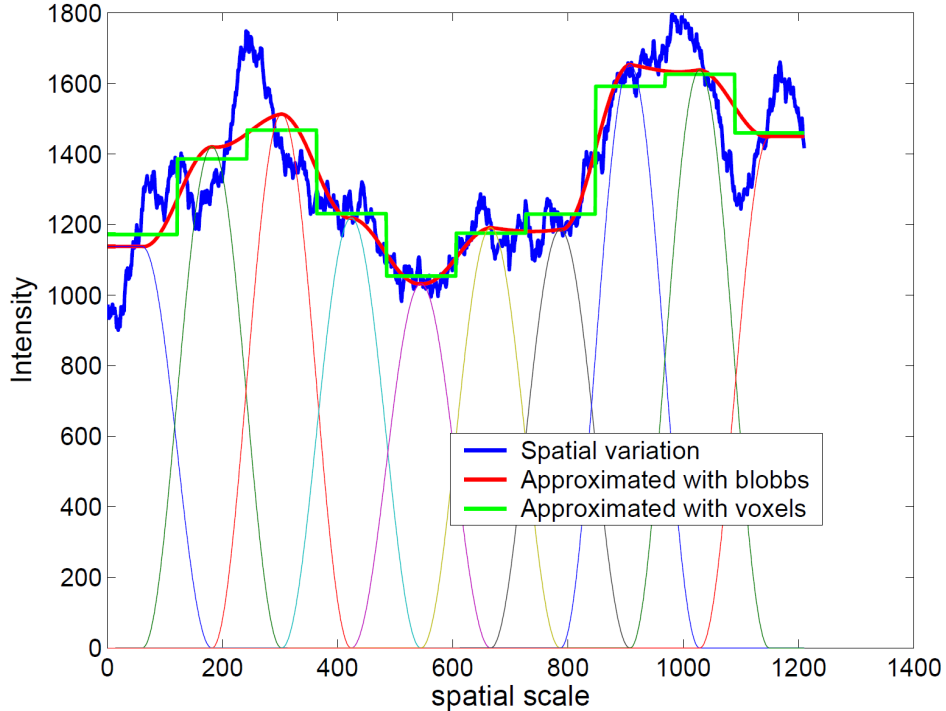
Figure 6.2: The figure shows the difference between voxels and blobs in the transition smoothness. In this figure only 10 voxels/blobs are used to fit the one dimensional function. (51 x 51 x 101) blobs will be used to construct the 3D auroral distribution.

The overlapping blobs are superior to the voxels since they are better at approximating smoothly varying functions, as shown in the figure 7.1 above. The modelled emission volumes will therefore be built up using the cos^2 blobs. The value of each emission blob is calculated from the equations 5.2, 5.3 and 5.4 in chapter 5. For the 6300 Å modelling,

---

[1]Voxels are volume elements, small cubes, with a uniform emission value.

equation 5.6 is needed as well. A volume of (102 x 102 x 202) km^3 was chosen to contain the aurora. The size of each volume element containing a blob is (2 x 2 x 2) km^3. Hence, (51 x 51 x 101) blob values are calculated for each volume construction.

6.2   The Projection Process

It is possible to calculate the projection from the 3D emission blobs down to the 2D images. However, to calculate the projection from every blob distribution in the (51 x 51 x 101) blob grid would require a considerable amount of computing. The more time efficient Dot-Projection Algorithm, introduced in [Rydesäter and Gustavsson, 2000], is therefore used. The description given here is only a short review of the projection technique described in citerydesater2000investigation. The projection algorithm from the emission volume down to a simulated image at a given imaging station is step-by-step below:

1. The midpoint, the dot, of each blob is projected down to a simulated image

2. The dots are divided into projection layers, defined by their radial distance to the imaging station, $\boldsymbol{r}_s$. This is shown to the left in figure 6.3. In this thesis, the dots were divided into Six layers. A larger number of layers would improve the modelled image but slow down the projection process.

3. The uniform emission value of every blob is divided by $(\boldsymbol{r}_s^2)$, assuming an isotropic emission distribution

4. The emission contribution from the dots is then assigned to their respective projection layers, as described to the right in figure 6.3.

5. Each layer is filtered with a cos^2 2D filter. The 2D filters are separately designed for each layer so that the dots will reproduce (approximately) the projected cos^2 blob footprint after filtering. How these filters are generated is described in [Rydesäter and Gustavsson, 2000]. The filtering process is visualized to the right in figure 6.3. Here the dot projections are filtered first in the vertical direction and then in the horizontal direction.

6. The filtered projections layers are added to form the completed simulation image. The layers further away from the imaging station will project smaller and fainter cos^2 blob footprint than the layers closer to imaging station. This can be seen in the "Add Layers" image at the bottom and to the right in figure 6.3.
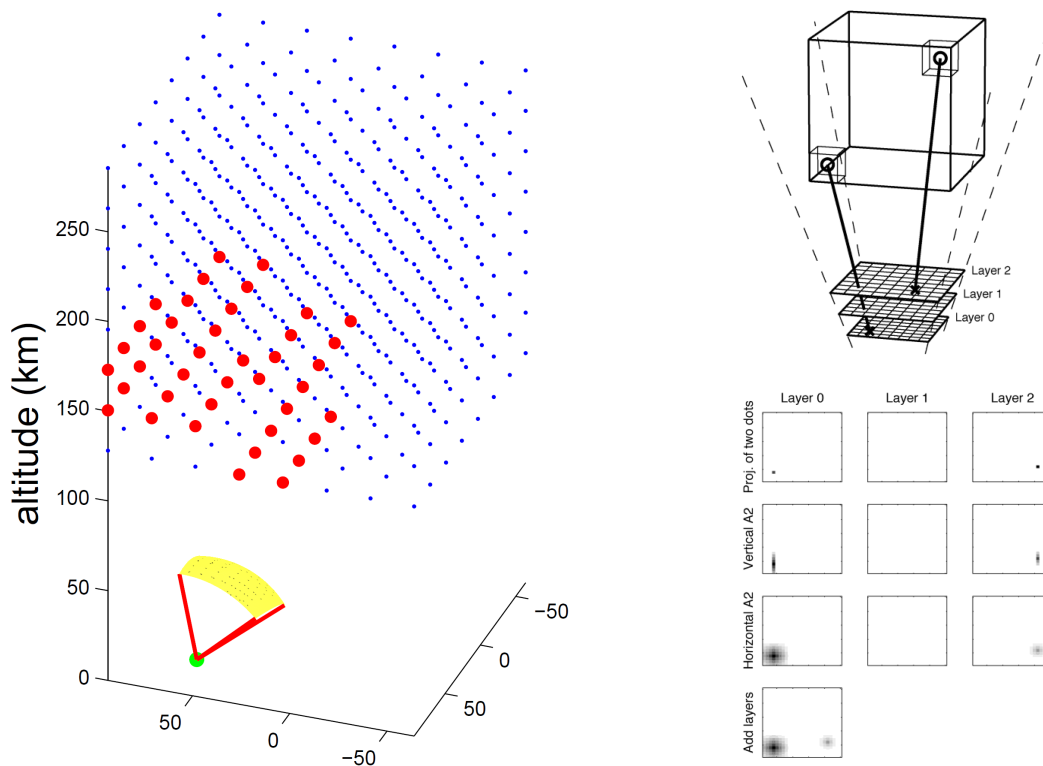
Figure 6.3: The figure to the left shows the emission dot grid. The red dots represents dots that are belonging to the same projection layer, as seen from the given imaging station. The figure to the right shows the projection process, from the dot-layer assignment to the final image. The rightmost figure is taken from (Rydesäter, 2000)[Rydesäter and Gustavsson, 2000]

Projection can only be done if the pixel field-of-view is known. Star calibration is used to to estimate the field-of-view of every pixel in the CCD. The field-of-view of the pixels containing stars can be estimated since the the position of the bright stars and their inherent orientation and angular difference is known with high accuracy on the night sky. The (256 x 256 pixels) transformation matrix and hence the field-of-view of the entire CCD is estimated by interpolating in between the transformation points determined by the star-pixels. It is beyond the scope of this thesis to give a thorough description of the projection and star calibration processes. The projection and the star calibration methods are only applied in this thesis and not developed further. The projection and star calibration programs, used in this thesis, are a part of Auroral Image Data Analysis (AIDA) tools, provided by B. Gustavsson. The contribution of this thesis lies in how the simulated emission distribution is built up, analysis of its appearance and evaluations of the construction parameters.

The volume and the volume projection, down to the imaging stations, is shown in the figure below.

42

Projections Of The Simulation Volume
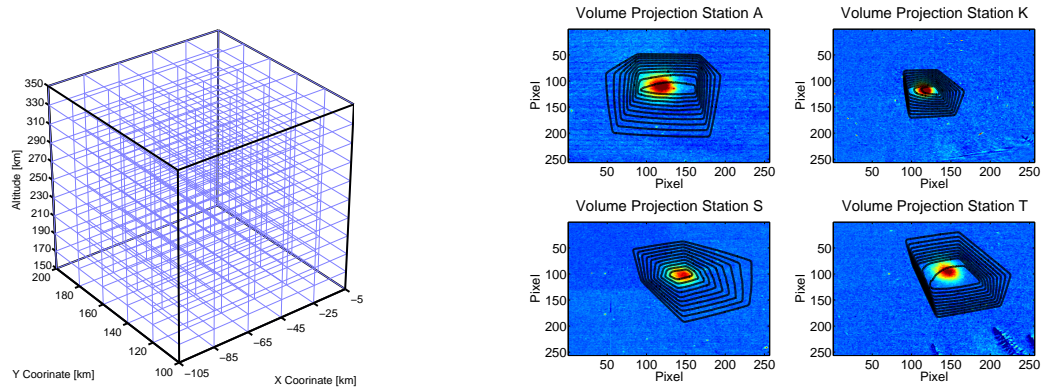
Figure 6.4: The figure to the left show the grid plot of the volume where the artificial aurora will be modelled. The size of each volume in the grid plot is (20 x 20 x 20) km^3, while the volume containing the overlapping blobs has a size of (2 x 2 x 2) km^3. A finer grid will improve the acquired data but slow down the simulation speed considerably. To the right is the contour plot of the projected emission volume on top of images containing radio induced airglow, the airglow is placed well within the volume at all stations.

Analysis Of The Modelled Aurora

7.1   Comparing The Observed And Modelled Images

Finally, now that the aurora construction, modelling and projection is defined, it is possible obtain the modelled images. Comparisons of the "real" aurora projections (the observational images) and the "simulated" aurora projections (the modelled images), will reveal the reliabiltiy of the parameter guess. The parameter guess is then changed according to the parameter search method and the error function value of a modified version of the least square fitting method. The parameter search is done using the Nelder-Mead simplex search method. It is beyond the scope of this thesis to describe the search algorithm, the curious reader is directed to [Lagarias et al., 1998]. After the parameters are changed and the cos^2 blob values constructing the modelled aurora are modified, another comparison is done. The (parameter search $\rightarrow$ emission construction $\rightarrow$ image comparison) process is then iterated.
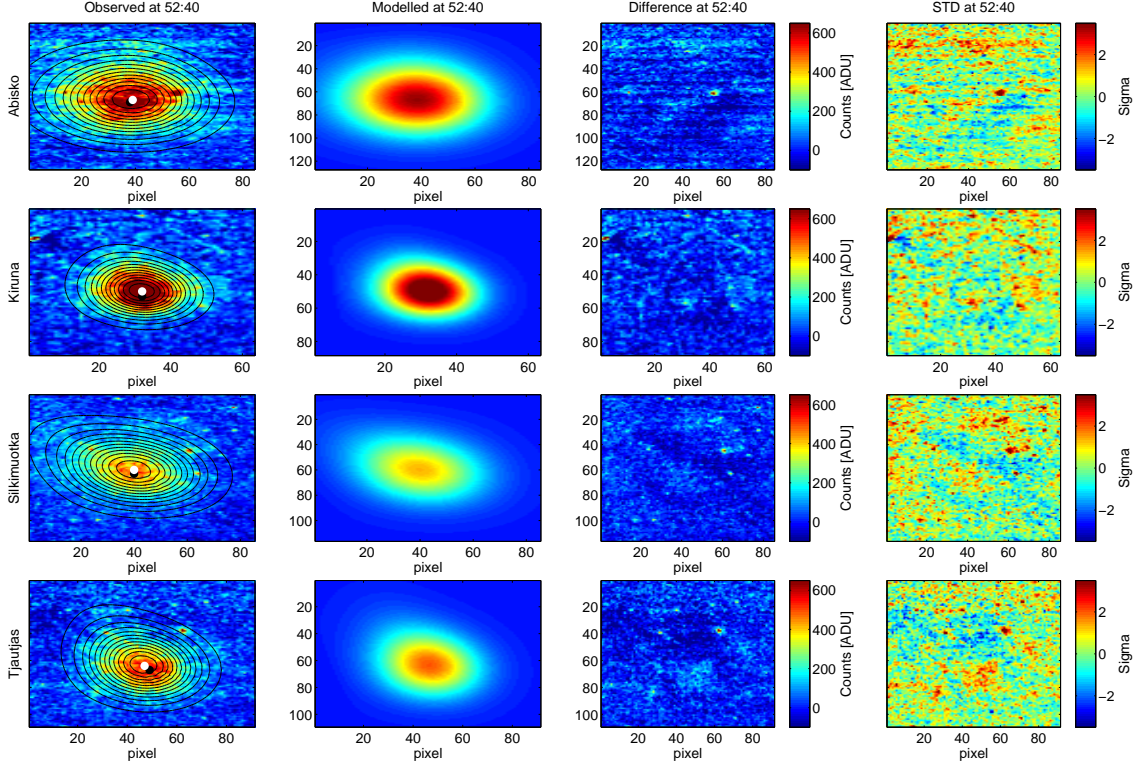
Figure 7.1: The figure shows a comparison in 6300 Å emission at time 16.52.40 UT between the observed image in the leftmost column and the modelled image in column two. The modelled images are made using the semi-theoretical construction technique. The white dot in the middle of the emission blob in the observed image is the modelled emission maximum emission point ($\tilde{m}_s$). The black dot represents the point of maximum emission in the observed image (m_s). The black contour lines on top of the observed emission blob represents the shape of the modelled emission. The difference between the observed image and the modelled image ($p_s - \tilde{p}_s$) is shown in the third column. The standard deviation of the intensity difference distribution is shown in the rightmost column. The top row is the comparison for the Abisko station, the second row is from the station in Kiruna, the third row is the Silkimuotka station and the last row is the Tjautjas station.

By looking at which comparison that gives the best result, it is possible to direct the parameter guesses iterations to a converging "best fit" guess. This is in practice done by minimizing the least-square error function. In this thesis, a modified version of the least-square error function is applied. The modified version also takes the spatial distance between the point of maximum intensity in the observational and simulated images into consideration.

$$E(\bar{V}_i) = \frac{1}{|s|} \cdot \left(\sum_{s,i,j} [p_s(i,j) - \tilde{p}_s(i,j,I(\bar{r},\bar{V}_i))]^2 + W \cdot \sum_s [\boldsymbol{m_s} - \boldsymbol{\tilde{m}_s}]^2 \right) \qquad (7.1)$$

$E(\bar{V}_i)$ is the error function of the of the guessed parameters $\bar{V}_i$ at time t_i. $|s|$ is the total number of stations, four in ALIS. s is is the station index, 1, 2, 3 and 4 for the stations in Abisko, Kiruna, Silkimuotka and Tjautjas. (i,j) is the pixel index. $p_s(i,j)$

is the observed image in station s after background reduction and $\tilde{p}_s(i, j, I(\bar{r}, \bar{V}_i))$ is the modelled image for station s. $\tilde{p}_s$ is made out of projections of the simulated aurora and is therefore also directly dependent on $I(\bar{r}, \bar{V}_i)$ which is the modelled volume emission distribution at time t_i.[Gustavsson et al., 2001] $\boldsymbol{m_s}$ is the vector from pixel $(1, 1)$ to the location of the maximum intensity of the induced aurora in the observed image. $\tilde{\boldsymbol{m}}_s$ is the vector to the location of the maximum intensity in the simulated image. W is a weight factor controlling the significance of the positional maximum intensity differences.

7.2 Statistic Analysis Of The Modelled Aurora

Simulated airglow blobs are continuously being constructed using parameter guesses as provided by the parameter search and tested by the least-square error function (equation 7.1) for as long as desired. The reliability of the parameters is then determined by the reduced Pearson's chi-squared number, see equation 7.2. The reduced Pearson's chi-squared number can not be used to support or falsify the model, but is chosen to quantify the credibility of the model. The closer the number is to 1, the better the model is. $(\chi^2_{red} >> 1)$ indicates a poor fit. $(\chi^2_{red} < 1)$ indicates "over-fitting", this happens if the variance $(\sigma^2 = E_s)$ is overestimated or if the model somehow is fitting noise.

$$\chi^2_{red} = \frac{1}{|s|} \cdot \frac{1}{N - n} \cdot \sum_s \sum_{i,j} \frac{(O_s(i, j) - E_s(i, j))^2}{E_s(i, j)} \tag{7.2}$$

N Is the total number of pixels within the region of interest (the heating area), i.e. the total number of data points to be considered and n is the degrees of freedom, the number of fitted parameters. O is the observed "raw" image, before background subtraction, and E is the expected modelled image with the background added. The other parameters are defined as previously. It is possible to use the reduced Pearson's chi-squared number since both the background count distribution and de-excitation emission distribution can be considered as random processes and the emitted radiation can safely be assumed to be isotropic and independent of each other. The number of photons emitted from a volume containing a number of excited atoms, during the 6 second exposures, will therefore be Poisson distributed. The pixel gain due to the background airglow, assuming no cosmic rays or other irregularities in the background counts, will also have a Poisson distribution. The gain in each pixel will therefore be the sum of the two emission contributions. The sum of two Poisson distributions will be yet another Poisson distribution. The discrete Poisson distribution will approach the continuous normal distribution with enough pixel counts, (counts > 50), the average raw counts in the images are approximately 4000. Hence, the intensity in every pixel in the modelled image will have an expected probability distribution: $p(E(i, j)) = N(O(i, j), \sqrt{O(i, j)})$.

$$\chi^2_{red} = \frac{1}{|s|} \cdot \frac{1}{N - n} \cdot \sum_s \sum_{i,j} \frac{(p_s(i, j) - \tilde{p}_s(i, j))^2}{E_s(i, j)} \tag{7.3}$$

The squared difference $(p_s(i, j) - \tilde{p}(i, j))^2$ can be used instead of $(O_s(i, j) - E_s(i, j))^2$, since the squared differences will be equal, with or without the background. The reduced

Pearson's chi-squared number, as given in equation 7.3, can therefore be used to compare the parameter guesses and construction methods.

The comparison between the modelled and the observational images, described in section 7.1, and the reduced Pearson's chi-squared number will be used in the following chapter, where the three construction techniques will be examined.

Simulation Results And Analysis

The results and analysis of the 6300 Å, 5577 Å and 8446 Å emission modelling will be presented in this chapter. The radio induced emission in the 4278 Å line was too weak for tomographic reconstruction. In addition, the 8446 Å emission reconstruction could only be done for one set of images. The emission profiles of the modelled 6300 Å, 5577 Å and 8446 Å emissions will be given at the end of this chapter.

8.1   The 6300 Å Emission Results And Analysis

The 6300 Å auroral modelling results will be presented first. The 6300 Å emission is the strongest emission line, the emission enhancement is approximately 3 times stronger during heating at 6.200 MHz than during heating at 5.423 MHz, as shown in figure 4.1. The observed and modelled image comparison during 6.200 MHz heating, for all three construction techniques, are given below:
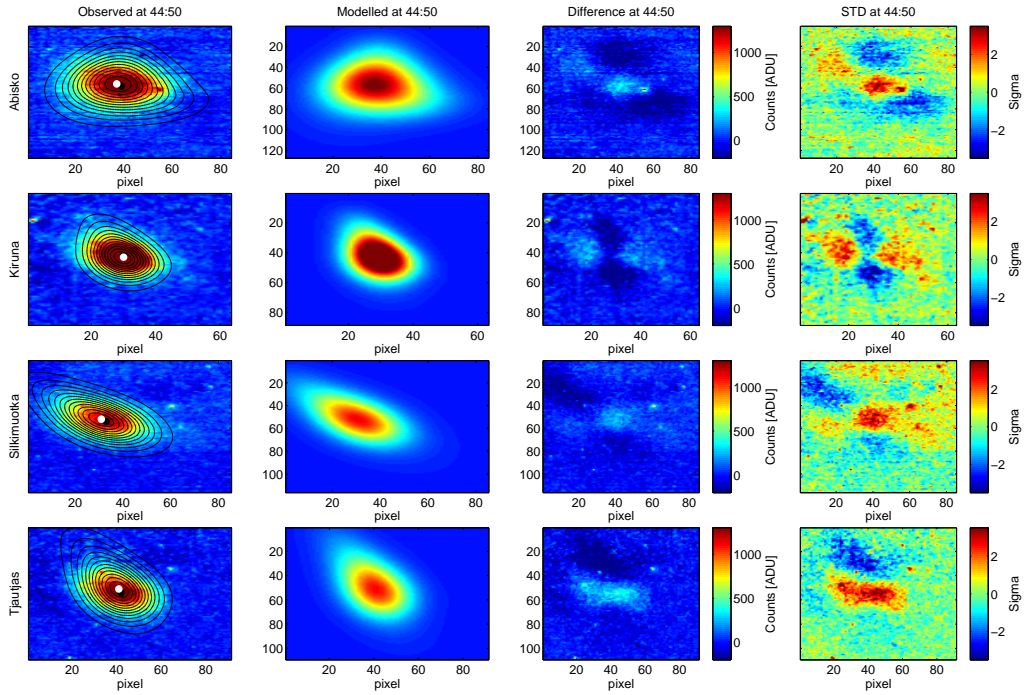
Figure 8.1: Simulation result using the theoretical curves construction technique during 6.200 MHz heating. An explanation of the images and what they represent was given in figure 7.1.
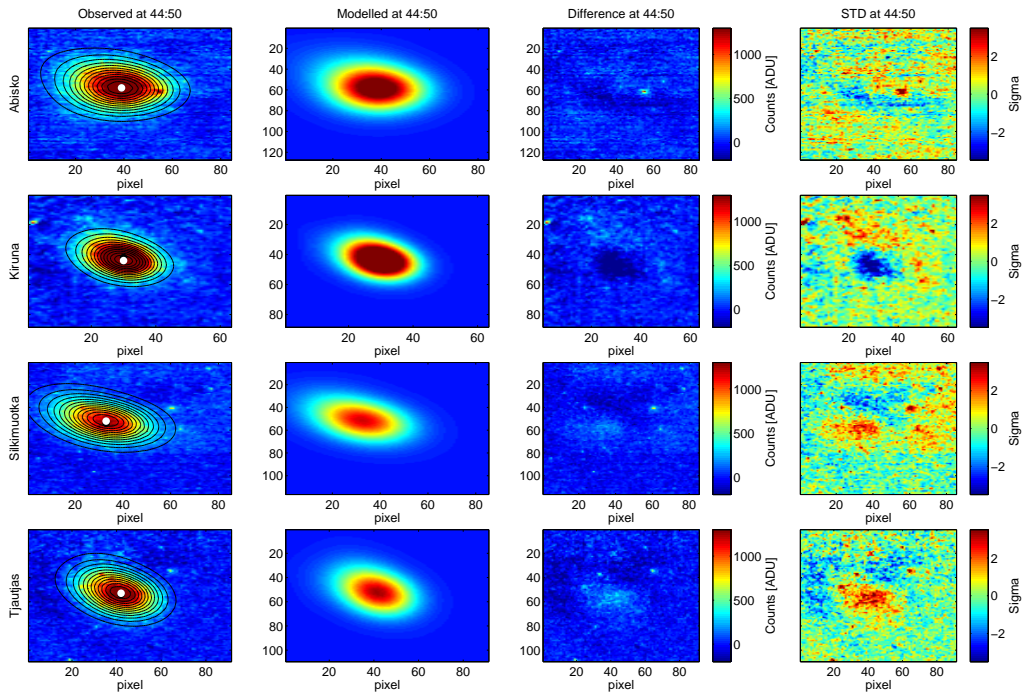
Figure 8.2: Modelling results using the semi-theoretical curves construction technique under 6.200 MHz heating
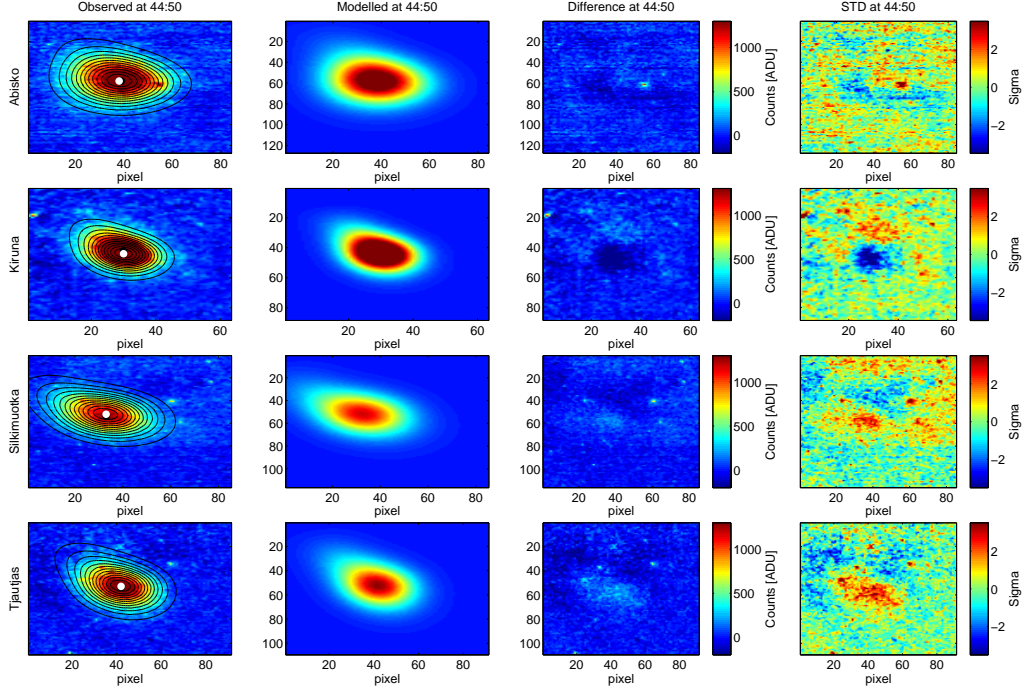
Figure 8.3: Modelling results using the free parameter search construction technique during 6.200 MHz heating

99 artificial auroras are modelled in the 6300 Å emission line, 33 for each construction technique. All comparison images can not be shown here. Note that additional comparison images are presented in appendix A. One of the comparisons presented in the appendix is a comparison from modelling at the emission enhancement minimum. This is done to have a measure of the modelling background, i.e. to find out how uniform the "difference" and standard deviation images are at minimum. Only two of the comparisons of the emission enhancements at maximum are shown in this section. One during 6.200 MHz heating, at time 16.44.50 UT shown above, and one during 5.423 MHz heating, at time 16.52.40. The times of the comparison images for all construction techniques are equal, this makes it easier to compare the different construction methods. The 6300 Å emission comparison images during 5.423 MHz heating are presented below:
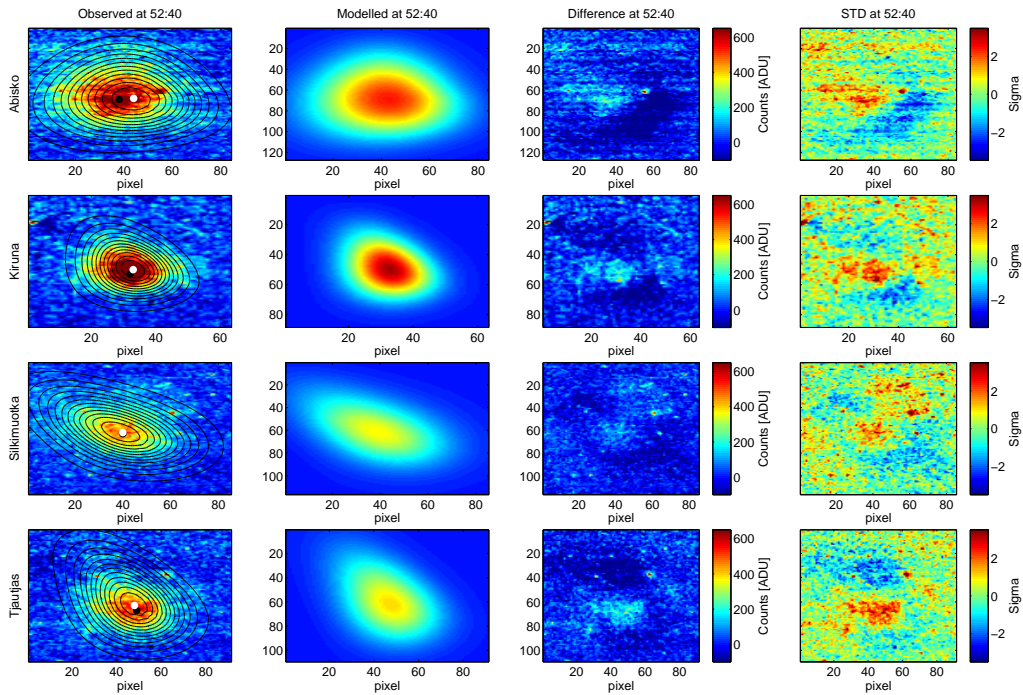
Figure 8.4: Modelling results using theoretical curves under 5.423 MHz heating. Note that the count value range, the colorbar range, in the 5.432 MHz comparison images is one half of the count value range in the 6.200 MHz images.
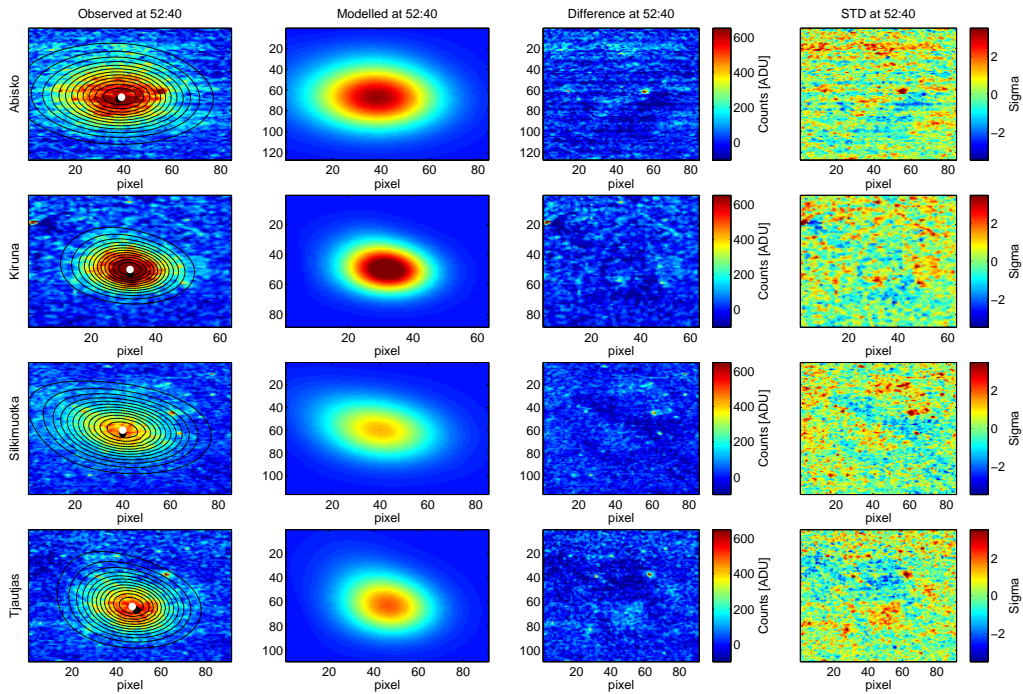
Figure 8.5: Modelling results using semi-theoretical curves under 5.423 MHz heating
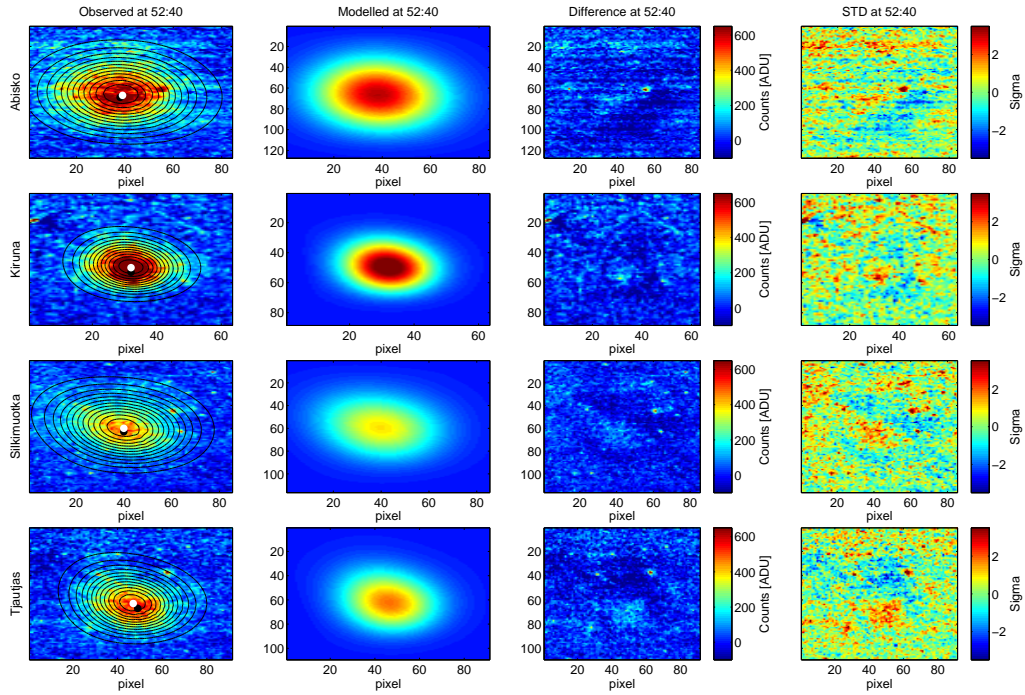
Figure 8.6: Modelling results using free parameter search under 5.423 MHz heating

It is apparent from the standard deviation images in the rightmost column that there are clusters of high absolute STD counts within the pixels of the radio induced emission blob. This is especially clear for the theoretical curve comparison image during 6.200 MHz heating, figure 8.1. To see this more clearly, histogram plots of the pixel values are shown in the figure below.
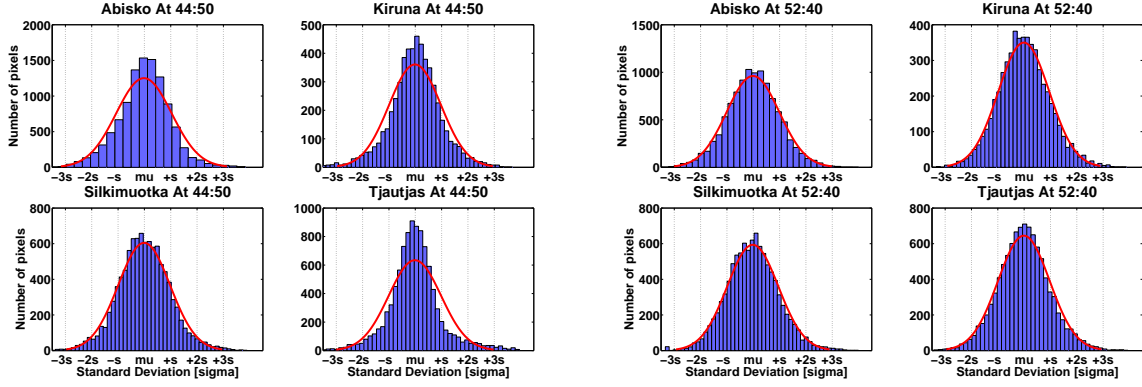
(a) Theoretical during 6.200 MHz (b) Theoretical during 5.423 MHz
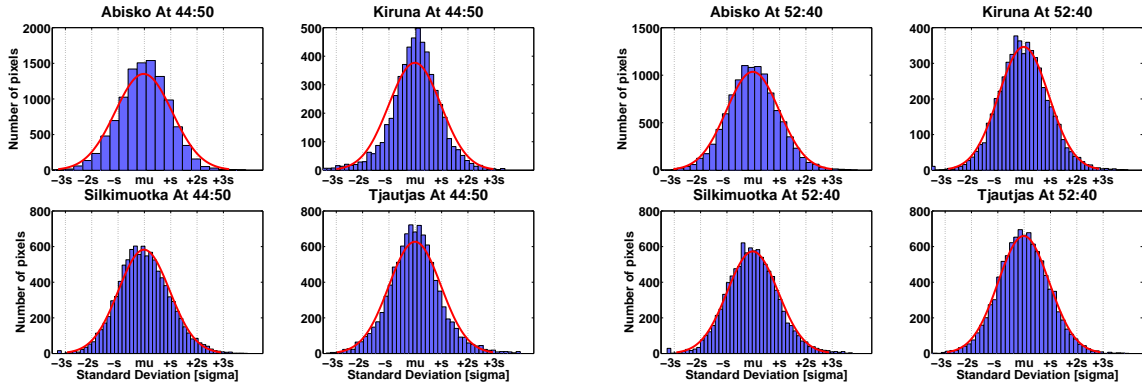
(c) Semi-theoretical during 6.200 MHz (d) Semi-theoretical during 5.423 MHz
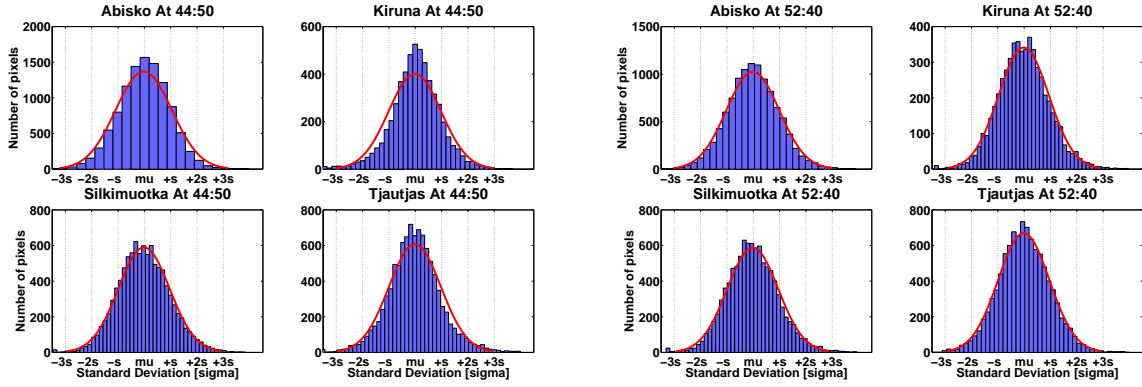
(e) Free parameter search during 6.200 MHz (f) Free parameter search during 5.423 MHz

Figure 8.7: Comparison between binned pixel values in the "difference" images from the modelled-observed comparison images, figures 8.1 - 8.6, and a fitted normal distribution. The number of pixels within a count interval are given by the purple posts and the red line represents the fitted normal distribution.

It is apparent, from figure 8.7 above, that the binned pixels and the normal distribution do not fit well for the theoretical curves construction method, especially during the 6.200 MHz heating. The fitted normal distribution underestimates the distribution within $\pm 1\sigma$ to better fit the high number of pixels with count values outside $\pm 1\sigma$. The

semi-theoretical curves and free parameter search methods provides better normal distribution fitting. Figure 8.7 show a better normal distribution fit during 5.423 MHz heating than during 6.200 MHz heating. However, the signal to noise ratio is lower during 5.423 MHz frequency heating, meaning that the "difference" count values, shown in column three in the comparison images, will be closer to the random and normally distributed background emission. Hence, although the 5.423 MHz fitting seems better, it is important to keep in mind that the signal to noise ratio will influence the quality control of the model. The signal to noise ratio difference will also influence the relative values of the reduced Pearson's chi-squared number (χ^2_{red}). χ^2_{red} will be overestimated for the 6.200 MHz heating and underestimated for the 5.423 MHz heating. The parameter results and analysis of the images taken under 6.200 MHz heating and images taken during 5.423 MHz heating will therefore be given separately, this will also be done in the result evaluation of the other emission lines. In addition, the transmitted frequency shift from 6.200 MHz to 5.423 MHz will cause a heating altitude fall, as explained in chapter 3. This increases the importance of separating the 6.200 MHz and 5.423 MHz analysis. The fall in heating altitude can be seen in the electron temperature figure 3.2 and the modelled 3D emission distributions in figure 8.8. It is however assumed that the heating altitude is constant during heating with constant frequency. This is a valid assumption, judging from the EISCAT electron temperature appearance in figure 3.2. Thus, the mean parameter values and their standard deviation can be estimated from the simulation outputs of all the images during constant heating frequency. The parameter results and the χ^2_{red} values are presented in the table below.

Parameter	6.200 MHz frequency heating			5.423 MHz MHz frequency heating		
$I(counts)\cdot 10^6$	4 ± 2	7 ± 3	6 ± 3	1.5 ± 0.5	3 ± 1	2 ± 1
$x(km)$	-45 ± 5	-54 ± 2	-53 ± 2	-45 ± 1	-54 ± 1	-48 ± 1
$y(km)$	143 ± 3	152 ± 2	151 ± 2	145 ± 2	159 ± 3	153 ± 1
$z(km)$	230 ± 2	241 ± 4	238 ± 4	206 ± 9	233 ± 6	228 ± 3
$\sigma_r(km)$	11 ± 3			16 ± 1		
$\sigma_x(km)$		12 ± 3	13 ± 3		15 ± 2	16 ± 1
$\sigma_y(km)$		10 ± 2	11 ± 2		15 ± 3	20 ± 2
$\sigma_z^d(km)$			16 ± 5			15 ± 3
$\sigma_z^u(km)$			12 ± 6			16 ± 5
γ		3.5 ± 1.1			2.2 ± 0.8	
$\phi(deg)$		7.5 ± 1.6	6.5 ± 1.5		10.2 ± 0.9	9.2 ± 0.7
$V_x(km/s)$	0.8 ± -0.5	-0.2 ± 0.5	-0.1 ± 0.6	1.7 ± 0.3	-1.2 ± 0.9	-0.1 ± 0.1
$V_y(km/s)$	-0.4 ± 0.3	0.2 ± 0.4	0.0 ± 0.4	-0.9 ± 0.2	0.4 ± 0.2	-0.2 ± 0.1
$V_z(km/s)$	0.5 ± 0.5	-0.1 ± 0.5	0.4 ± 0.4	1.0 ± 0.4	-2.1 ± 0.8	-0.5 ± 0.3
$D(km^2/s)$	0.4 ± 0.6	2 ± 2	0.2 ± 0.5	0.6 ± 0.4	15 ± 106	0.0 ± 0.0
χ_{red}^2	2.2 ± 0.6	1.4 ± 0.2	1.4 ± 0.2	1.8 ± 0.5	1.4 ± 0.3	1.5 ± 0.3
Model:	Theo	Semi	Free	Theo	Semi	Free

Table 8.1: The mean and standard deviation values of the modelling during the 6.200 MHz and 5.423 MHz frequency is shown above. The construction technique names are shortened to Theo, Semi and Free, this represents the theoretical curves, semi-theoretical curves and free parameter search construction techniques. These estimates were done during 22 images under 6.200 MHz heating and 11 images during 5.423 MHz heating. The parameter values are physically feasible, except the D value in the semi theoretical modelling during 5.423 MHz heating. At the end of the modelling, when only three stations were operating, the diffusion parameter started to stray away. The reason for this is unknown. It might be that the model attempted to fit noise outside the emission blob by increasing the diffusion. The diffusion had a value of over 200 (km^2/s) at the end, this is not physical and is not in agreement with the other emission reconstructions. The increasing diffusion did not effect the other parameters, which stayed within reasonable bounds.

The figure below shows the constructed emission volumes, at time 45:50 UT and 52:40 UT, using the three different construction techniques:
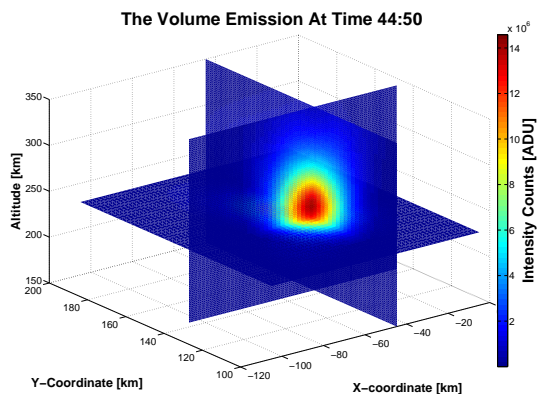
(a) Theoretical during 6.200 MHz
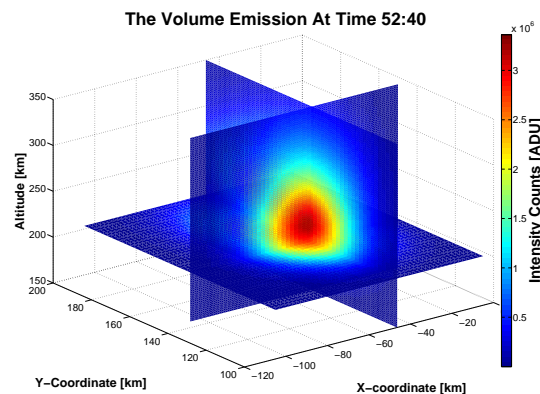
(b) Theoretical during 5.423 MHz
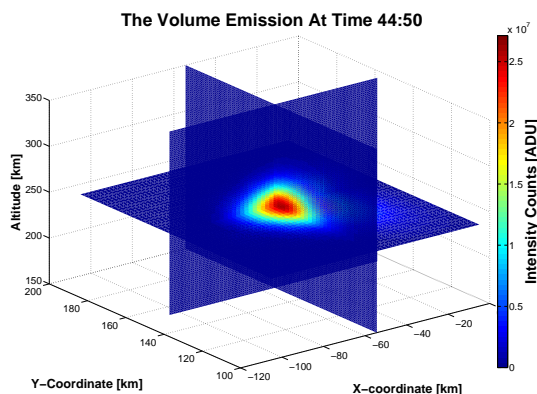
(c) Semi-theoretical during 6.200 MHz
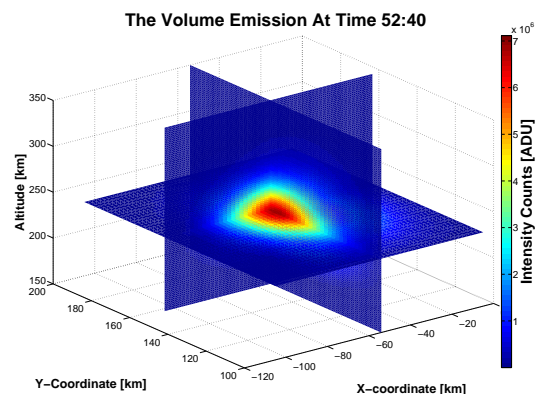
(d) Semi-theoretical during 5.423 MHz
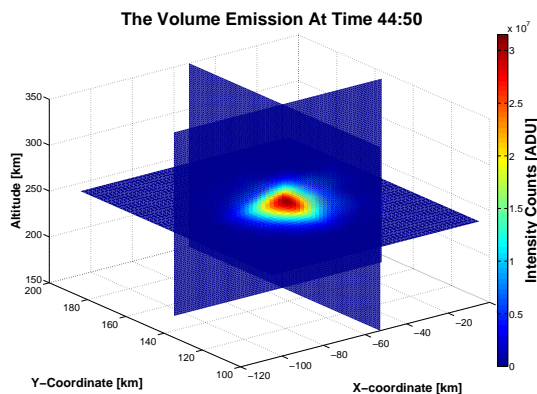
(e) Free search during 6.200 MHz
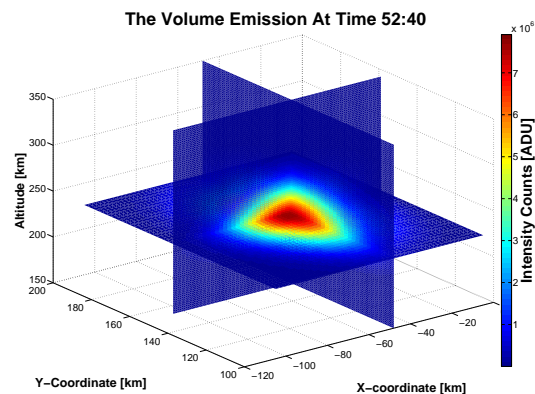
(f) Free search during 5.423 MHz

Figure 8.8: The constructed volumes which are projected down to the modelled images in the modelled-observed comparison images, figures 8.1 - 8.6. The slice is taken through (x_0, y_0, z_0), the point of maximum excitation rate.

8.2 The 5577 Å Emission Results And Analysis

The results from the 5577 Å auroral simulation will now be presented. The 5577 Å emission is the second strongest emission line. The emission enhancement is approximately 20 per cent stronger during the 5.423 MHz heating than during 6.200 MHz heating. The observed and modelled image comparisons for the 6.200 MHz heating are given below:
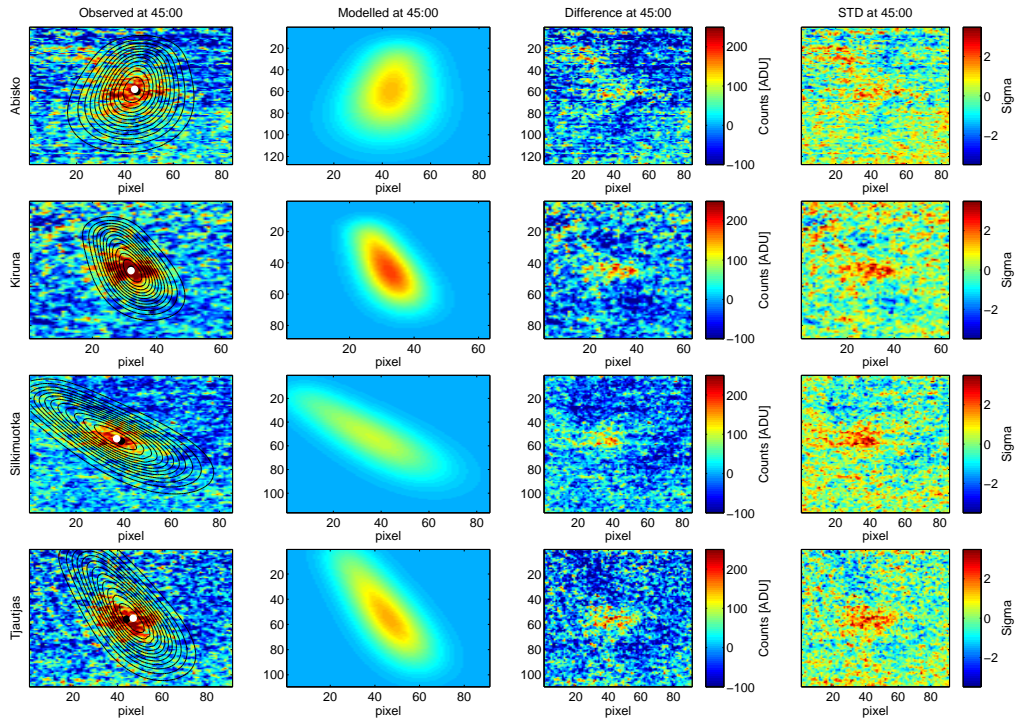
Figure 8.9: Simulation results using theoretical curves during 6.200 MHz heating
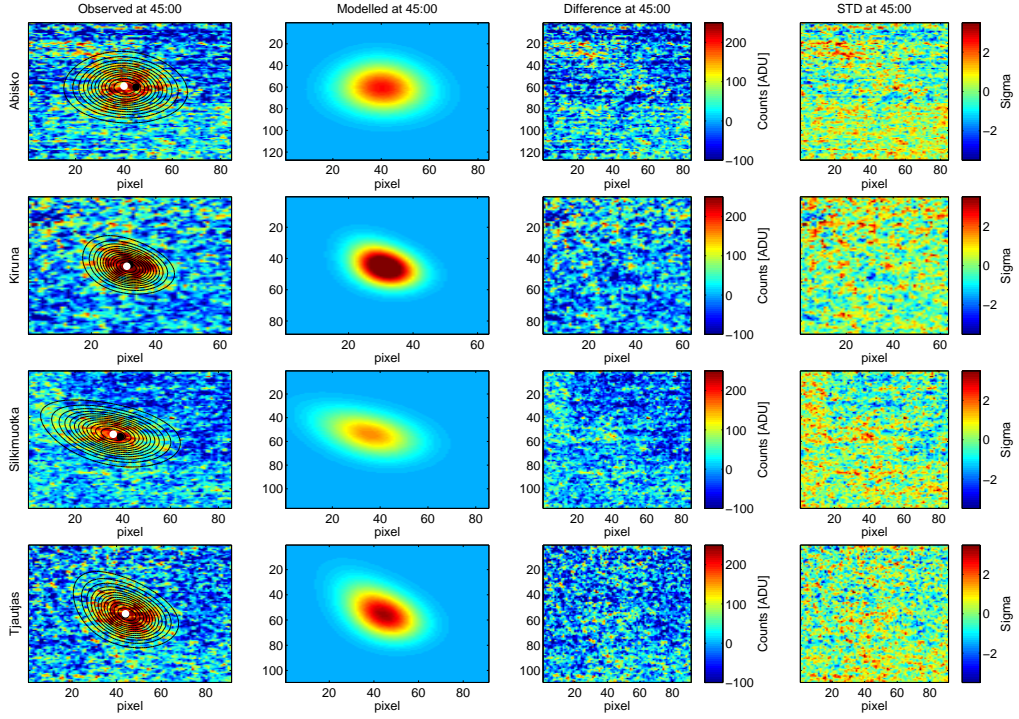
Figure 8.10: Simulation results using semi-theoretical curves under 6.200 MHz heating
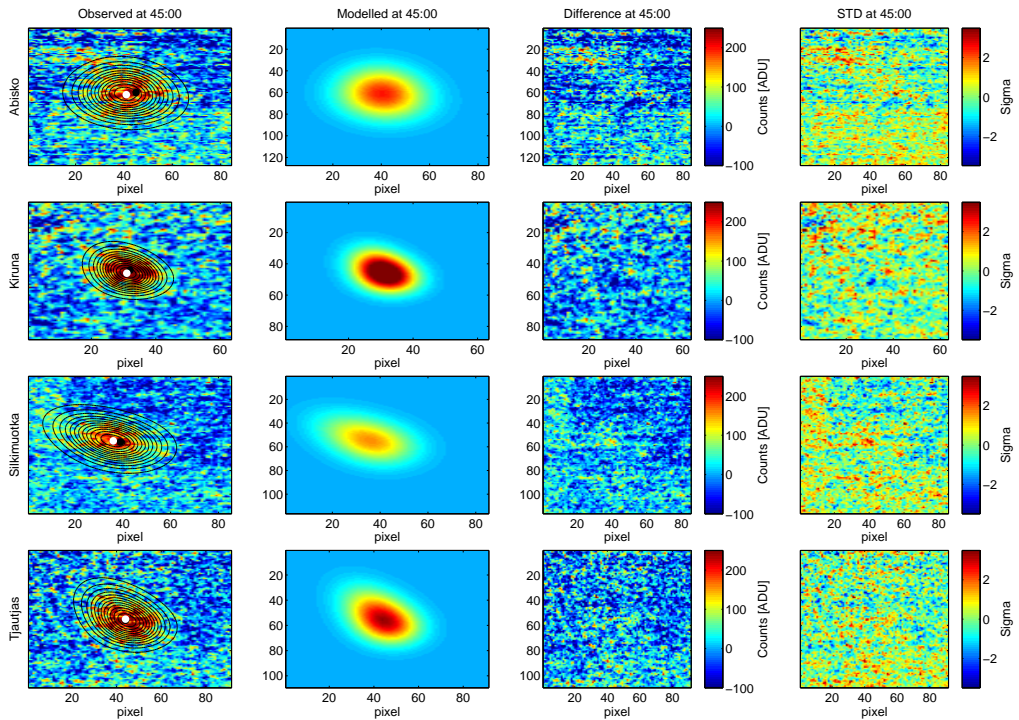
Figure 8.11: Simulation results using free parameter search during 6.200 MHz heating

39 artificial auroras are modelled in the 5577 Å emission line, 13 for each construction technique. Note that additional comparison images are presented in appendix A. Two

comparisons with times similar to the 6300 Å comparison times are shown in this section. One during 6.200 MHz heating, at time 16.45.00 shown above, and one during 5.423 MHz heating, at time 16.51.40. The 5577 Å emission comparison images during 5.423 MHz heating are presented below:
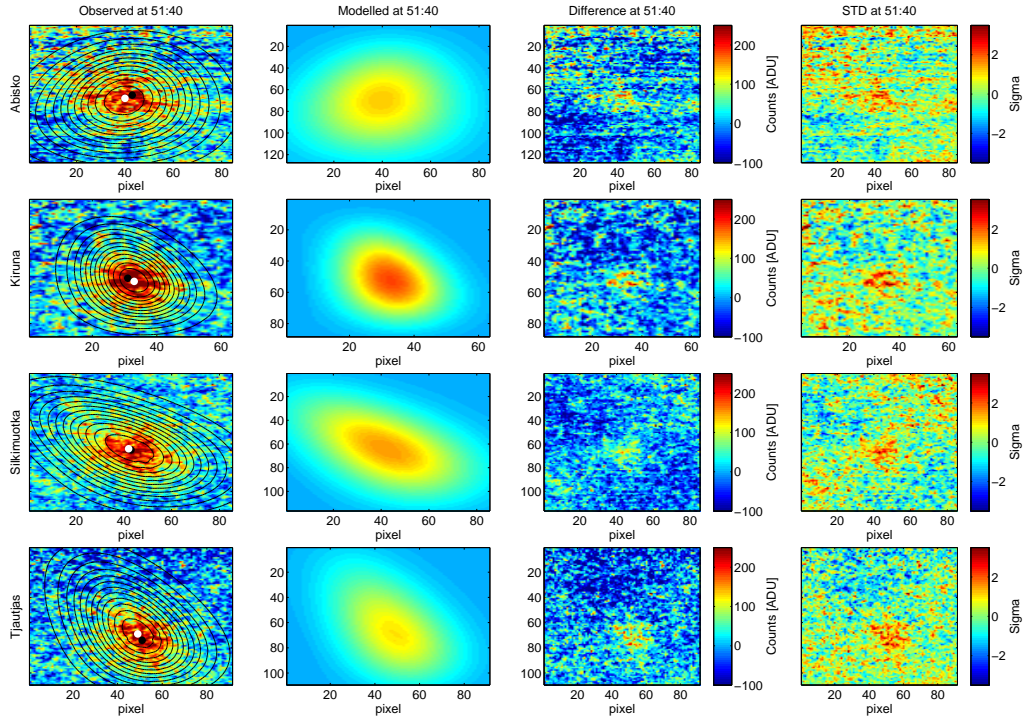
Figure 8.12: Simulation results using theoretical curves during 5.423 MHz heating
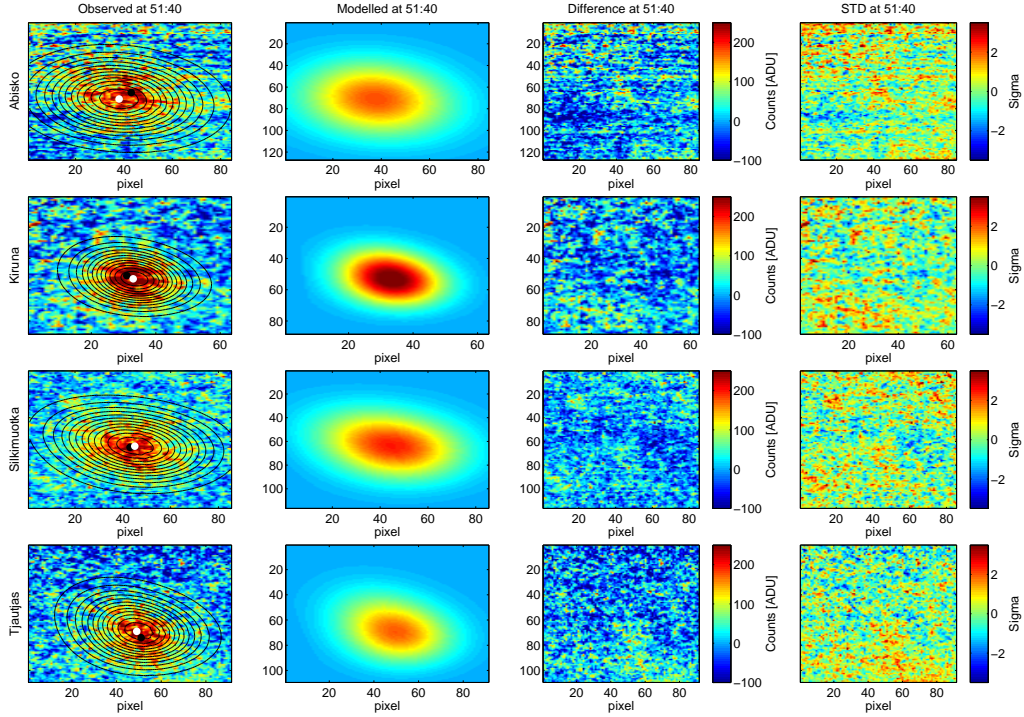
Figure 8.13: Simulation results using semi-theoretical curves during 5.423 MHz heating
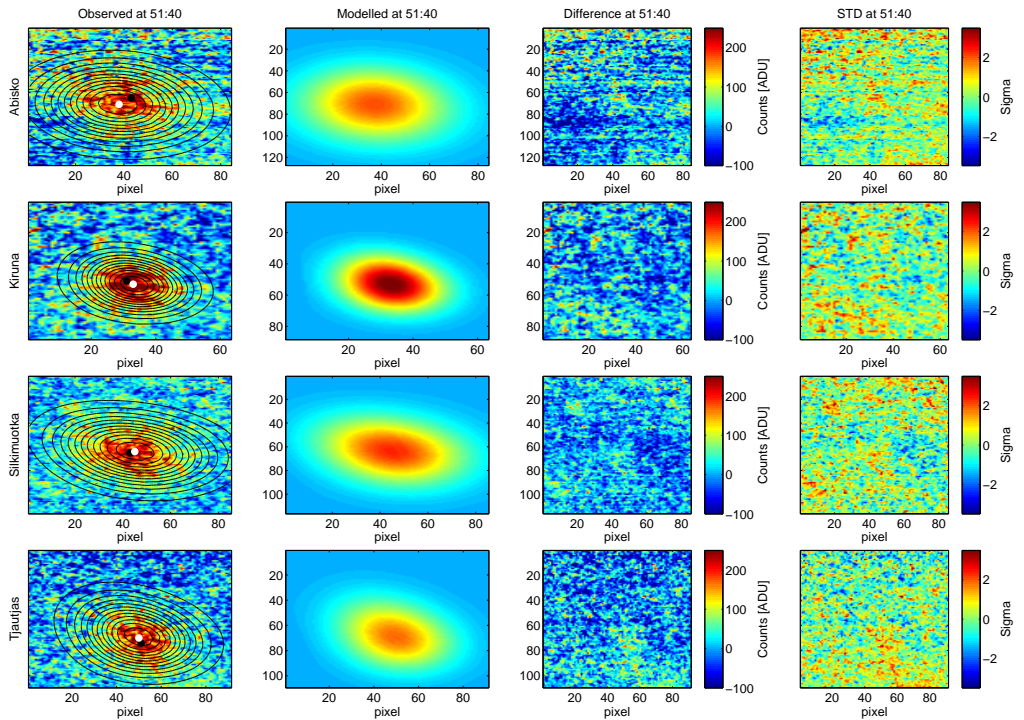
Figure 8.14: Simulation results using free parameter search during 5.423 MHz heating

The signal to noise ratio is lower for the 5577 Å emission than for the 6300 Å emission. Hence, the comparison between the binned pixel value distribution in the "difference"

image and the normal distribution is less useful for supporting or refuting the auroral construction model.
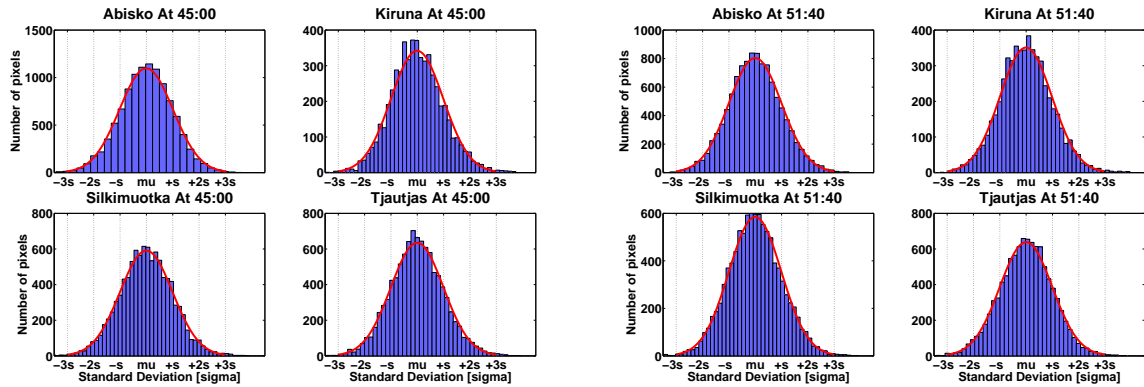
(a) Theoretical curves during 6.200 MHz   (b) Theoretical curves during 5.423 MHz
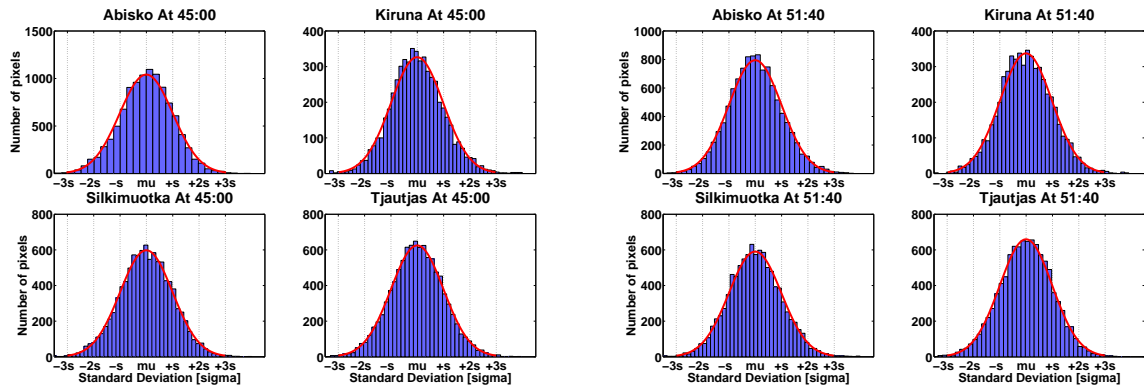
(c) Semi-theoretical curves during 6.200 MHz   (d) Semi-theoretical curves during 5.423 MHz
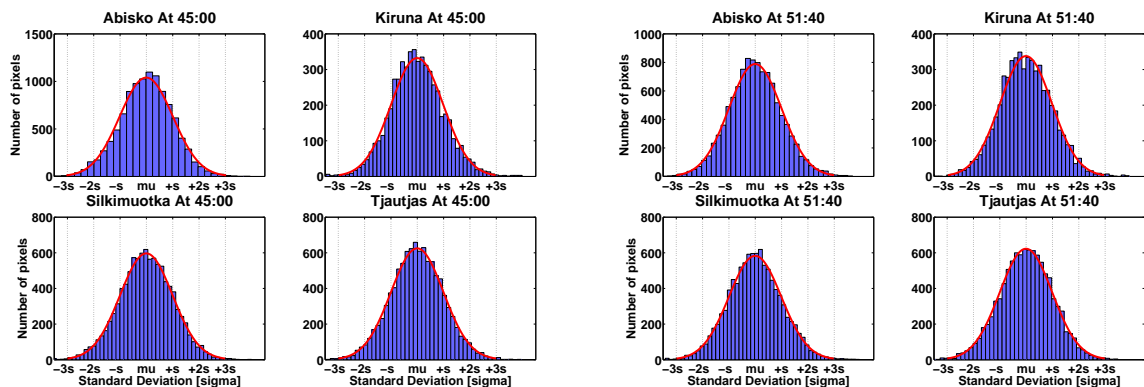
(e) Free parameter search during 6.200 MHz   (f) Free parameter search during 5.423 MHz

Figure 8.15: Comparison between binned pixel values in the "difference" images from the modelled-observed images, figures 8.9 - 8.14, and a fitted normal distribution.

The free parameter results and the χ^2_{red} values are presented in the table below:

Parameter	6.200 MHz frequency heating			5.423 MHz MHz frequency heating		
$I(counts)\cdot 10^6$	1.5 ± 0.3	3.3 ± 0.5	3.1 ± 0.6	1.3 ± 0.2	2.1 ± 0.2	1.7 ± 0.3
$x(km)$	-55 ± 2	-53 ± 1	-54 ± 1	-51 ± 1	-51 ± 1	-51 ± 1
$y(km)$	154 ± 1	151 ± 2	151 ± 2	160 ± 1	155 ± 2	155 ± 2
$z(km)$	238 ± 3	239 ± 3	232 ± 8	218 ± 3	212 ± 2	213 ± 10
$\sigma_r(km)$	11 ± 1			17 ± 2		
$\sigma_x(km)$		11 ± 1	11 ± 1		17 ± 2	18 ± 2
$\sigma_y(km)$		11 ± 3	11 ± 3		18 ± 2	16 ± 1
$\sigma_z^d(km)$			11 ± 5			21 ± 6
$\sigma_z^u(km)$			25 ± 5			26 ± 11
γ		8 ± 3			2 ± 4	
$\phi(deg)$		31.5 ± 0.6	38 ± 22		35.4 ± 0.3	68 ± 1
χ^2_{red}	1.7 ± 0.3	1.5 ± 0.3	1.5 ± 0.3	1.9 ± 0.5	1.8 ± 0.4	1.8 ± 0.4
Model:	Theo	Semi	Free	Theo	Semi	Free

Table 8.2: The mean and standard deviation values of the modelling during the 6.200 MHz and 5.423 MHz frequency is shown above. These estimates were done using 8 images under 6.200 MHz heating and 5 images during 5.423 MHz heating. Note that the diffusion and drift parameters are not needed for the 5577 Å modelling. This is due to the short radiative lifetime of the excited $O(^1S)$ state. The parameters are physically feasible.

The figure below shows the constructed emission volumes, at 45:00 UT and 51:40 UT, using the three different construction techniques:
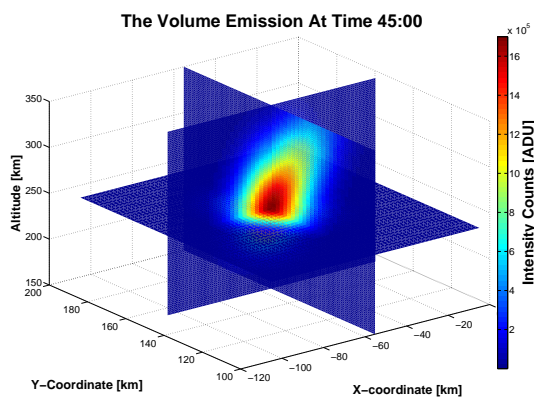
(a) Theoretical curves during 6.200 MHz
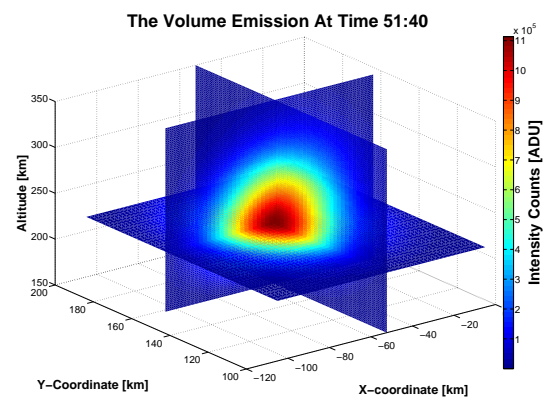
(b) Theoretical curves during 5.423 MHz
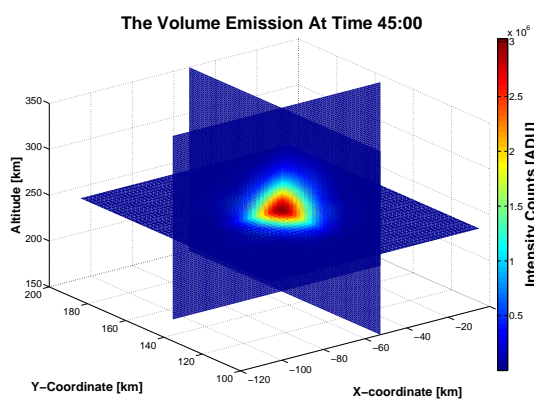
(c) Semi-theoretical curves during 6.200 MHz
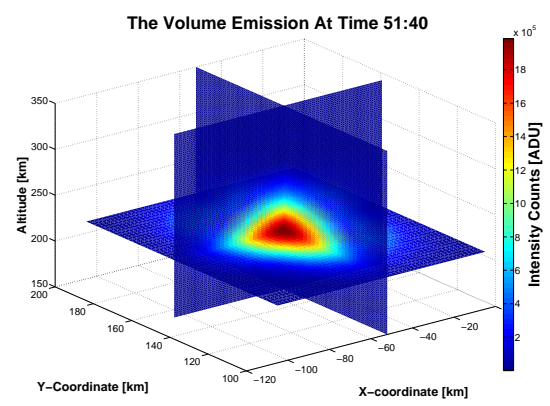
(d) Semi-theoretical curves during 5.423 MHz
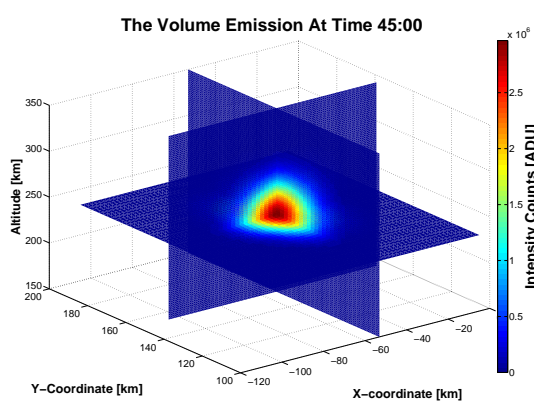
(e) Free parameter search during 6.200 MHz
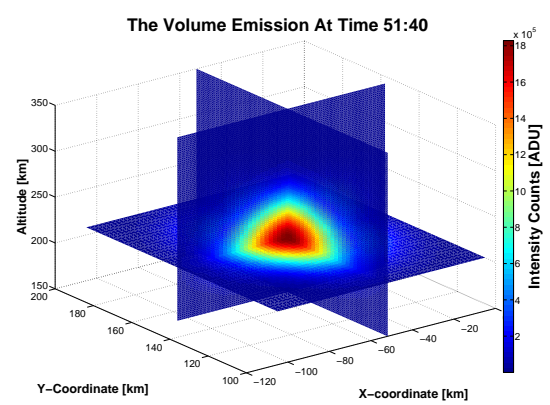
(f) Free parameter search during 5.423 MHz

Figure 8.16: The constructed volumes which are projected down to the modelled images in the modelled-observed images, figures 8.9 - 8.14. It is clear that the slice, through the point of maximum excitation rate, is also the point of maximum emission. This is not a surprise, since the de-excitation of the $O(^1S)$ state is assumed to instant. The volume emission therefore equals the volume excitation in the simulation.

8.3 The 8446 Å Emission Results And Analysis

The 8446 Å emission did only give sufficient signal to noise ratio for tomographic reconstruction during the 5.423 MHz frequency modulation. Unfortunately, there were only three stations equipped with the near infra-red filter, Abisko, Silkimoutka and Tjautjas. Reconstruction with two stations will not be attempted for the 8446 Å emission, the radio induced emission is too faint to give reliable results from only two images. Consequently, only two images were taken simultaneously at three stations and during 5.423 MHz frequency heating, at 52:00 UT and 53:15 UT. The 53:15 UT image from Tjautjas had a non-uniform background, the reason for this is unknown, light pollution or electric noise might have been present. This leaves the 52:00 UT images as the only useful data set for the tomographic modelling of the 8446 Å emission line. The results are presented below:
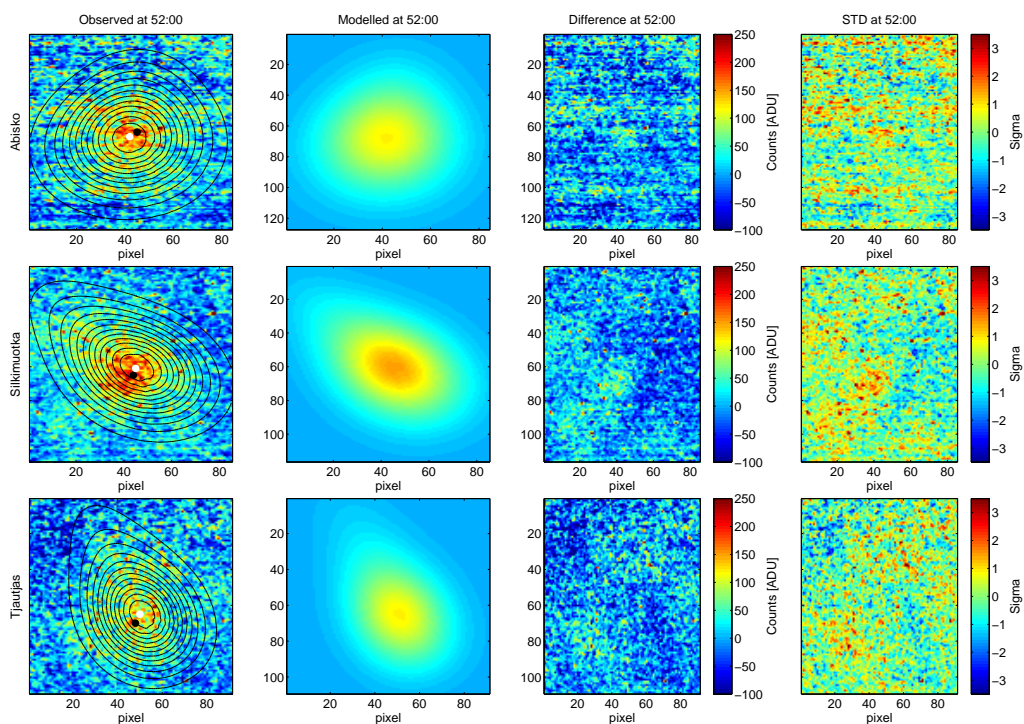
Figure 8.17: Simulation results using the theoretical curves construction technique during 5.423 MHz heating.
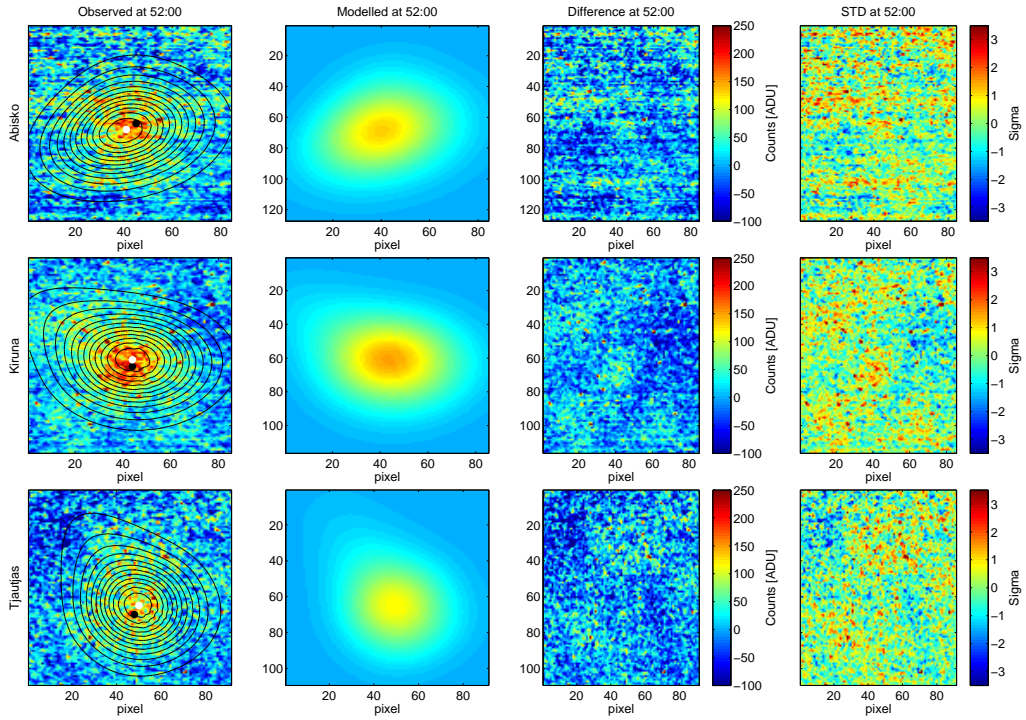
Figure 8.18: Simulation results using the semi-theoretical curves construction technique during 5.423 MHz
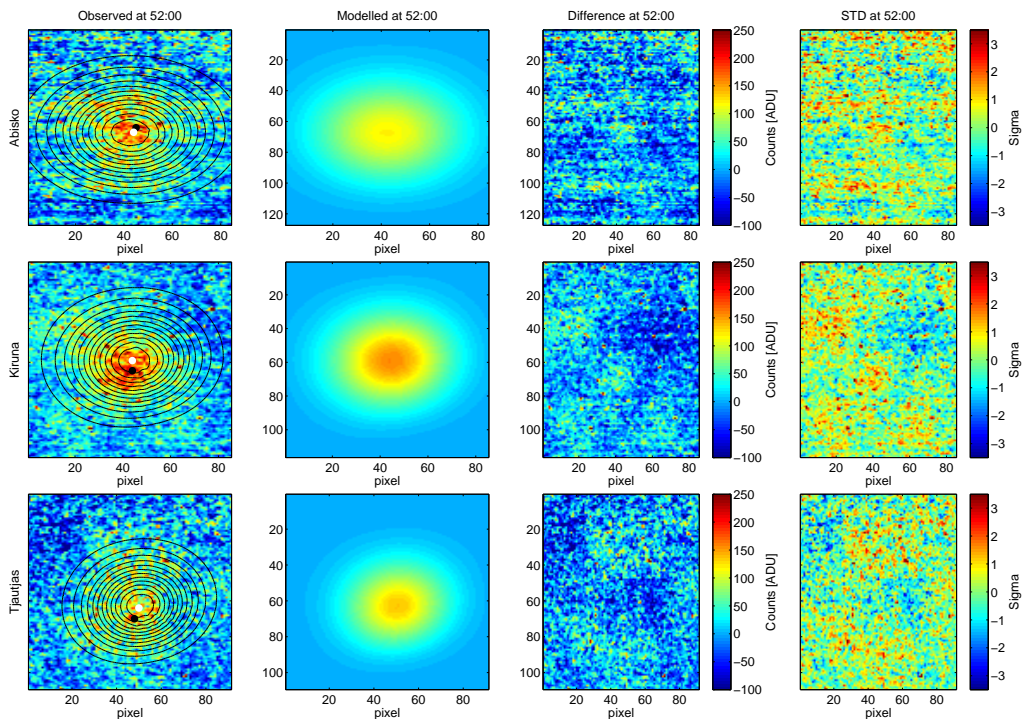
Figure 8.19: Simulation results using free parameter search construction technique during 5.423 MHz heating

Below are the parameters that produced the best fit between the observed and the modelled images for the three different construction methods:

Parameter	5.423 MHz MHz heating		
$I(counts) \cdot 10^6$	1.4	1.7	1.9
$x(km)$	-55	-53	-55
$y(km)$	151	152	151
$z(km)$	224	226	222
$\sigma_r(km)$	16		
$\sigma_x(km)$		19	19
$\sigma_y(km)$		12	20
$\sigma_z^d(km)$			12
$\sigma_z^u(km)$			15
γ		1.1	
$\phi(deg)$		30.0	1.4
χ_{red}^2	1.3	1.3	1.3
Model:	Theo	Semi	Free

Table 8.3: The results from the 5.423 MHz frequency heating at 52:00 UT. One data point means no mean or uncertainty estimates. However, the parameters seems physically feasible. The de-excitation of the $O(^3P)$ state is assumed to occur immediately after excitation. Hence, the diffusion and wind parameters are not needed in the 8446 Å modelling.

The figure below shows the constructed emission volumes and the normal distribution fitting at 52:00 UT, using the three different construction techniques:
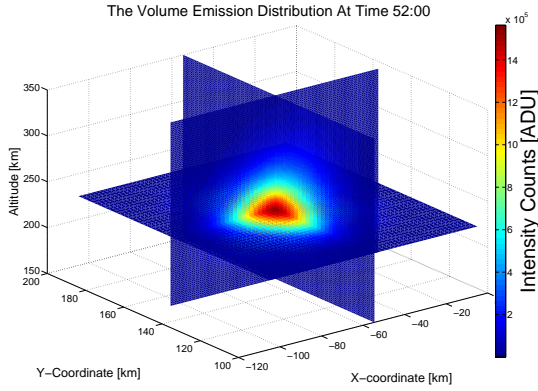
(a) Theoretical curves during 5.423 MHz
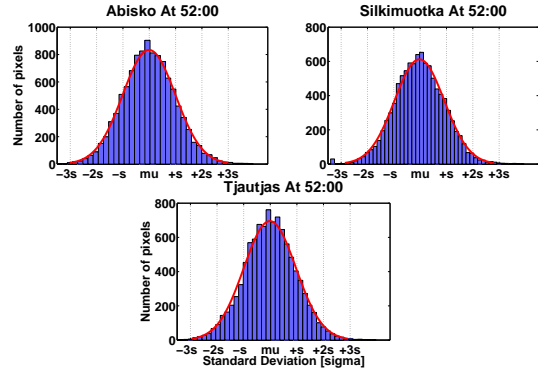
(b) Theoretical curves during 5.423 MHz
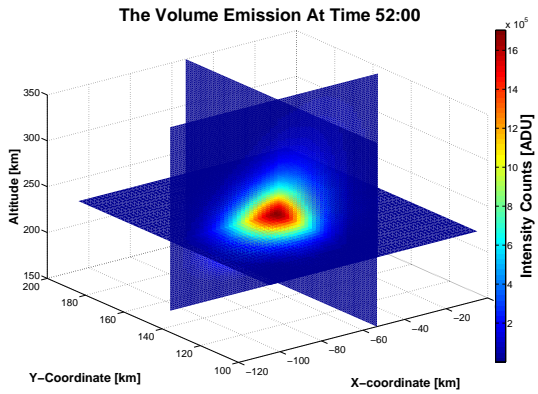
(c) Semi-theoretical curves during 5.423 MHz
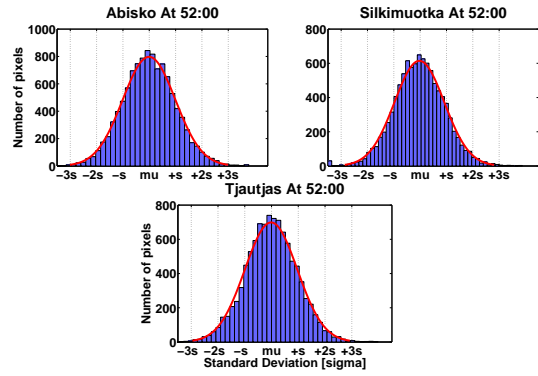
(d) Semi-theoretical curves during 5.423 MHz
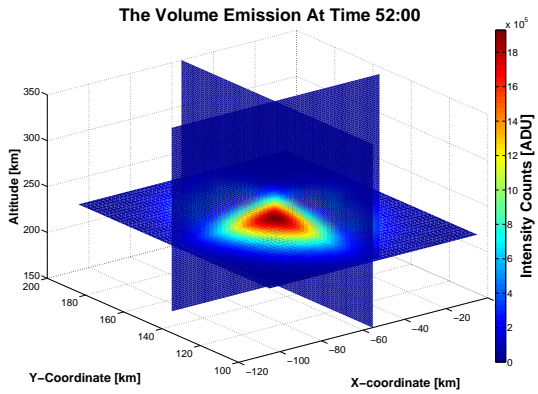
(e) Free parameter search during 5.423 MHz
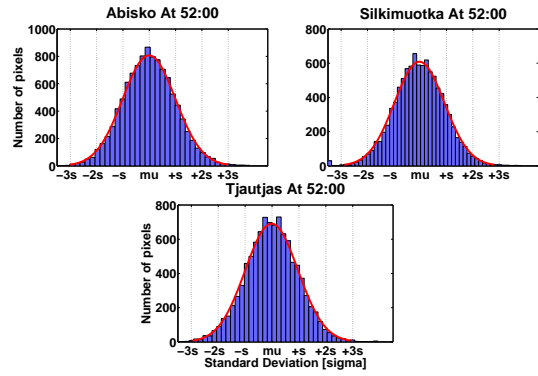
(f) Free parameter search during 5.423 MHz

Figure 8.20: To the left, the constructed volumes which are projected down to the mod-elled images in the modelled-observed images, figures 8.17 - 8.19. To the right, comparison between binned pixel values in the "difference" images from the comparison images and a fitted normal distribution. The number of pixels within a count interval are given by the purple posts and the fitted normal distribution is represented by the red line. The emission center is in the center of the slice plot. This means that the excitation and the emission centres are at the same point. The reason for this is the short radiative lifetime of the excited $O(^3P)$ state, which makes it possible to ignore the effect of the $O(^3P)$ lifetime, diffusion and drift.

8.4 The Time Evolution Of The Aurora

So far, the only presentation of the auroral parameters are given in tables 8.1, 8.2 and 8.3. However, the time evolution of some of these parameters are of interest. The time evolution of the height, width and the total volume emission of the 6300 Å and 5577 Å emission modelling will be presented in this section.

(a) Theoretical Height

(b) Theoretical Width

(c) Semi-theoretical Height

(d) Semi-theoretical Width

(e) Free search Height

(f) Free search Width
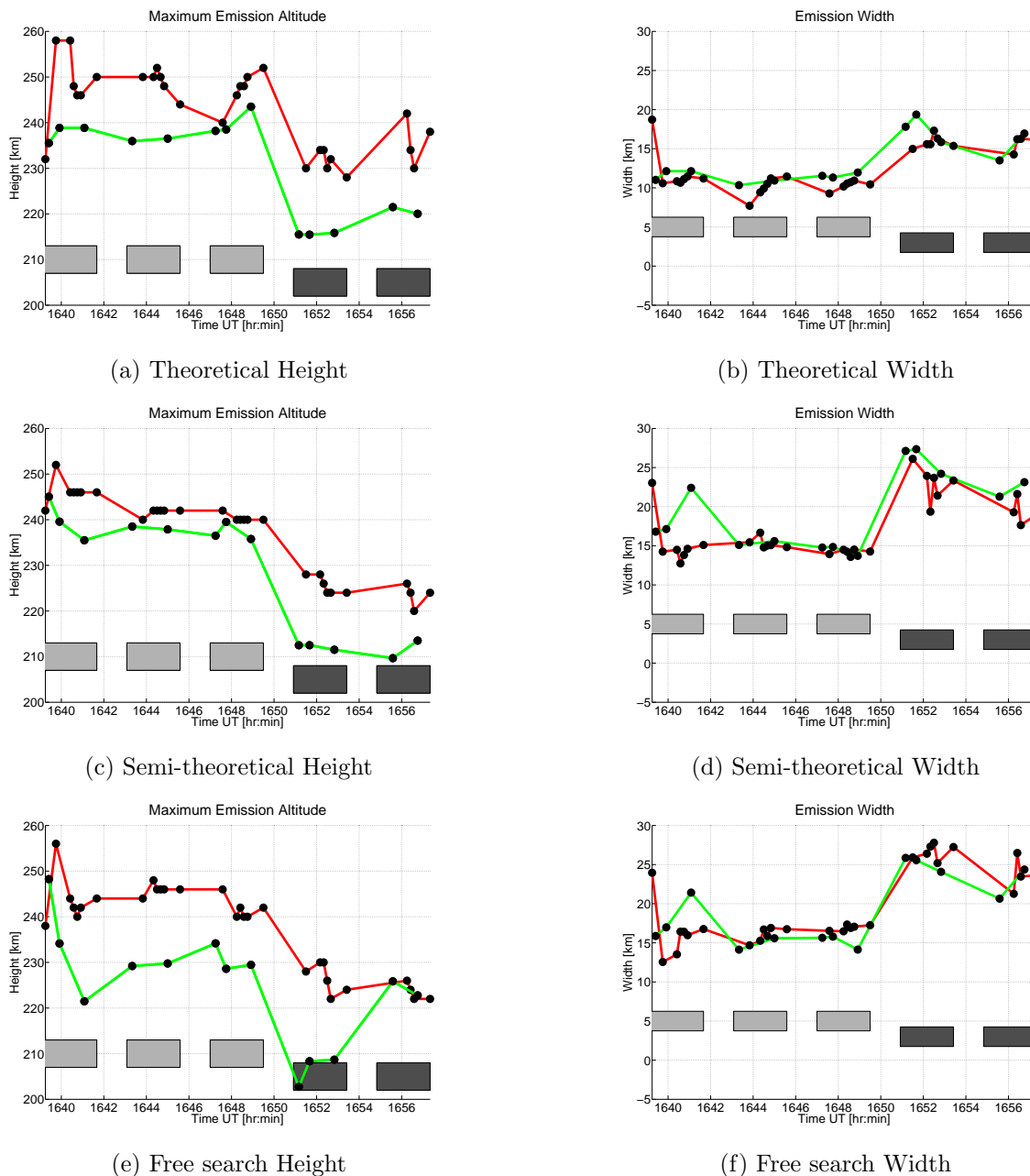
Figure 8.21: The red line represents the heights and widths of the 6300 Å emission. The green line represents the heights and widths of the 5577 Å emission. The widths are in $\pm\sigma$, the half widths of the emission blobs.
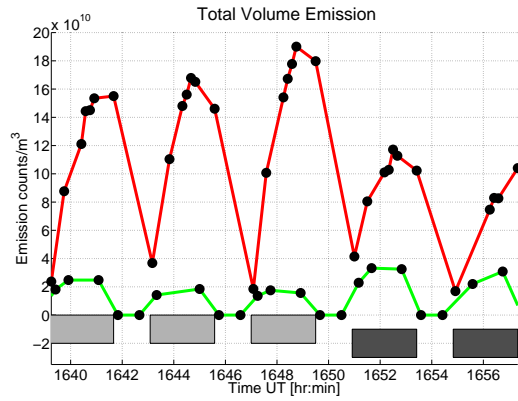
(a) Total theoretical volume emission
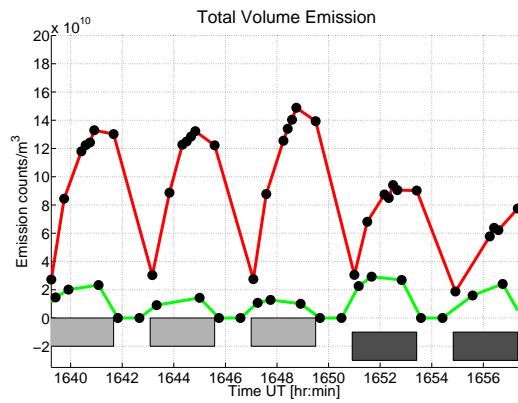
(b) Total semi-theoretical volume emission
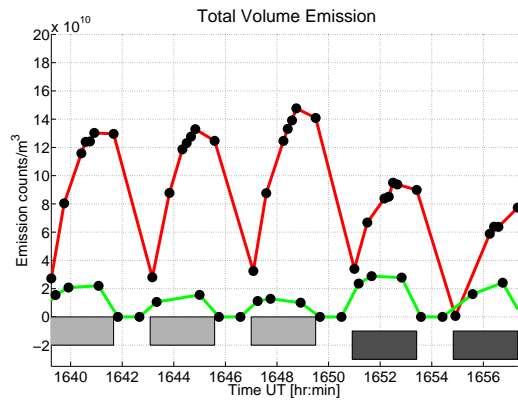
(c) Total free search volume emission

Figure 8.22: The red line represents the 6300 Å emission and the green line represents the 5577 Å emission.

8.5 The Emission Profiles

It is difficult to get a proper grasp of the volume emission distribution from the parameters and the volume emission slice figures alone. This section will therefore present the emission volumes as functions of altitude:
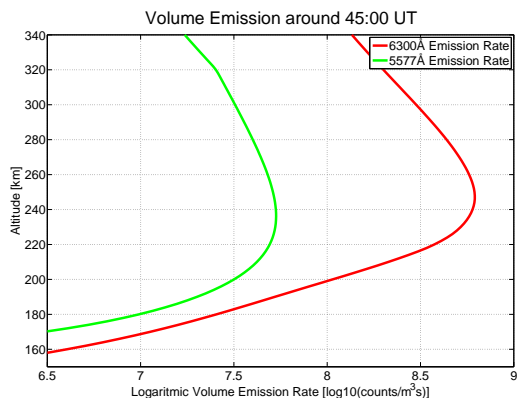
(a) Theoretical profile during 6.200 MHz
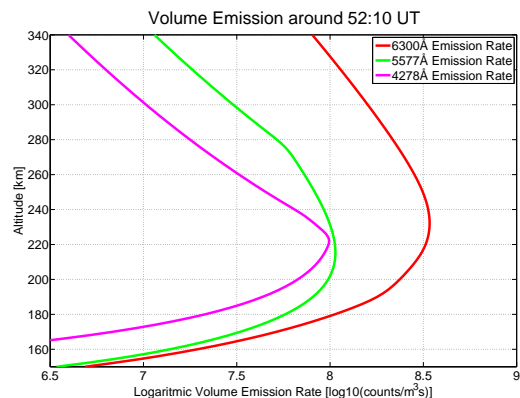
(b) Theoretical profile during 5.423 MHz
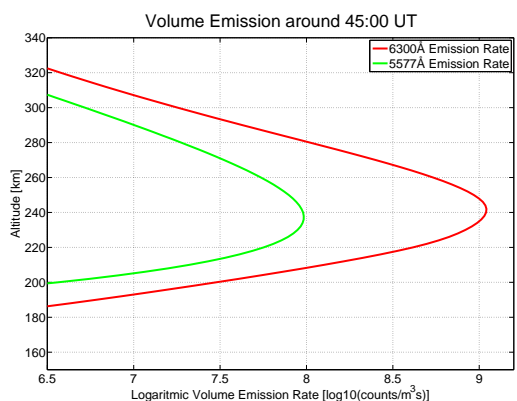
(c) Semi-theoretical profile during 6.200 MHz
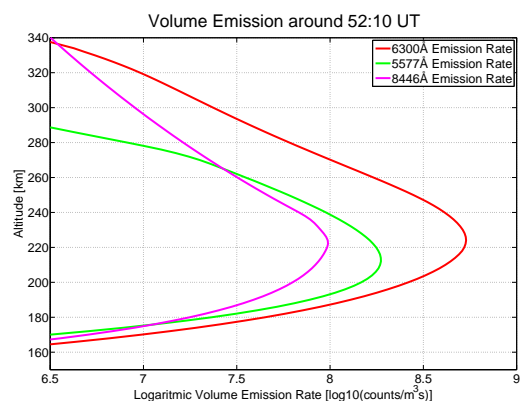
(d) Semi-theoretical profile during 5.423 MHz
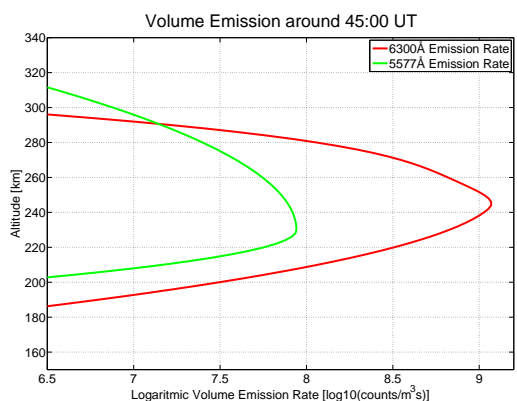
(e) Free search profile during 6.200 MHz
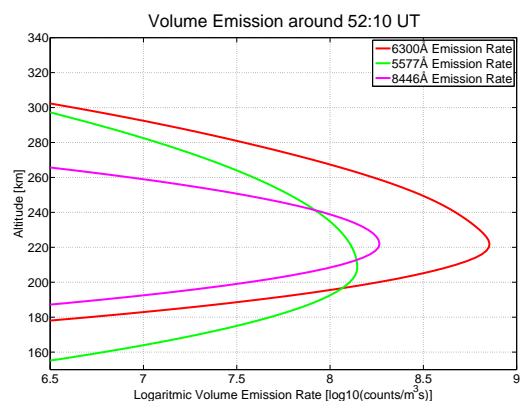
(f) Free search profile during 5.423 MHz

Figure 8.23: The figures above shows the emission profiles, the total volume emission distribution as a function of altitude. Note that the volume emission rate scale is logarithmic.

Discussion

9.1 Evaluation Of The Thermal Electron Excitation Theory

The thermal electron excitation theory, described in section 3.2, predicts a steady state ratio of the 5577 Å and the 6300 Å emission intensities, determined by a Maxwellian electron energy distribution. The steady state ratio can therefore be predicted by using equation 3.5 and the EISCAT measured electron temperatures. The figure below shows the steady state 5577 Å and 6300 Å emission intensity ratio curve:
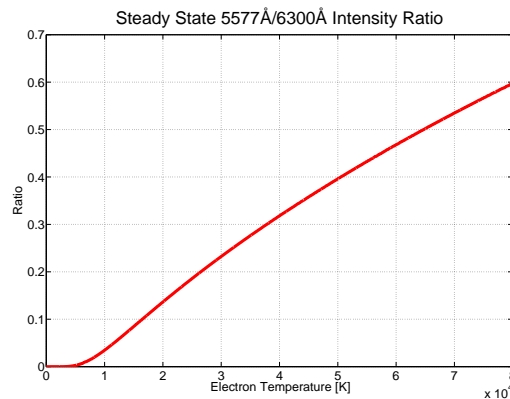
Figure 9.1: The figure shows the steady state ratio between the 5577 Å and 6300 Å emission intensities as a function of temperature. The effective lifetime of $O(^1D)$, τ_{O1D}, is set to 24 seconds which is the theoretical effective lifetime value at the peak emission height, see figure 4.2. The transition probability, A_{6300} is set to $0.0071s^{-1}$, as suggested in [Gustavsson et al., 2002].

The enhancements of the total volume emission in figure 8.22 will be used to estimate the intensity ratios. The enhancement estimates are taken from the semi-theoretical and

free parameter search figures, since they are in good agreement with the observed images. The total count value of the entire emission volume, at steady state, is approximately $13 \cdot 10^{10}$ for the red line and $1.8 \cdot 10^{10}$ for the green line during the 6.200 MHz heating. This gives a ratio of 0.14, corresponding to a theoretical thermal electron temperature of 20000 K. The thermal electron temperature is not in agreement with the EISCAT measured temperature of 3300 K, see figure 3.2, during 6.200 MHz heating.

During the 5.423 MHz heating, the 6300 Å volume emission reached a total of $9.7 \cdot 10^{10}$ counts, whereas the 5577 Å emission had a steady state at $2.7 \cdot 10^{10}$ counts. This gives a ratio of 0.28, corresponding to a theoretical temperature of 36000 K. Hence, the theoretical temperature estimate during the 5.423 MHz heating do not agree with the measured temperatures in figure 3.2.

In addition, the thermal electron excitation theory do not provide an explanation for the source of the 8446 Å emission. The 8446 Å emission is caused by de-excitation of the $O(^3P)$ state, which has a threshold energy of 10.99 eV. The Maxwellian electron energy distribution can not be the source of the excited $O(^3P)$ states. It was shown in table ?? that a proportion of $5.6 \cdot 10^{-22}$ electrons will have enough energy to excite the $O(^3P)$ state. This is not in agreement with the observed enhancement seen in figure 4.4. It can bee seen, by comparing figures 4.4 and 4.3, that the I_{8446}/I_{5577} ratio is approximately 0.8 during the 5.423 MHz heating. This ratio is far from the electron energy ratio:

$$\frac{E_{8446}}{E_{5577}} = \frac{5.6 \cdot 10^{-22}}{2.0 \cdot 10^{-8}} = 2.8 \cdot 10^{-14} \tag{9.1}$$

Where E_{8446} is the proportion of electrons with energies higher than the $O(^3P)$ threshold and E_{5577} is the proportion of electrons above the $O(^1S)$ threshold, from a 2500 K Maxwell electron distribution. The I_{8446}/I_{5577} and E_{8446}/E_{5577} ratio difference can not be explained by cross section or reaction rate differences. Hence, the EISCAT temperature measurements and the emission enhancements shows clearly that: The theoretical temperature predictions and the high I_{8446}/I_{5577} ratio are strongly conflicting with the thermal electron excitation theory.

9.2 Evaluation Of The Construction Techniques And The Accelerated Electron Excitation Theory

The observational-modelled comparison images presented in chapter 8 and in appendix A all show the same trend: The theoretical curves construction technique provides the least reliable modelling of the artificial aurora. Whereas the semi-theoretical curves and the free parameter search construction techniques provides modelled auroral projections with appearances close to the observational images.

This trend is supported by the results from the reduced Pearson's chi-squared number χ^2_{red} and the normal distribution fitting with the observational-modelled "difference" images. See tables 8.1, 8.2 and 8.3 for the reduced Pearson's chi-squared numbers and figures 8.7, 8.15 and 8.20 for the normal distribution fitting to the binned pixel values of the observational-modelled "difference" images. The only exception to this trend is the

8446 Å modelling. However, the 8446 Å emission is weakest emission line, with emission enhancements close to the natural variations of the background airglow. Hence, the near infra-red emission simulations provides the least reliable modelling results. Nevertheless, the acquired 8446 Å artificial auroral parameters are physically possible, and there are no reasons to discard the results although the reliability is low. The 6300 Å and 5577 Å emissions have higher signal to noise ratios and the modelling is done employing more observational images. In addition, the artificial auroral construction parameters are physically sound. Hence, the semi-theoretical and the free parameter search modelling, which were in agreement with the observed images, provide statistically feasible parameters.

The semi-theoretical and the free parameter search hight and width results will be used to compare the modelled results to the accelerated electron excitation theory, as proposed in section 3.3. The maximum emission height curves in figure 8.21, show that the 6300 Å emission height is above the 5577 Å emission. The triangulation results in appendix B support this trend. This is a consequence of the long radiate lifetime of the excited $O(^1D)$ state, 107 seconds. The neutral density gradient will cause more collisional de-excitation of the $O(^1D)$ states at lower altitudes. This will lead to an upward shift in the 6300 Å emission height. This shift was estimated in [Gustavsson and Eliasson, 2008] to be approximately 15 km at 230-250 km, see figure 3.6. The 5577 Å emission line is caused by de-excitation of $O(^1S)$, with a radiative lifetime of 0.7 seconds. Hence, the collisional de-excitation of $O(^1S)$ will be small compared to the radiative de-excitation. This means that the 5577 Å emission center will be close to the excitation center. The shift between the maximum 5577 Å emission height and the maximum 6300 Å emission hight can therefore be used as an estimate of the altitude shift of the 6300 Å emission above the acceleration height, comparabel to the shift preditions in figure 3.6. The 15 km shift is roughly in agreement with the free-parameter search during the 6.200 MHz heating, if the first 3 green data points are excluded, but not in agreement with the semi-theoretical emission heights. However, the semi-theoretical emission hight shift is roughly in agreement with the shift during the 5.423 MHz heating, whereas the free parameter search heights are not. The modelled emission widths and the predicted emission widths show different emission width ratios and tendencies. Note that the emission widths presented in figure 8.21, is only the half width, whereas the widths in figure 3.7 are the full widths. The emission widths predicted by the accelerated electron flux simulation shows a decrease in emission width at lower altitudes. This is in conflict with the results presented here, the widths are increasing at lower heating altitudes. The reason for this conflict is unknown. However, the overall tendency is clear: The modelled results, from the semi-theoretical and free parameter search constructions, are not in agreement with the accelerated electron flux simulation [Gustavsson and Eliasson, 2008]. Neither the predicted 6300 Å emission height shift nor the predicted emission widths are in agreement with the modelled results. In addition, the theoretical excitation curves, which were acquired using the accelerated electron flux simulation, provided the least credible modelling of the artificial aurora, as seen in the observational-modelled comparison images presented in chapter 8.

It is difficult to evaluate if the semi-theoretical curves modelling is better or worse than the free parameter search modelling. Both construction techniques provide relatively similar construction parameter values, error margins included, and the model reliabil-

ity, determined by the observational-modelled comparison images,, the χ^2_{red} numbers and normal distribution fitting with the observational-modelled "difference" images, are almost equally good. In addition, both construction techniques show the same tendency: Most of the modelled emission lies within a thinner layer than what is predicted by the accelerated electron curves.

The sharpening of the semi-theoretical and free parameter emission curves around the peak emission is clearly seen in figure 8.23. It is reassuring that both the semi-theoretical and the free parameter search show this tendency, and that the semi-theoretical and the free parameter emission profiles are relatively similar. This indicates that the modelling and the minimization of the least squares are giving reliable results. This is not obvious since the semi-theoretical and free parameter techniques are constructing the aurora differently. However, the profiles are increasingly deviating towards the bottom and top of the main emission layer, approximately 20 km below and 25 km above the maximum emission altitude.

The reason why the emission profiles from the two different construction techniques do not properly converge, might be the choice of free parameters. The semi-theoretical curves might require additional shape parameters to account for different ionospheric conditions. The ionospheric conditions during the March 3. 2002 heating experiment, from which the accelerated electron excitation curves were estimated from, might be different to the ionospheric conditions during the February 16. 2015 experiment. For the free parameter search, the choice of two different altitude widths, below and above the excitation midpoint, might not be enough. A height dependent excitation parameter, proportional to the neutral density, could be used to account for the electron mean free path gradient.

CHAPTER 10

Conclusion And Outlook

In this thesis, the three dimensional emission distribution of artificial auroras, induced by HF radio waves in the ionosphere have been modelled using three different construction techniques: Theoretical curves, semi-theoretical curves and free parameter search.

It is clear, from comparisons with observational images and statistical analysis, that the semi-theoretical curves and the free parameter search construction techniques provided physically sound and statistically feasible construction parameters. Whereas modelling by employing the accelerated electron excitation theory curves from [Gustavsson and Eliasson, 2008] did not provide modelled aurora projections in agreement with observational images. In addition, the 6300 Å emission shift above the excitation altitude center and the 5577 Å and 6300 Å emission widths, predicted by the accelerated electron excitation model, did not agree with the modelling results.

It has been shown in this thesis that the EISCAT measured temperatures and the theoretically predicted temperatures, using the thermal electron excitation theory and the observed 5577 Å and 6300 Å emission intensity ratio, are strongly conflicting. The credibility of the thermal electron excitation theory is further reduced by the observed 8446 Å emission enhancements during 5.423 Mhz heating.

An additional goal of this thesis was to develop good data reduction methods. This has been done in appendix C. In this appendix, it was shown that the data reduction gave the desired result. The emission from the heating blob was isolated from the background light and the count values outside the heating blob appeared to be stochastic with no apparent trends or skews.

The programs for the data reduction and the auroral construction can be adapted for tomographic reconstruction of other ionospheric heating events. However, it is recommended, if using the semi-theoretical curves, to employ additional parameters to account for different ionospheric heating conditions. Furthermore, if the free parameter search

construction technique is used, it is suggested to add a height dependent excitation altitude width parameter. The parameter can be proportional to neutral density gradient. The excitation altitude width parameter will then account for the electron mean free path gradient in the ionosphere.

It will be beneficial in future artificial auroral tomographic reconstruction attempts to employ at least two different construction methods, e.g. the semi-theoretical and the free parameter search construction techniques. This is recommended since there might be several construction parameter combinations which constructs modelled auroras with projections similar to the observational images. This means that the observational images might have several converging modelled solutions. This is a consequence of the clustered location of the ALIS cameras, all the imaging stations are below and south of the radio induced emission blob. Hence, the modelled images are close to being linearly dependent. The projected model "aliases" can be detected if the differently constructed models converge towards different solutions. On the other hand, if the different construction techniques provide similar artificial auroral emission volumes, it will greatly increase the reliability of the modelled construction techniques and parameters.

It has been shown in this thesis that both the semi-theoretical and the free parameter search construction techniques provide relatively similar construction parameters, error margins included. In addition, both the semi-theoretical and the free parameter search construction provide auroral models where most of the enhanced emission lies within a thinner layer around the peak excitation height than what is predicted by the accelerated electron excitation theory curves. This can be seen in the altitude-emission profiles in figure 8.23. The semi-theoretical and the free parameter search altitude-emission profiles are in relatively good agreement within the main emission layer, approximately 20 km below and 25 km above the maximum emission altitude. This indicates that the excitation of constituents in the ionosphere during HF heating do no come from an isotropically distributed electron flux, as assumed in the accelerated electron excitation modelling in [Gustavsson and Eliasson, 2008]. The reason for this might be that the accelerated electrons are less effected by the isotropic scattering, due to elastic collisions at the acceleration height, than what has previously been assumed.

Tomography Results

141 artificial auroras have been modelled and compared to observational images. All of these comparisons can not be shown. In this appendix, the comparisons from two 6300 Å and two 5577 Å emission enhancement times will be presented. These comparisons were not shown in the main body to shorten the "Simulation Results And Analysis" chapter. However, they are included here, mainly to show that the results presented in the main body are not unique.

A.1   Additional 6300 Å Emission Results

The modelling of the 6300 Å emission enhancement of the maximum of the first modelled heating pulse will be presented first:
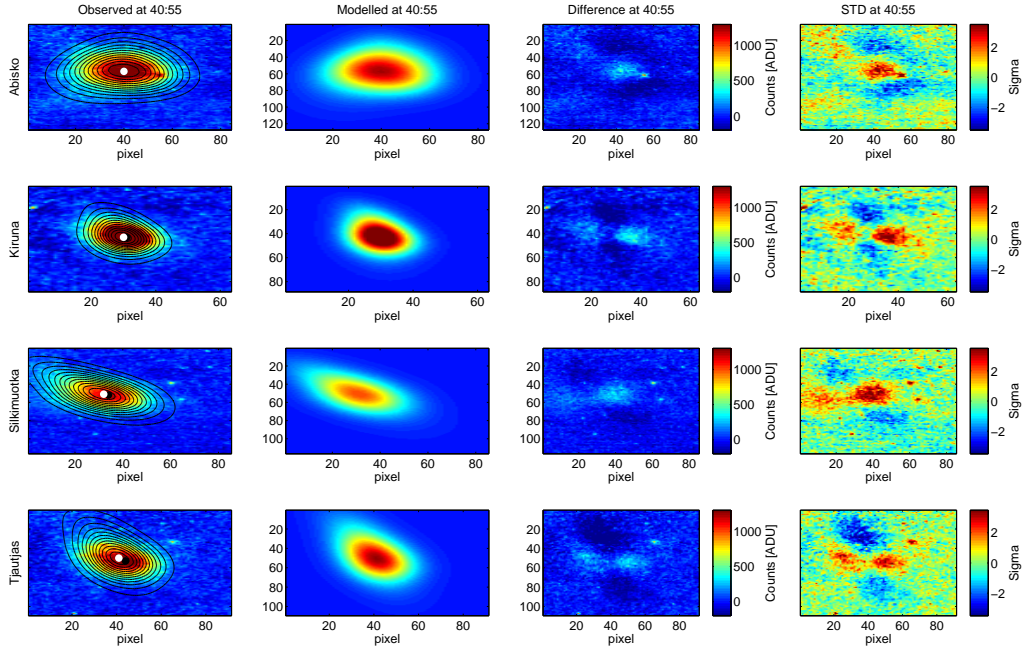
Figure A.1: Simulation result using the theoretical curves construction technique during 6.200 MHz heating. An explanation of the images and what they represent was given in figure 7.1.
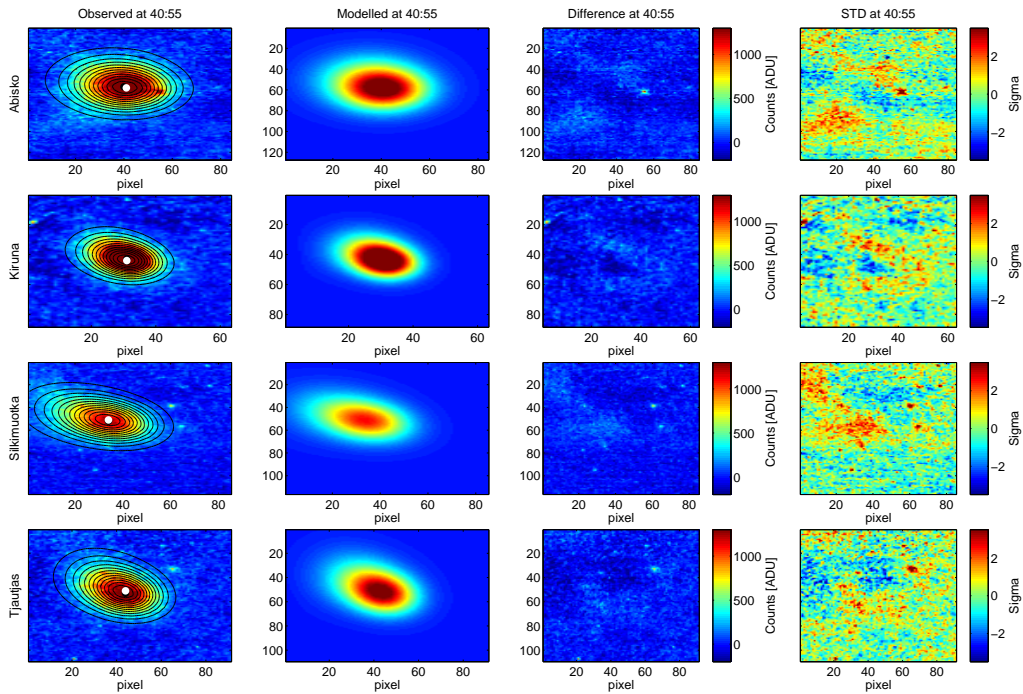
Figure A.2: Modelling results using the semi-theoretical curves construction technique under 6.200 MHz heating
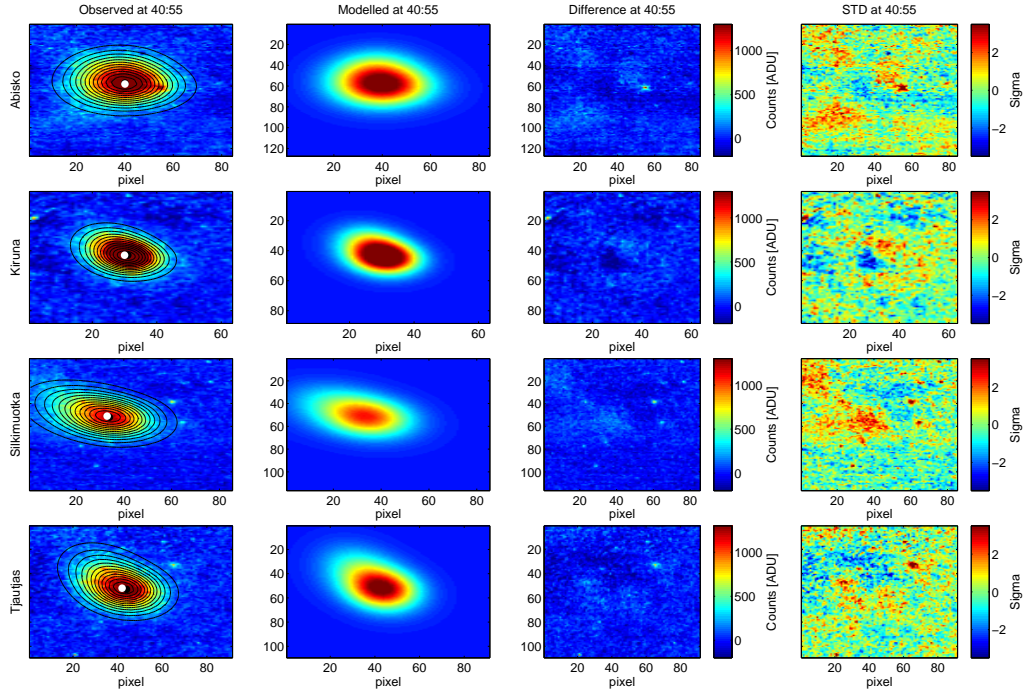
Figure A.3: Modelling results using the free parameter search construction technique during 6.200 MHz heating

The 6300 Å emission enhancement at the enhancement minimum will now be shown. This is done to measure of the modelling background, and to have a glance at the "difference" and standard deviation images are at minimum. This is of interest because it is desirable to know how smooth and uniform the standard deviation "background" is. When the standard deviation "background" is known, it is easier to say how much the standard deviation image during heating maximum differ from the standard deviation "background".
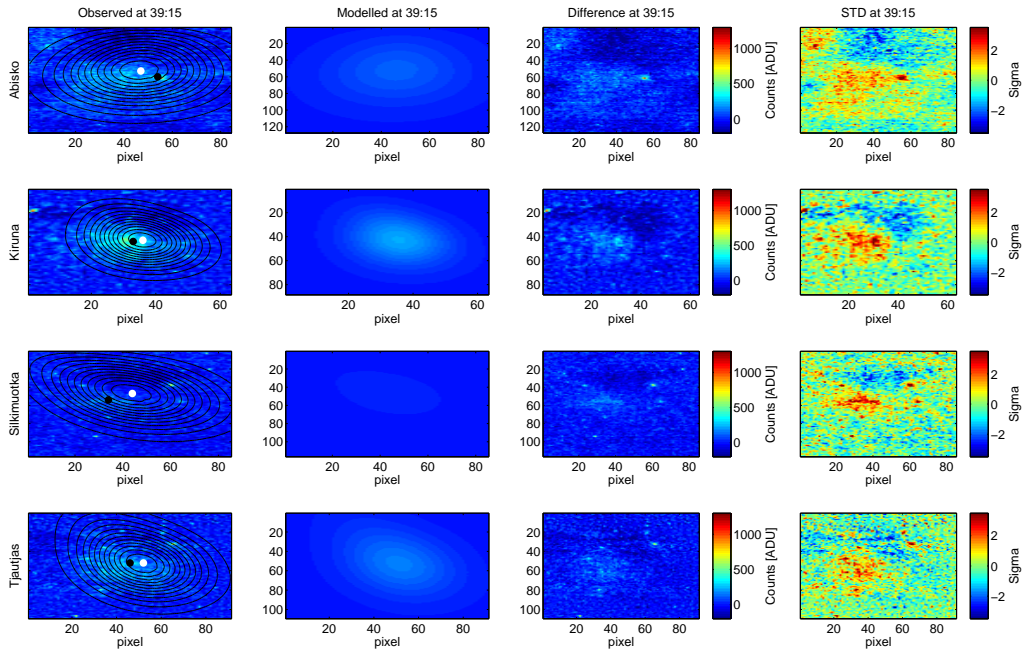
Figure A.4: Simulation results using the theoretical curves construction technique at emission enhancement minimum.
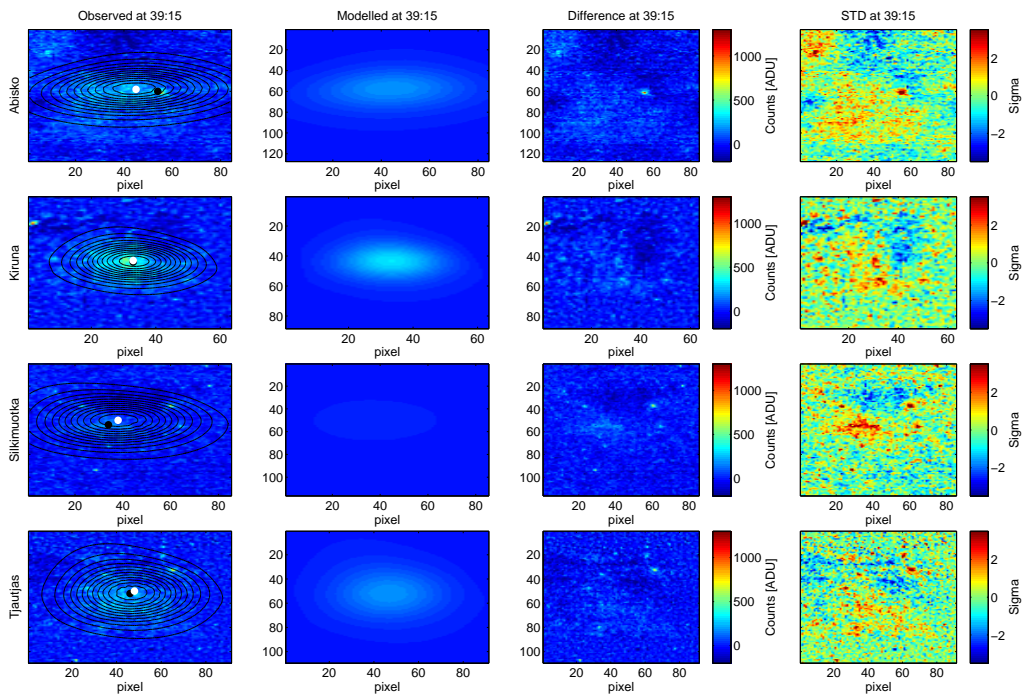
Figure A.5: Modelling results using the semi-theoretical curves construction technique at emission enhancement minimum
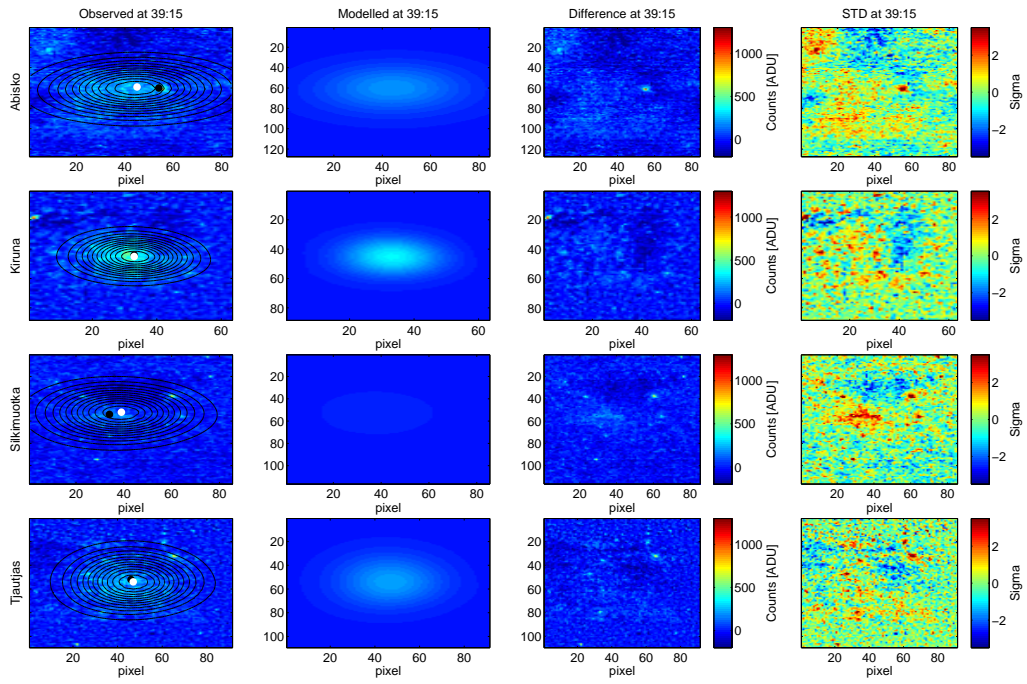
Figure A.6: Modelling results using the free parameter search construction technique at emission enhancement minimum

A.2 Additional 5577 Å Emission Results

The comparison results from two additional 5577 Å emission enhancement times will be presented in this section. The green line modelling of the emission enhancement at maximum during the first 6.200 MHz heating pulse will be presented first:
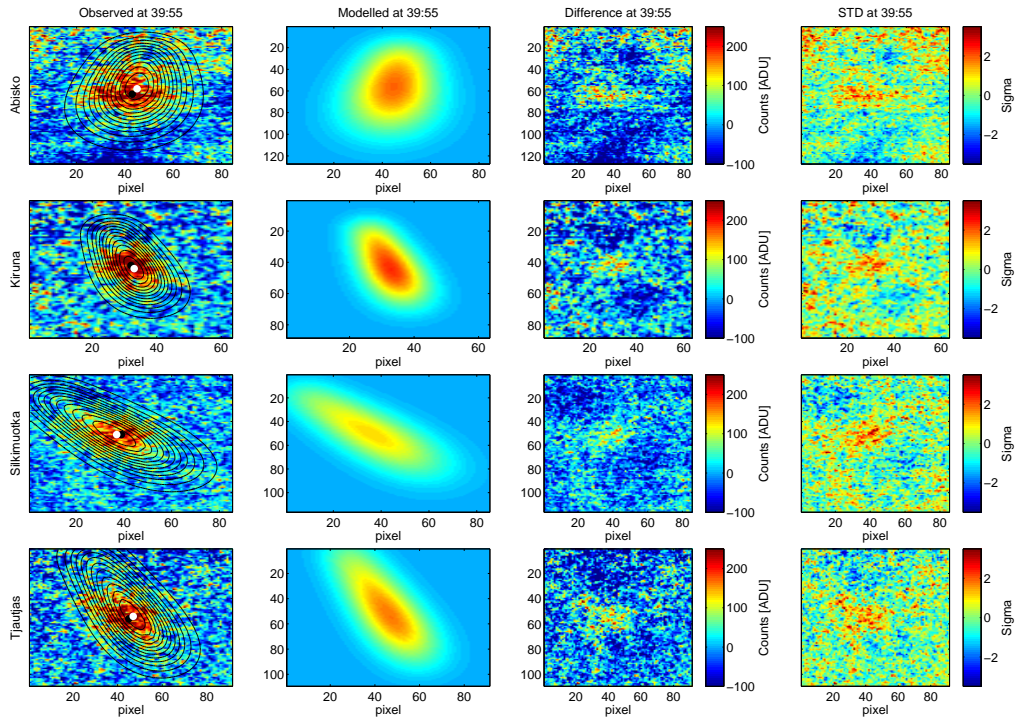
Figure A.7: Simulation results using the theoretical curves construction technique during 6.200 MHz heating.
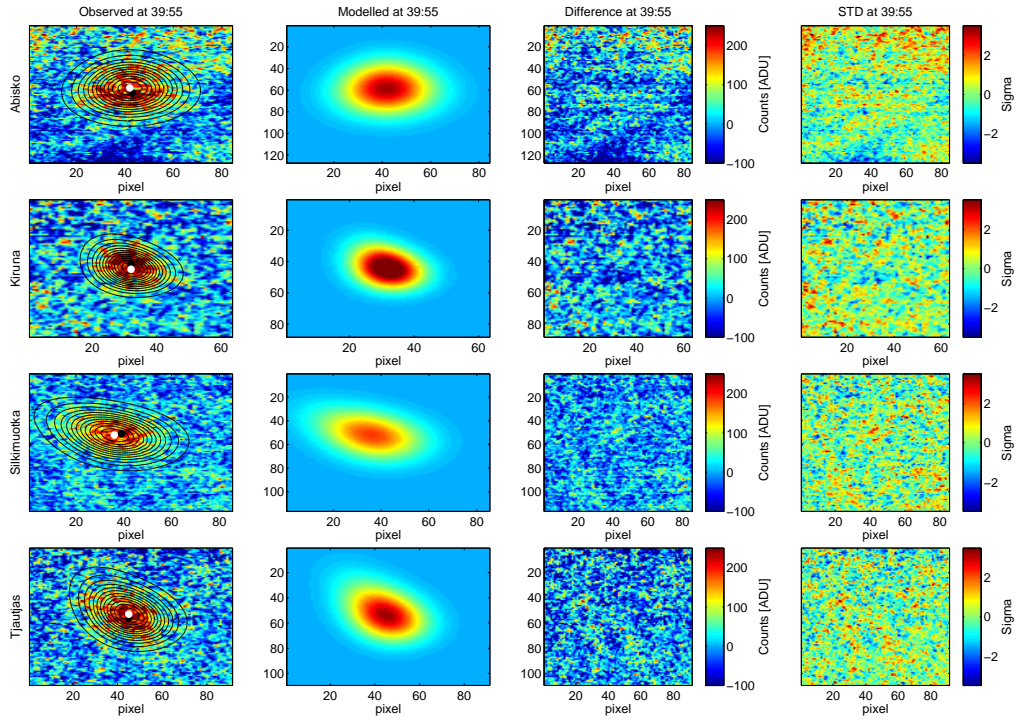
Figure A.8: Modelling results using the semi-theoretical curves construction technique under 6.200 MHz heating
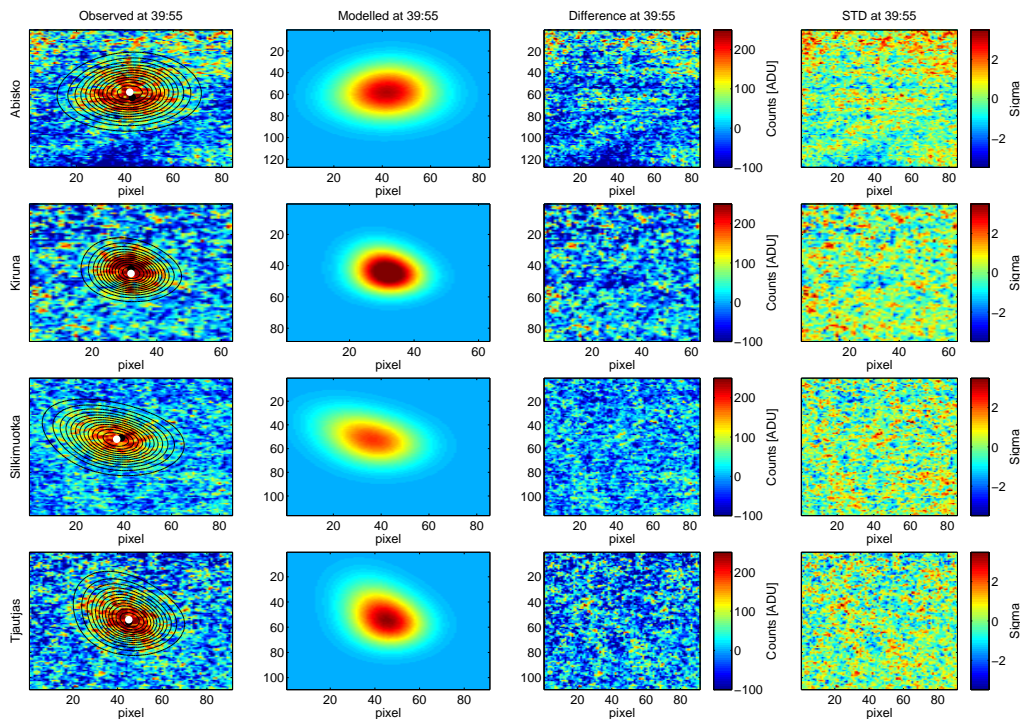
Figure A.9: Modelling results using the free parameter search construction technique during 6.200 MHz heating

The modelling comparison results from the last 5.423 MHz heating pulse are presented below:
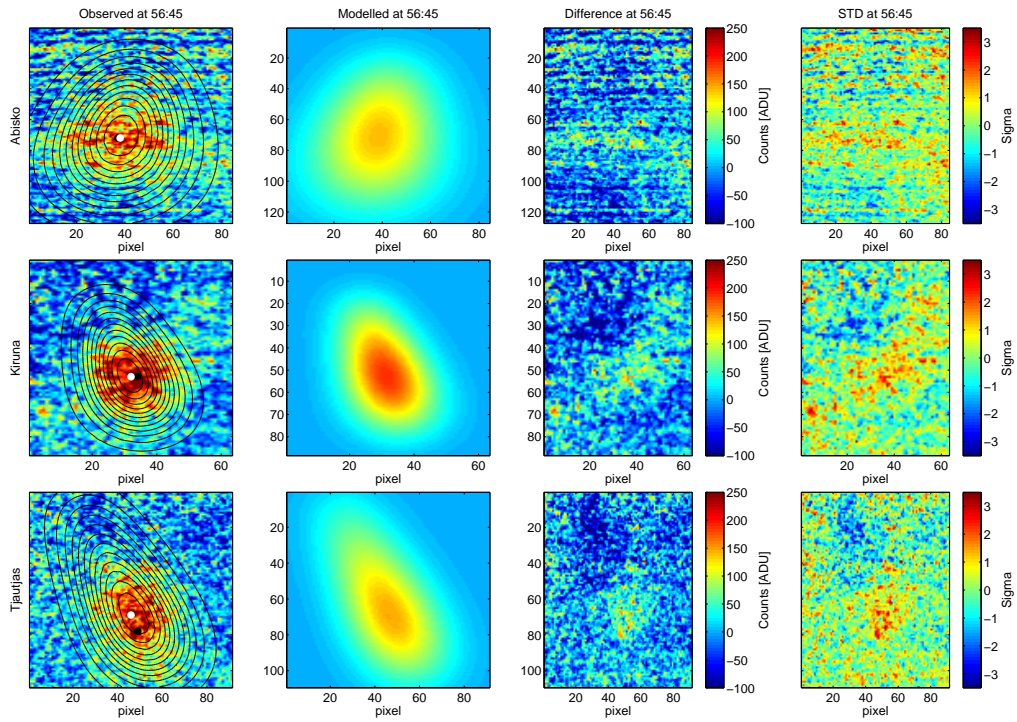
Figure A.10: Simulation results using the theoretical curves construction technique during 5.423 MHz heating.
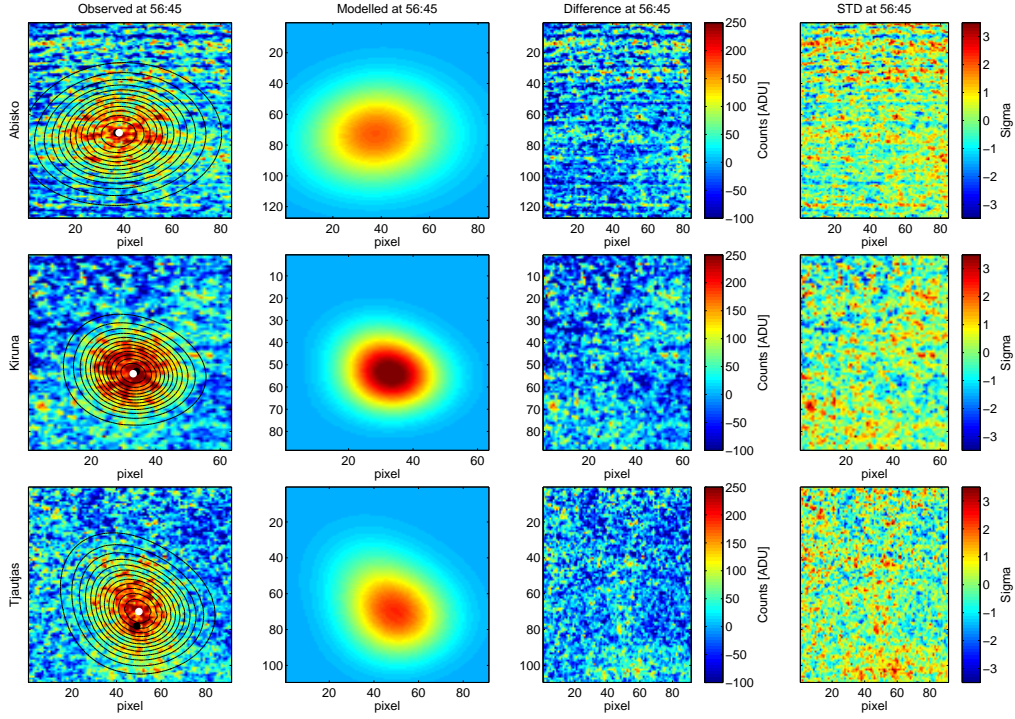
Figure A.11: Modelling results using the semi-theoretical curves construction technique under 5.423 MHz heating
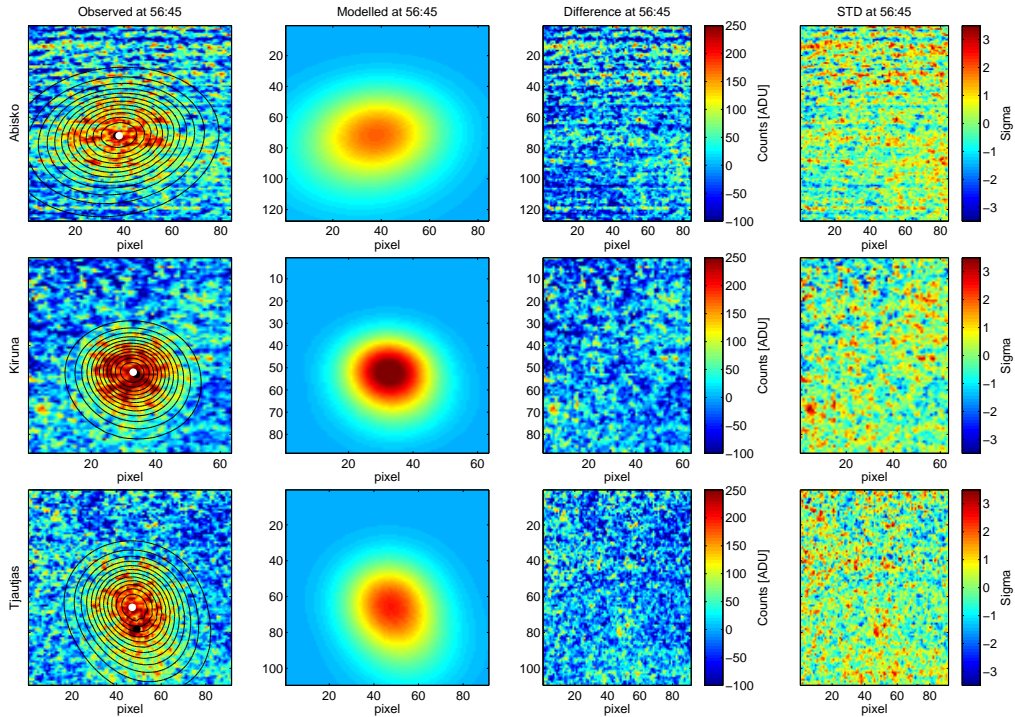
Figure A.12: Modelling results using the free parameter search construction technique during 5.423 MHz heating

87

Triangulation Results

Triangulation is used as an independent check of the estimated maximum emission height. The triangulation program is provided by B. Gustavsson, as part of AIDA tools. The applied triangulation method will not be described in this thesis, since the program is only used as a sanity check of the applied tomographic reconstruction techniques and has not been developed further. The results from the triangulation are shown below:
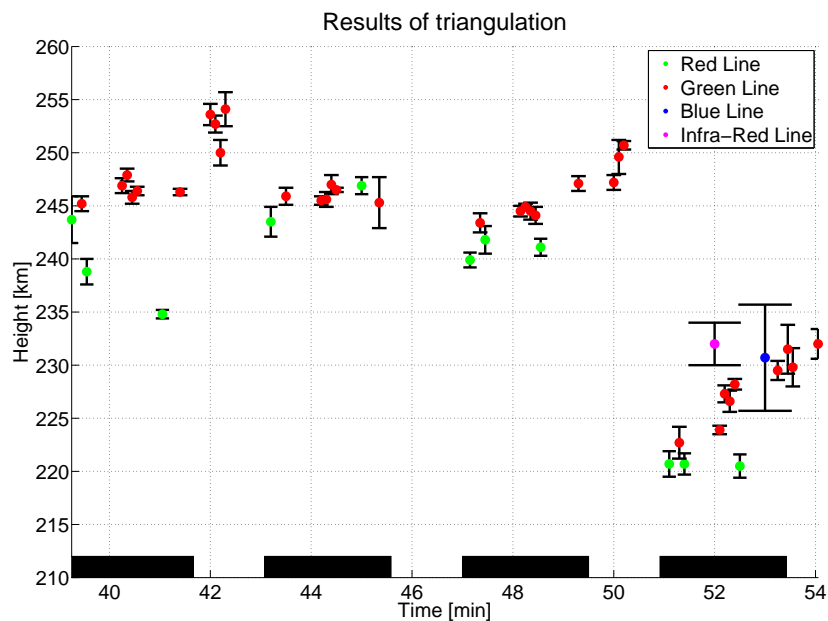
Figure B.1: The triangulation results are presented in the figure above. How the height estimates are acquired, by the program user, is described in figure B.2 below. The black boxes above the 40 min, 44 min and 48 min ticks represents the 6.200 MHz heating and the box above the 52 min tick represent heating at 5.423 MHz.
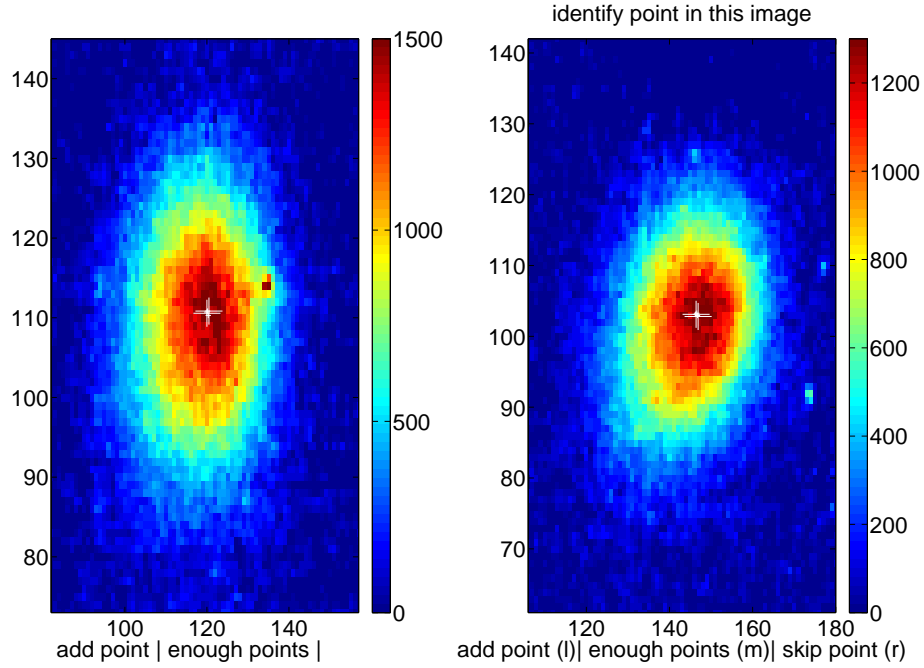
Figure B.2: The figure shows how the heights were determined. Each triangulation height was estimated from a set of white crosses in the observational images, positioned by the program user. 5 points are used for each height evaluation. The heights in figure B.1 above is therefore the mean value of 5 hight estimates, and the error bars are determined by the standard deviation.

Observational images from the station in Abisko and in Silkimoutka were used in the triangulation estimates. These two stations were chosen due to the spatial distance between the stations. The location of the stations are shown in figure 2.5. A longer baseline will provide more reliable results. In addition, the 6300 Å line images from Abisko and Silkimoutka were taken in sync, as explained in section 2.2. This allows triangulation estimates of the enhanced emission during emission decay.

Data Reduction

C.1 Background Subtraction

The background subtraction is done to isolate the heating emission from the background light. The heating emission appears and disappears within a second for emission in 4278 Å, 5577 Å and 8446 Å. This is due to the short lifetime of N_2^+1NG, $O(^1S)$ and $O(^3P)$ in the ionosphere. Images at "turn on" will thus show background light and heating emission while "turn off" images will only show the background light. The background subtraction for images in 4278 Å, 5577 Å and 8446 Å is therefore straightforward: Images at "turn off" can be used to estimate the background at "turn on". At sunset, the decay of the background light falls off approximately exponentially, see figure C.1. Interpolation in time between "turn off" images is used to estimate the background. A spline interpolation will acquire the exponential curve, and is therefore used for the entire data-set.
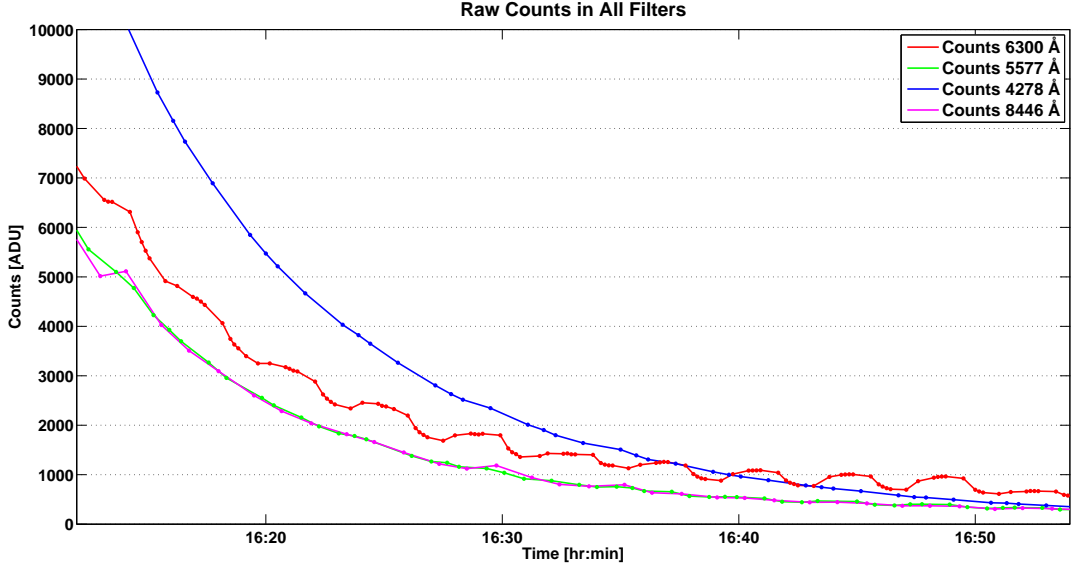
Figure C.1: The figure shows the raw counts as a function of time for the images at station A in all filters. The counts are in ADUs (analog to digital unit). High frequency induced enhancement is only visible for the 6300 Å emission.

The straightforward method can not be used for the 6300 Å emission line. The mean lifetime of $O(^1D)$ is too long, typically 40 seconds [Gustavsson et al., 2002]. The heating emission at the minima, 85 seconds after "turn off", will not be negligible. The images at "turn off" can therefore not be used directly to estimate the background light. The ratio of the Intensity at maximum, just before "turn off", and the intensity at minimum, just before "turn on" can be estimated as [Gustavsson et al., 2002]:

$$I(t) = I_0 \cdot e^{-\frac{t}{\tau}} \tag{C.1}$$

$$I(85) = I_0 \cdot e^{-\frac{85}{40}} = I_0 \cdot 0.10 \tag{C.2}$$

$$\frac{I(85)}{I_0} = 0.12 \tag{C.3}$$

Equation C.3 show that the airglow emission 85 seconds after turn off is 12 per cent of the airglow at maximum. The heating remnant should be accounted for in the background subtraction. To solve this issue, images at minima is filtered , the heating region cut out and the heating region filled in again using the image frame to interpolate the missing heating area. The process is shown step-wise in the figure below:
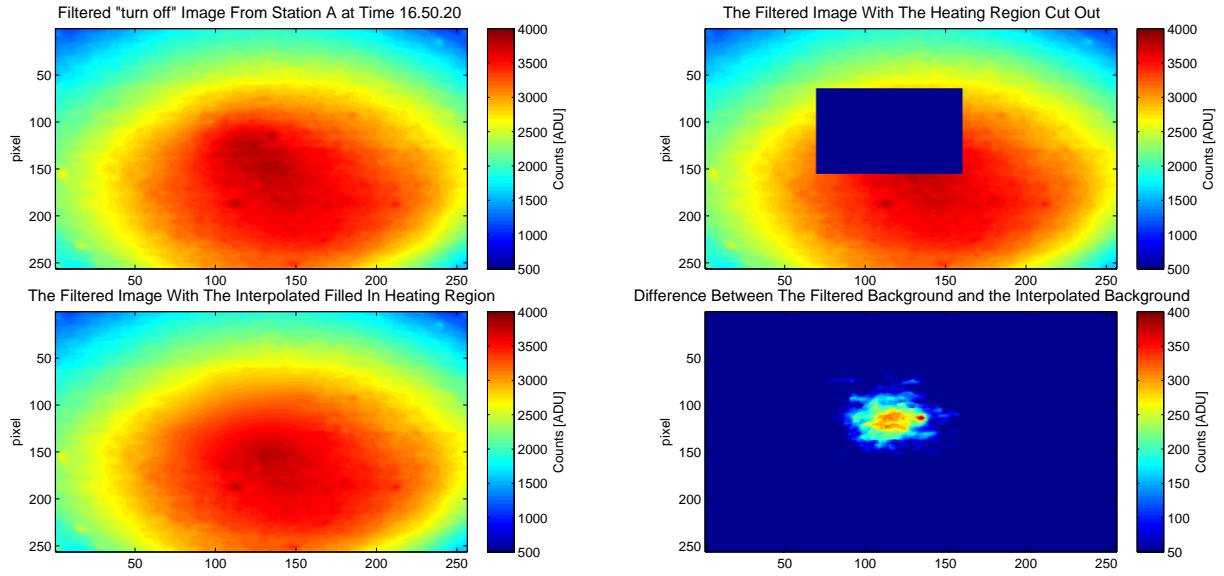
Figure C.2: It is apparent from the difference between the filtered "turn off" image and the background estimate that the heating cut out was necessary. There is a clear remnant of the heating blob. The colormap in the difference plot is scaled down to 10 per cent of the colormap in the other plots. A median filter with a five times five grid is used to filter the "turn off" images.

Finally, now that the heating remnant is removed, it is possible to interpolate in time to estimate the background for all images. Below is an example of how the background subtracted data is generated:
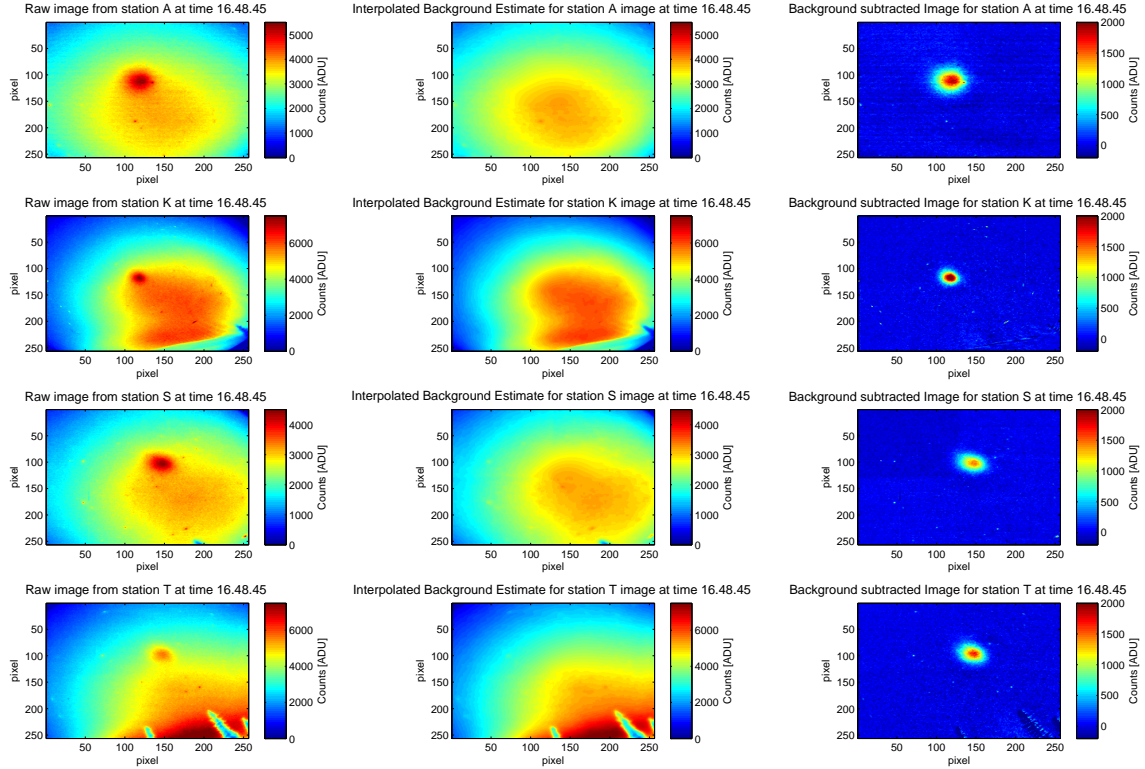
Figure C.3: The background subtraction seems to work well for all stations. It is even possible to separate the top-left CCD quadrant from the others in station S. Stars are not completely removed due to filtering of the background image and due to the rotation of the Earth. It is worth mentioning that these background subtracted images will not be used further. Flat-field correction will be applied to both the background estimated image and the science image before the subtraction. See figures C.12, C.13 and C.14 for the final background subtracted and flat field corrected image.

To check how good the background fit really is, a cut in x-axis (row) and y-axis (column) through the maximum of the heating blob is done for all stations:
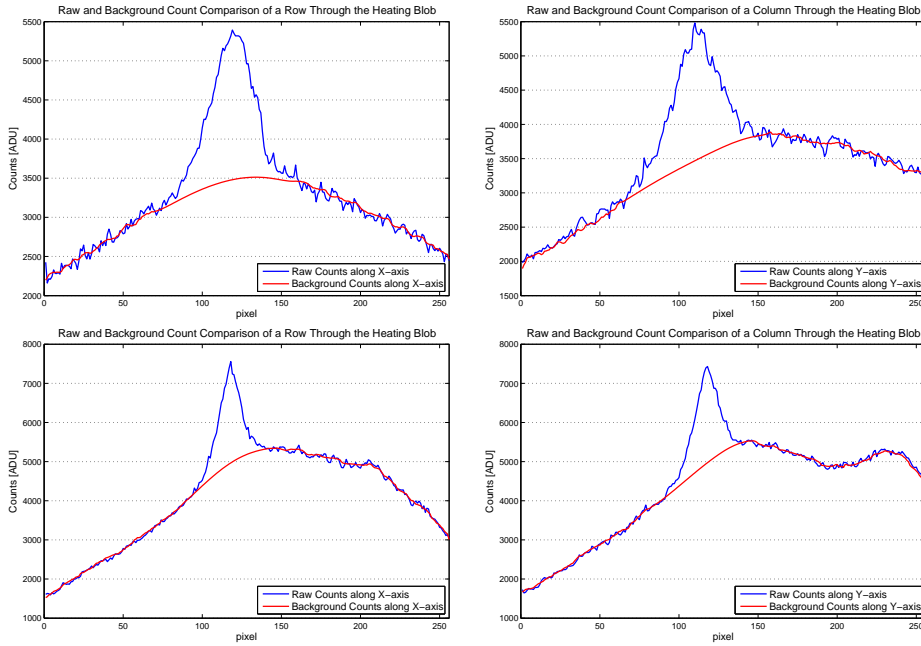
Figure C.4: The top plots show the Station A count comparison of the heating image and the estimated background image in 6300 Å at time 16.48.45. The bottom plots shows the same for station K.
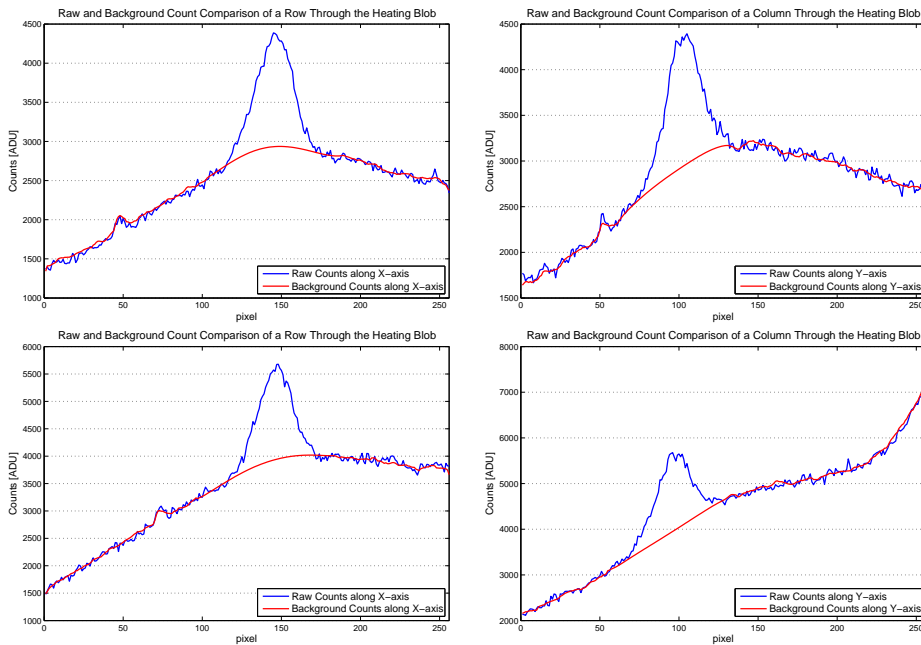
Figure C.5: The plots at the top show the Station S count comparison of the heating image and the estimated background image in 6300 Å at time 16.48.45. At the bottom, the same is sown for station T.

Background estimates are produced in the same manner as shown in figure C.2 and C.3 for all images in 6300 Å. For emission in 4278 Å, 5577 Å and 8446 Å, the process described in figure C.2 can be skipped and the background estimate procedure described in figure C.3 can be applied directly.

C.2 Flat-Field Correction

Flat field correction is needed to remove pixel to pixel sensitivity differences in the CCD, vignetting and irregularities in the optical system [Brändström, 2003]. Images taken at sunset are used as "flat images". These images have no apparent heating and high count values in each pixel (i.e. high signal to noise ratio without saturating the pixels). These images is expected to be quite flat with a small count gradient towards the direction of the sun. However, this is not the case, the flats and the heating images do not have a smooth and flat background at all, as can bee seen in figure C.6. Flat field correction will thus improve the image quality.
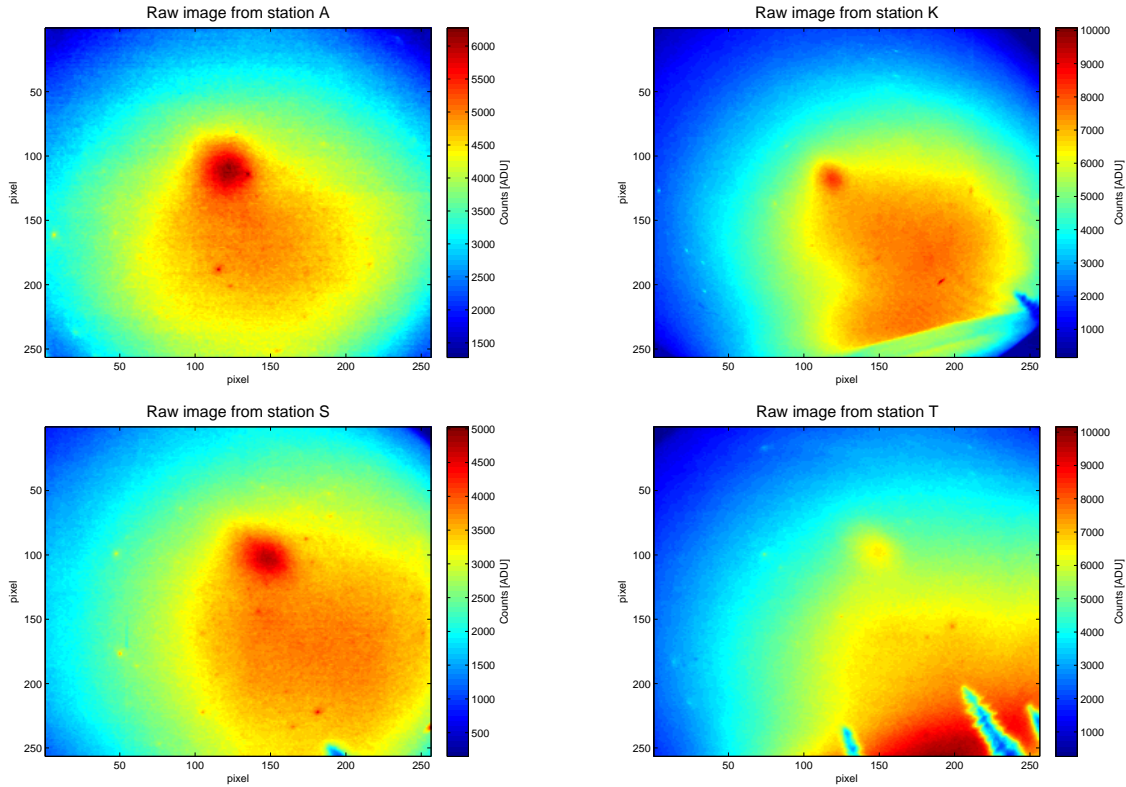
Figure C.6: Raw heating images at time 16.41.40 for the 6300 Å emission. The background sky is clearly not smooth and flat, there are gradients and irregularities in the image for all stations. The blue pillars in the bottom right corner in the image for station T, and barely visible for station S and K, are trees.

The ADU intensity output for a pixel with coordinates (u,v), I(u,v) is [Gustavsson, 2000]:

$$I(u,v) = A_{u,v} \cdot \tilde{I}_{u,v} + Z_{u,v} + C_{u,v}(t) \tag{C.4}$$

Where A is the CCD sensitivity matrix. $A_{u,v}$ is the sensitivity of pixel (u,v), $\tilde{I}_{u,v}$ is the number of photons that hit the pixel (u,v), $Z_{u,v}$ is the bias value of the pixel (u,v) and $C_{u,v}$ is the dark current of pixel (u,v). The bias frame is estimated using an overscan region. The bias frame estimation and the bias subtraction is already done in the data received

by ALIS. The dark current is neglected since the exposure time of 10 seconds is too short to get a considerable amount of counts. The dark current only becomes significant for exposure times of more than 10-15 min[Brändström, 2003]. The light sensitivity of pixel (u,v) then becomes:

$$A_{u,v} = \frac{I_A LIS(u,v)}{\tilde{I}_{u,v}} \tag{C.5}$$

The area containing the heating emission, the region of interest, is cut out. It is assumed that the amount of electrons hitting the CCD is the same for all pixels in this region (i.e the sky is considered flat within the region of interest), but the pixel gain is different. Hence $I_A LIS$ is the observed flat image in the heating region and $\tilde{I}$ is the mean value of the pixels in $I_A LIS$. The sensitivity matrix A will then be properly scaled with a mean value of 1. For each flat image, one sensitivity matrix (one "flat"), is generated for the region of interest. All the "flats" are median combined into one "master flat image" to reduce noise and to get a reliable flat field. One "master flat image" is produced for each station.
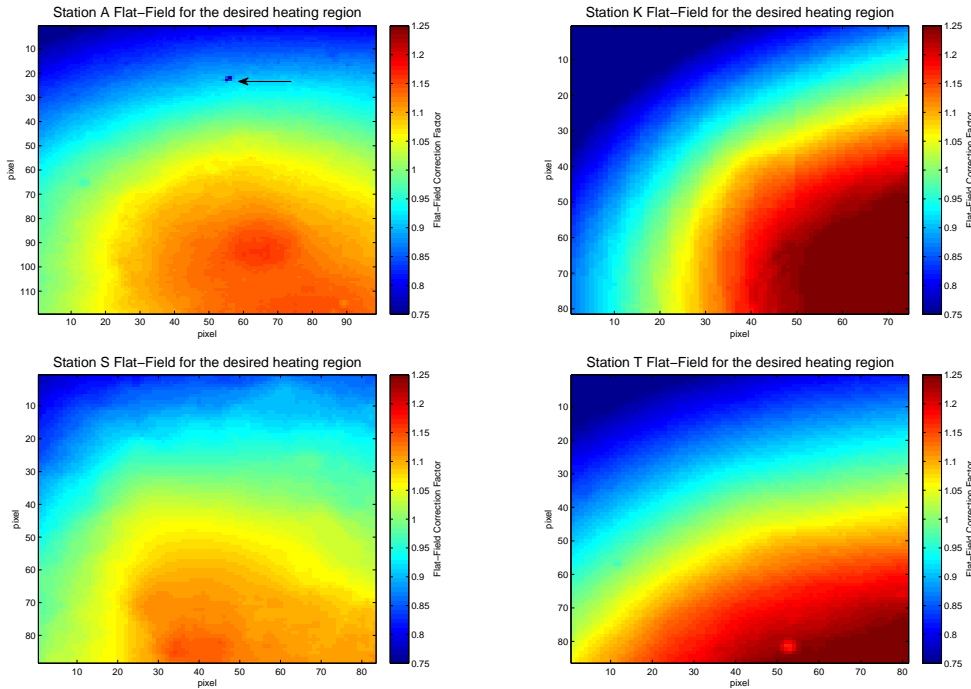
Figure C.7: The saved master flat images for the 6300 Å line, The arrow in station A points to a cluster of bad pixels

The raw images of a given station is then be divided by the master flat image. The more light sensitive pixel values will be scaled down while the less light sensitive pixel values will be scaled up. The result should ideally be a flat image with the heating blob in the middle.
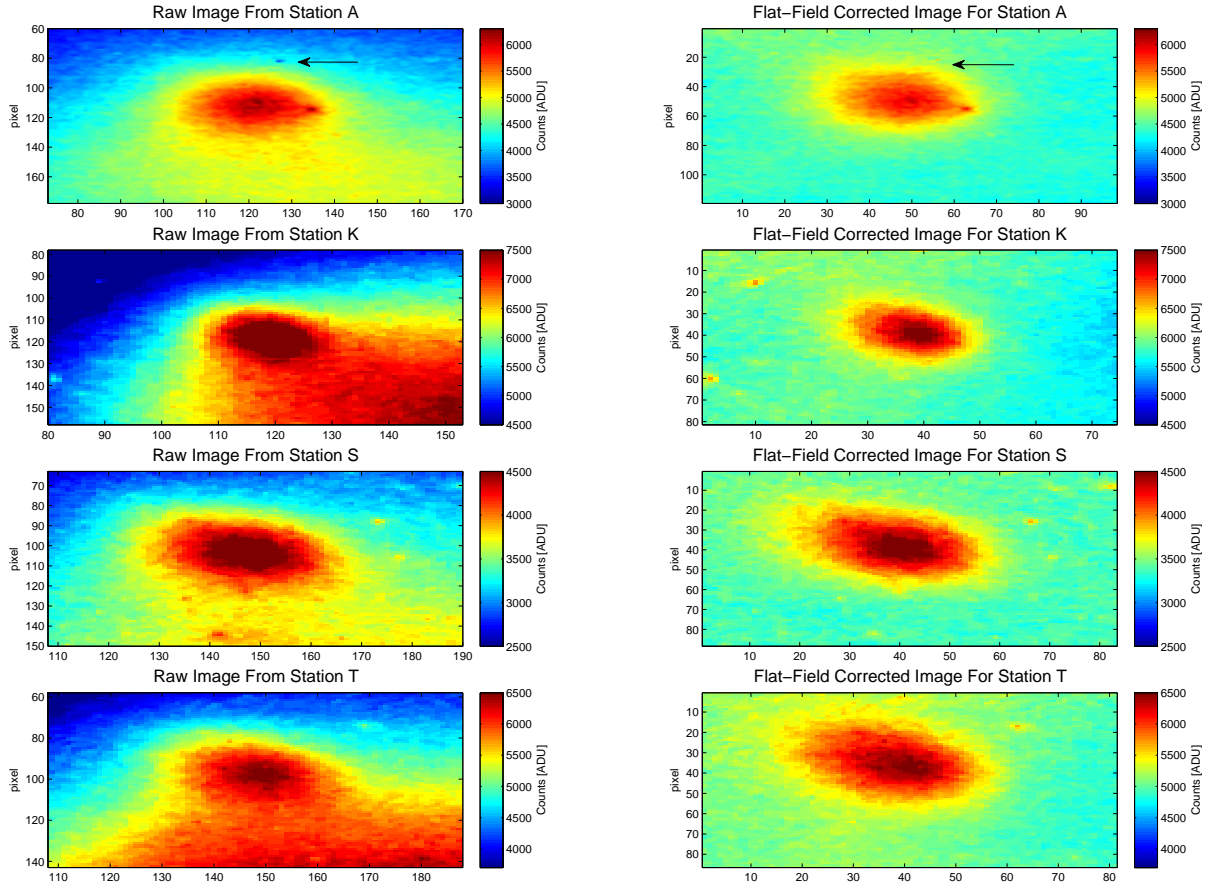
Figure C.8: The flat-field corrected images have a smoother background. The bad pixels, marked with an arrow in station A, is corrected and more importantly, the gradient in the heating blob is adjusted. It is important to correct this in order to extract polite information. The vignetting (mainly) distorted the shape of the heating blob.

The heating blob should ideally be in the middle of the image in figure C.8 for all stations. Nevertheless, since the heating blob moves around quite a bit, a trade-off is necessary. A reasonable heating region for all the heating pulses is chosen by looking at movies of the heating blob. A fixed region for all pulses makes the data set more consistent and it is easier to compare pulses.

As far as i know, doing the flat-field correction with twilight flats have not been done before for ALIS data. Theoretical flats have been used instead to adjust for vignetting. According to Brändström [Brändström, 2003], several attempts have been done to find a good way of doing flat-field correction without success. Hence the use of theoretical flats from a mathematical model is used in absence of other options [Brändström, 2003]. The reason for the ALIS flat-field correction problems might be the attempt of finding a flat-field for the entire image. Since the vignetting and the irregularities are so significant in the images it might be impossible to find a good flat field for the full image. There is a gain factor difference of at about 2 for stations A, S and T and a factor of 6.5 for station K. The pixel to pixel gain differences over the image are just too large to adjust without distortions.
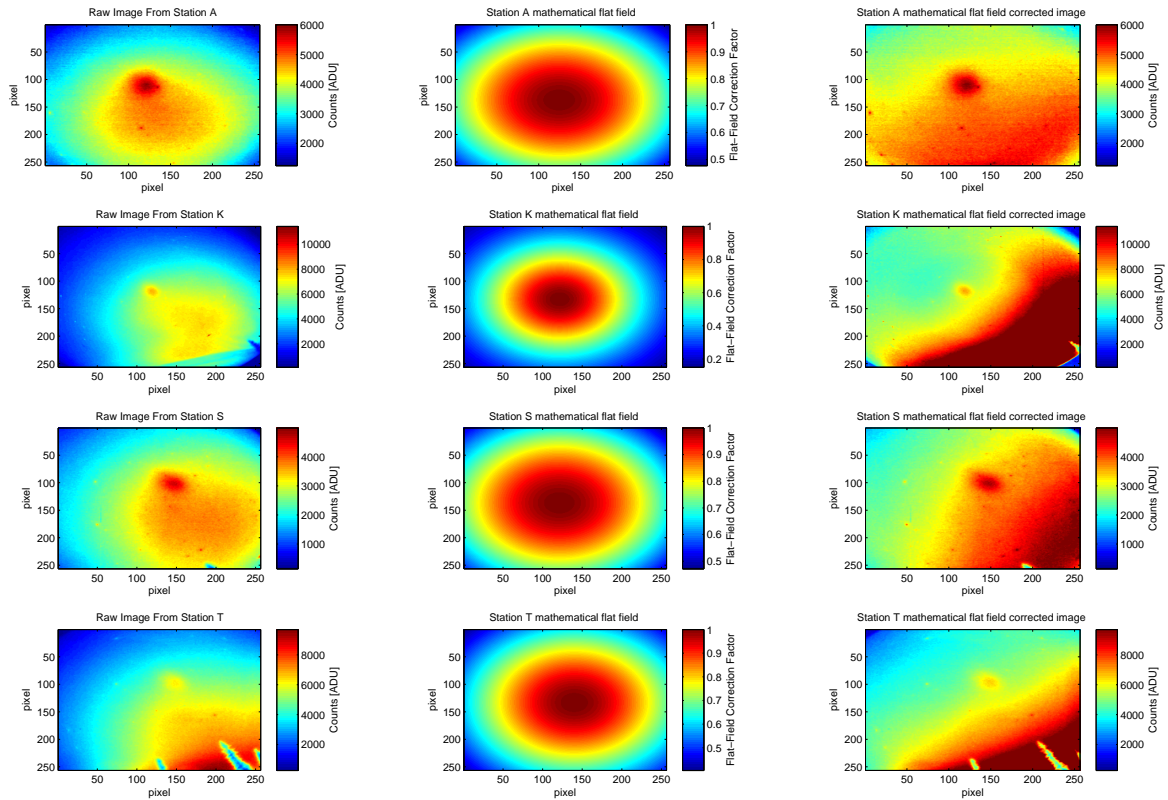
Figure C.9: It is clear that the theoretical flats does not improve the quality much. For station K the flat-field correction is borderline making the quality worse. It might be possible to improve the flat-field correction by changing the center and width of the vignetting correction, but not by much, the theoretical flats will always only be able to adjust for the vignetting and unable to account for bad pixels and irregularities in the optical system.

However, finding the flat field of a desired region, the heating region, might be a good solution. Comparing the flat-field corrected images from figure C.8 and C.10, this might be the better option and should be considered in future image reductions of ALIS data.
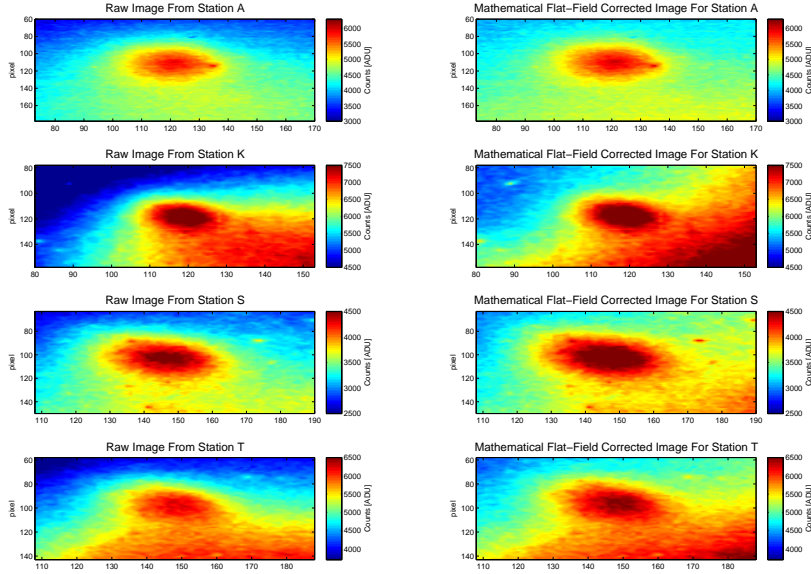
Figure C.10: The flat-field corrected images using theoretical flats from a mathematical model. The images have the same axis and count range as in figure C.8 for better comparison.

It is apparent form figure C.8 that the flat correction improved the quality of the data for the 6300 Å line. Master flats for the remaining filters 4278 Å, 5577 Å and 8446 Å were produced in the same manner. Flat-field correction using these flats also improved the data quality, as can bee seen in figure C.11. The master flats were saved and used for the entire data set.
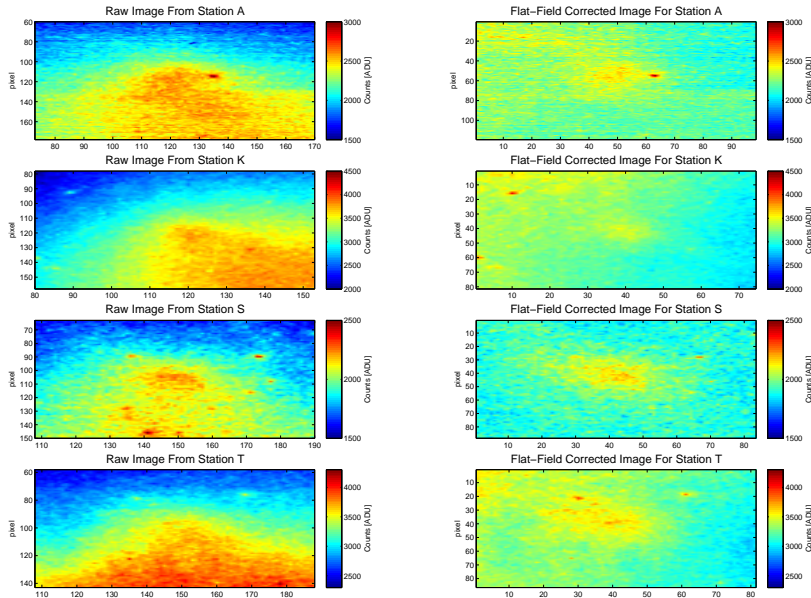
Figure C.11: Raw heating and flat-field corrected images at time 16.45.00 for the 5577 Å emission.

C.3 Data Reduction Quality Check

The background subtraction will be done after flat field correction of both the heating image and the background estimate. The process described in figure C.3 will then look like:
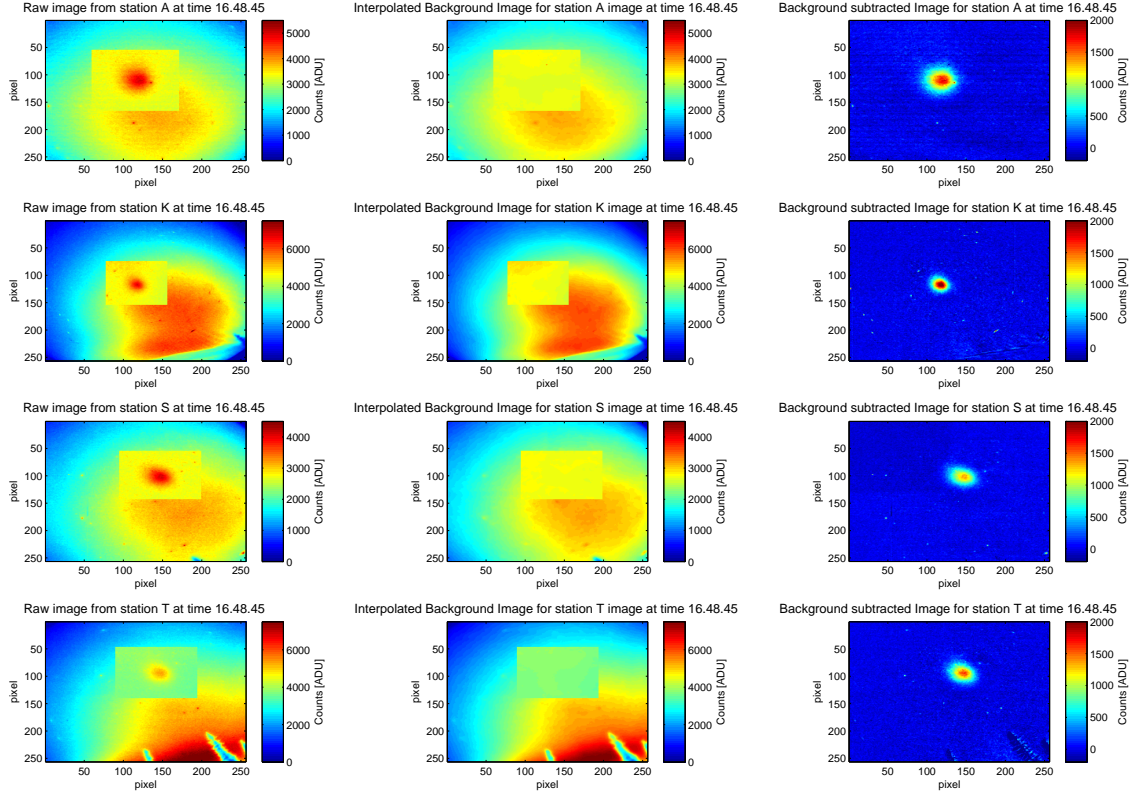
Figure C.12: The flat field corrected region is clearly visible in the heating and the background images. The background subtracted images look much alike the background subtracted images in figure C.3. Nevertheless, there is an important difference, the gain gradient in the heating blob is adjusted. Even small gain gradients in the observed blob will deform the three dimensional shape of the heating volume created by the tomographic inversion.

These images will be used in the tomographic inversion, the lifetime calculation and the diffusion estimates. A cut in x-axis (row) and y-axis (column) through the maximum of the heating blob is done as a quality check of the flat field corrected and background subtracted images. The cuts in 6300 Å at time 16.48.45 for all stations is shown as an example in the figures below.
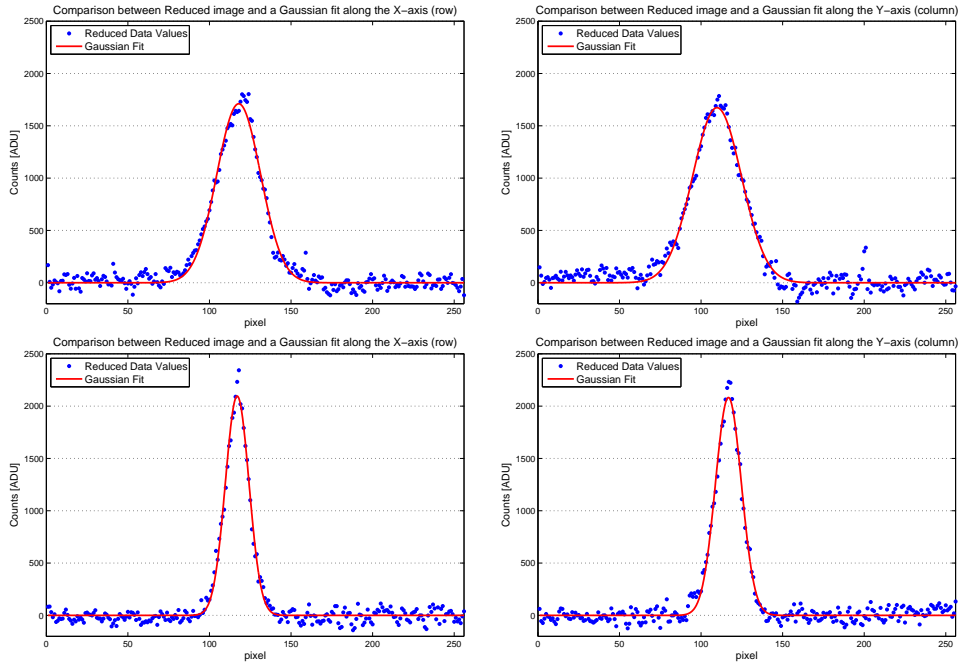
Figure C.13: The two top plots show the row and column cut through the flat field corrected and background subtracted image from station A. The bottom two plots shows the same for station K.
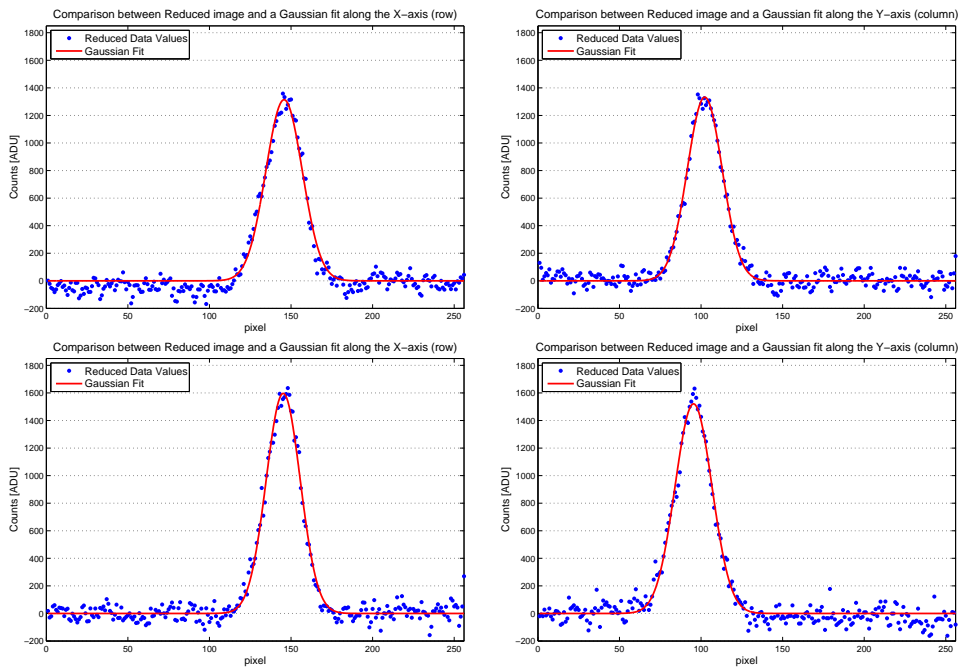
Figure C.14: The row and column cuts for station S is show at the top and below are the cut plots from station T.

It is clear that the Gaussian fit is quite good, although it is not strictly required that the heating blob should give Gaussian shaped counts in the projected camera images. Wind and atmospheric neutral density differences will distort the heating blob shape. However, figure C.13 and C.14 show that the data reduction gives the desired result: The emission from the heating blob is isolated from the background light and the count values outside the heating blob appears stochastic with no apparent trends or skews.

List of Figures

107

List of Tables

114

Bibliography

[Bernhardt et al., 1989] Bernhardt, P., Tepley, C., and Duncan, L. (1989). Airglow enhancements associated with plasma cavities formed during ionospheric heating experiments. *Journal of Geophysical Research: Space Physics*, 94(A7):9071–9092.

[Brändström et al., 1999] Brändström, B., Leyser, T., Steen, Å., Rietveld, M., Gustavsson, B., Aso, T., and Ejiri, M. (1999). Unambiguous evidence of hf pump-enhanced airglow at auroral latitudes. *Geophysical research letters*, 26(23):3561–3564.

[Brändström, 2003] Brändström, U. (2003). The auroral large imaging system: design, operation and scientific results.

[Brekke, 2012] Brekke, A. (2012). *Physics of the upper polar atmosphere*. Springer Science & Business Media.

[Brekke and Egeland, 1994] Brekke, A. and Egeland, A. (1994). *Nordlyset: Kulturarv og Vitenskap*. Grøndahl.

[Dalipi and Syla, 2013] Dalipi, B. and Syla, N. (2013). Theoretical analysis of incoherent scatter radar spectra behavior for different maxwellian ionospheric plasma conditions.

[Eliasson and Papadopoulos, 2015] Eliasson, B. and Papadopoulos, K. (2015). Numerical study of anomalous absorption of o mode waves on magnetic field-aligned striations. *Geophysical Research Letters*, 42(8):2603–2611.

[Finlay et al., 2010] Finlay, C., Maus, S., Beggan, C., Bondar, T., Chambodut, A., Chernova, T., Chulliat, A., Golovkov, V., Hamilton, B., Hamoudi, M., et al. (2010). International geomagnetic reference field: the eleventh generation. *Geophysical Journal International*, 183(3):1216–1230.

[Gondarenko et al., 2005] Gondarenko, N., Ossakow, S., and Milikh, G. (2005). Generation and evolution of density irregularities due to self-focusing in ionospheric modifications. *Journal of Geophysical Research: Space Physics*, 110(A9).

[Gordon et al., 1970] Gordon, R., Bender, R., and Herman, G. T. (1970). Algebraic reconstruction techniques (art) for three-dimensional electron microscopy and x-ray photography. *Journal of theoretical Biology*, 29(3):471–481.

[Gustavsson, 1998] Gustavsson, B. (1998). Tomographic inversion for alis noise and resolution. *Journal of Geophysical Research: Space Physics*, 103(A11):26621–26632.

[Gustavsson, 2000] Gustavsson, B. (2000). Three dimensional imaging of aurora and airglow.

[Gustavsson et al., 2002] Gustavsson, B., Brändström, B. U. E., Steen, Å., Sergienko, T., Leyser, T. B., Rietveld, M., Aso, T., and Ejiri, M. (2002). Nearly simultaneous images of hf-pump enhanced airglow at 6300 å and 5577 å. *Geophysical research letters*, 29(24).

[Gustavsson and Eliasson, 2008] Gustavsson, B. and Eliasson, B. (2008). Hf radio wave acceleration of ionospheric electrons: Analysis of hf-induced optical enhancements. *Journal of Geophysical Research: Space Physics*, 113(A8).

[Gustavsson et al., 2005] Gustavsson, B. et al. (2005). The electron energy distribution during hf pumping, a picture painted with all colors.

[Gustavsson et al., 2006] Gustavsson, B., Leyser, T., Kosch, M., Rietveld, M., Steen, Å., Brändström, B. U. E., and Aso, T. (2006). Electron gyroharmonic effects in ionization and electron acceleration during high-frequency pumping in the ionosphere. *Physical review letters*, 97(19):195002.

[Gustavsson et al., 2001] Gustavsson, B., Sergienko, T., Rietveld, M., Honary, F., Steen, A., Brändström, B., Leyser, T., Aruliah, A., Aso, T., Ejiri, M., et al. (2001). First tomographic estimate of volume distribution of hf-pump enhanced airglow emission. *Journal of Geophysical Research: Space Physics*, 106(A12):29105–29123.

[Hedin, 1991] Hedin, A. E. (1991). Extension of the msis thermosphere model into the middle and lower atmosphere. *Journal of Geophysical Research: Space Physics*, 96(A2):1159–1172.

[Kosch et al., 2002] Kosch, M. J., Rietveld, M., Kavanagh, A., Davis, C., Yeoman, T., Honary, F., and Hagfors, T. (2002). High-latitude pump-induced optical emissions for frequencies close to the third electron gyro-harmonic. *Geophysical research letters*, 29(23).

[Lagarias et al., 1998] Lagarias, J. C., Reeds, J. A., Wright, M. H., and Wright, P. E. (1998). Convergence properties of the nelder–mead simplex method in low dimensions. *SIAM Journal on optimization*, 9(1):112–147.

[Mantas, 1994] Mantas, G. P. (1994). Large 6300-å airglow intensity enhancements observed in ionosphere heating experiments are excited by thermal electrons. *Journal of Geophysical Research: Space Physics*, 99(A5):8993–9002.

[Mantas and Carlson, 1996] Mantas, G. P. and Carlson, H. C. (1996). Reinterpretation of the 6300-å airglow enhancements observed in ionosphere heating experiments based on analysis of platteville, colorado, data. *Journal of Geophysical Research: Space Physics*, 101(A1):195–209.

[Rydesäter and Gustavsson, 2000] Rydesäter, P. and Gustavsson, B. (2000). Investigation of smooth basis functions and an approximated projection algorithm for faster tomography. *International journal of imaging systems and technology*, 11(6):347–354.

[Stubbe, 1981] Stubbe, P. (1981). Modifying effects of a strong electromagnetic wave upon a weakly ionized plasma: A kinetic description. *Radio Science*, 16(3):417–425.